MEASUREMENT OF SPECTRAL CUT-OFFS OF THE ACTIVE GALACTIC NUCLEUS MRK 421 WITH VERITAS

D i s s e r t a t i o n

zur Erlangung des akademischen Grades

d o c t o r   r e r u m   n a t u r a l i u m

(Dr. rer. nat.)

im Fach Physik

eingereicht an der

Mathematisch-Naturwissenschaftlichen Fakultät

der Humboldt-Universität zu Berlin

von

Dipl.-Phys. Roman Welsing

Geboren am 7. Oktober 1981 in Borken (Westfalen)

Präsident der Humboldt-Universität zu Berlin

Prof. Dr. Jan-Hendrik Olbertz

Dekan der Mathematisch-Naturwissenschaftlichen Fakultät

Prof. Dr. Elmar Kulke

Gutachter: 1.   ....

                2.   ....

                3.   ....

Tag der mündlichen Prüfung: ....

Meiner Mutter Gisela Welsing
in tiefer Dankbarkeit gewidmet.

Abstract

VERITAS, an array of four imaging atmospheric Cherenkov telescopes, is capable of measuring spectra of very-high-energy ($E > 100$ GeV) γ-rays with high precision. On the basis of these spectra, conclusions can be drawn about the acceleration mechanisms in γ-ray sources. For instance, spectral cut-offs can indicate that there is a maximal energy available in the source.

In this work, 108 h of VERITAS data on the blazar Markarian 421 have been analysed by means of an implementation of a *Forward Folding* algorithm. By Forward Folding the complete instrument response function, factors including energy resolution and bias can be taken into account in the energy reconstruction. In particular, this method facilitates significant detections of spectral features, such as an exponential cut-off, and additionally, the spectral parameters can be determined with great accuracy. A dependence of the spectral index on the flux level of Markarian 421 could be detected with a significance of $> 3\sigma$. This dependence was interpreted as a shift of the peak energy of Inverse Compton emission to higher energies. Besides the application of Forward Folding to data of Markarian 421, the potential to detect exponential cut-offs with VERITAS and CTA, the next generation ground based γ-ray observatory, with this method was investigated. This study shows the influence of the energy resolution on the sensitivity of the instrument to spectral cut-offs. This sensitivity has been quantified for various cut-off energies.

Kurzfassung

VERITAS, ein abbildendes atmosphärisches Cherenkov-Teleskopsystem der dritten Generation, erlaubt es Spektren von hochenergetischer ($E > 100$ GeV) Gammastrahlung mit grosser Präzision zu messen. Anhand dieser Energiespektren können Rückschlüsse über die Beschleunigungsmechanismen in der Gammastrahlungsquelle gezogen werden. Spektrale cut-offs können durch eine maximale, verfügbare Energie in der Quelle zu Stande kommen.

In dieser Arbeit wurden 108 Stunden VERITAS-Daten des Blazars Markarian 421 mit Hilfe eines neu implementierten *Forward Folding* Algorithmus analysiert. Durch *Forward Folding* kann die komplette instrumentelle Antwortfunktion, einschliesslich Energieauflösung und -bias, in der Energierekonstruktion berücksichtigt werden. Diese Methode erlaubt es insbesondere spektrale Merkmale, wie etwa einen exponentiellen Cut-off, mit hinreichender Signifikanz zu beobachten. Zudem können die spektralen Parameter mit grosser Genauigkeit bestimmt werden. Eine Abhängikeit des spektralen Index von der Flussstärke von Markarian 421 konnte mit einer Signifikanz von $> 3\sigma$ nachgewiesen werden. Diese wurde als eine Verschiebung des Maximums der Emission, die auf dem Inversen Comptoneffekt basiert, zu höheren Energien interpretiert.

Neben der Anwendung des Forward Folding auf Daten von Markarian 421, wurde das allgemeine Potential dieser Methode zur Detektion exponentieller Cut-offs mit VERITAS und CTA, dem TeV Gammastrahlenobservatorium der nächsten Generation, untersucht. Diese Studien zeigen den Einfluss der Energieauflösung auf und quantifizieren die Sensitivität auf Cut-offs bei verschiedenen Energien.

Contents

Chapter 1

Introduction

Since the discovery of cosmic rays by Victor F. Hess in 1912, the search for the origin of these highly energetic particles has attracted numerous physicists. The acceleration of hadrons up to energies of 10^{20} eV happens under the most extreme conditions in the universe.

Particle astrophysics has emerged from table-top experiments probing these cosmic rays in cloud chambers, for example, to multi-kilometer arrays of instruments such as the Pierre Auger Observatory, the IceCube Observatory, and the planned Cherenkov Telescope Array (CTA). The Pierre Auger Observatory is a cosmic ray particle detector in Argentina which covers $\sim$ 3000 km^2. IceCube, located at the South Pole, is a neutrino detector that consists of $\sim$ 1 km^3 of ice equipped with Cherenkov light detectors. CTA is the planned successor to current imaging atmospheric Cherenkov telescope (IACT) experiments that will cover more than $\sim$ 1 km^2.

Detecting particles with a neutral electric charge provides direct information about their source, as they are not deflected by magnetic fields, which would obfuscate their origin. γ-ray astronomy permits the direct study of the most extreme objects in the universe, emitting electromagnetic radiation more than one hundred thousand times as energetic as visible light[1]. However, the γ-rays are absorbed in the atmosphere and, therefore, can not be detected directly on ground. It is the Cherenkov light emitted by an air shower of relativistic particles which leaves a foot print of the properties of the primary γ-ray on the ground. The γ-ray initiates such a cascade due to its electromagnetic interaction with the nuclei of air. The energy of the primary photon is transferred into the air shower particles by pair creation. Using the earth's atmosphere as a calorimeter in this way allows a relatively large effective collection area to be obtained given by the size of the Cherenkov light pool (of $\sim$ 150 m radius). This is important as the flux of γ-rays falls steeply with energy. Therefore, satellite experiments with a volume limited by the size of the space-craft are not sensitive at TeV energies.

---

[1]Violet light has an energy of $\sim$ 3 eV. Hence, low energy γ-rays of 300 MeV have one hundred thousand times this energy. TeV γ-rays reach up to 10^{12} times the energy of visible light.

The γ-ray sky

The sources of very-high-energy (VHE) γ-rays have both galactic and extragalactic origins. Currently, there are 147 detections by IACTs in the TeV energy range [146]. Of these, 53 sources are extragalactic blazars, active galaxies with a supermassive black hole in their nuclei. All objects, colored according to their source type are displayed in galactic coordinates in Figure 1.1. The physics of blazars is introduced in Chapter 2.
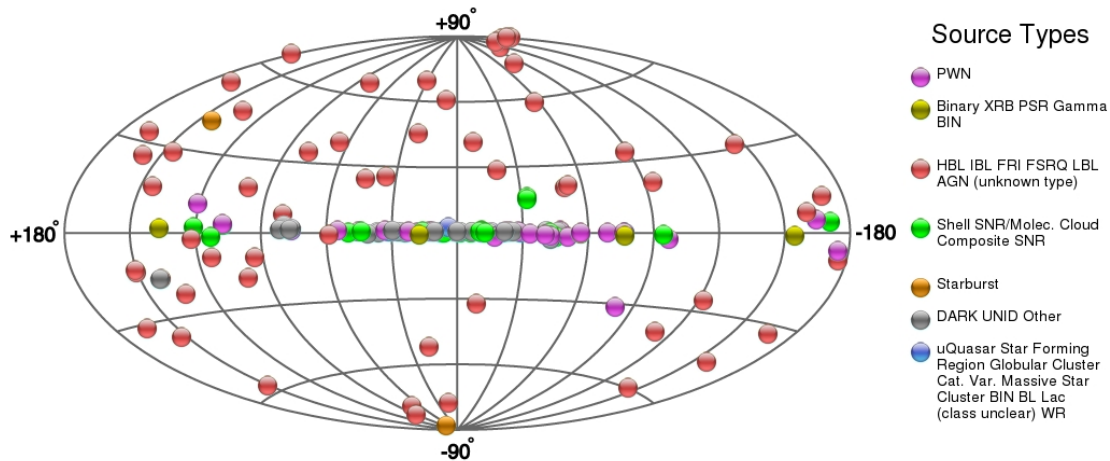
Figure 1.1: Skymap of TeV γ-ray sources in galactic coordinates: The colour of the points represents the object class of the TeV source. Pulsar Wind Nebulae (PWN) are displayed in Magenta, binary systems are displayed in dark yellow, Supernova Remnants (SNR) are shown in green. Extragalactic blazars are displayed in red and Starburst galaxies in dark orange. Picture taken from [tevcat.uchicago.edu] as of Apr. 9, 2014 [146].

VERITAS observations of Markarian 421

The goal of this thesis is to measure the spectrum of the blazar Markarian 421 (Mrk 421) precisely in order to gain insights into the acceleration mechanism responsible for the VHE emission. The spectrum of Mrk 421 shows a cut-off in the TeV domain, possibly due to a maximal energy available in the acceleration process. The measurement of this spectral cut-off is limited by the finite energy resolution of the detector (see Chapter 3). Unfolding algorithms which take into account the detector response allow for a more precise measurement of the energy spectrum. Therefore, the potential to detect an exponential cut-off with VERITAS by means of Forward Folding is studied in this thesis (see Chapter 4). An outlook on the potential to measure such spectral features with CTA is given. Finally, the method is applied to VERITAS observations of Mrk 421 (in Chapter 5).

VHE γ-ray instruments

To measure the spectral energy distribution (SED) of blazars is a multi-wavelength effort, ranging from the radio emission to TeV γ-rays. Due to the relatively low flux in very-high-

energy γ-rays, these can only be measured indirectly by IACTs. The principle of IACTs is to use the earth's atmosphere as a calorimeter, which results in a large effective area of $\sim 10^5 \mathrm{m}^2$. There are currently three IACT experiments in operation. This third generation of IACTs still uses the same detection principle for γ-rays as the pioneering Whipple 10 m telescope, which was built in 1968 and decommissioned in 2011. The first detection of TeV γ-rays by means of the imaging atmospheric Cherenkov technique was achieved with this telescope in 1989 [147]. The discovered Crab Nebula is a Pulsar Wind Nebula of relativistic particles powered by the Crab pulsar. It is the brightest object in the γ-ray sky to have constant flux, and therefore serves as the reference standard candle for γ-ray astrononmy.

Significant improvement of the IACT technique, following the pioneering work of the Whipple collaboration, was achieved by the second generation of instruments HEGRA [57] and CAT [38] by introducing the stereoscopic approach (see Section 3.1.3) of multi-telescope arrays.

Instrument	Lat.	Long.	Alt.	Telesc.	Area	Pixels	FoV	Thresh.
Whipple	32°	−111°	2300 m	1	75 m^2	379	2.3°	300 GeV
HEGRA	29°	18°	2200 m	5	8.5 m^2	271	4.3°	500 GeV
CAT	42°	2°	1650 m	1	17.8 m^2	600	4.8°	250 GeV
H.E.S.S.	−23°	16°	1800 m	4	107 m^2	960	5°	100 GeV
H.E.S.S. II	−23°	16°	1800 m	1	614 m^2	2048	3.2°	-
VERITAS	32°	−111°	1268 m	4	106 m^2	499	3.5°	70 GeV
MAGIC I+II	29°	−18°	2225 m	2	234 m^2	1039	3.5°	30 GeV

Table 1.1: Table of VHE γ-ray instruments of the first generation (Whipple), second generation (HEGRA and CAT) and third generation. The IACTs are characterized by their geographical location (latitude, longitude and altitude), hardware properties (number of telescopes, mirror area and number of pixels per telescope, Field of View) and energy threshold. The table has been taken from Acharya et al. (2013) [8], adapted from Hinton (2009) [89].

MAGIC, H.E.S.S. and VERITAS are the three IACT facilities of the current, third generation. H.E.S.S., the High Energy Stereoscopic System [15] in Namibia at 1800 m above sea level is an array of four telescopes in operation since 2003, with an additional fifth large size (28 m) telescope (H.E.S.S. II) recording first light in July 2012. MAGIC, the Major Atmospheric Gamma Imaging Cherenkov facility, consists of two 17 m telescopes located at 2200 m above sea level on La Palma, Canary Islands. The Very Energetic Radio Imaging Telescope System (VERITAS) is situated in southern Arizona at an altitude of 1268 m above sea level. VERITAS consists of four 12 m telescopes and is the main instrument of this work (see Chapter 3).

Third generation IACTs are the most sensitive detectors of TeV γ-rays. However, they are complemented by alternative detection techniques more sensitive in other energy regimes.

Satellite experiments for example, even though their effective area is limited by the size of the spacecraft, are more sensitive to the higher fluxes of γ-rays at energies below $\lesssim 50$ GeV. The $Fermi$-LAT [35], in operation since 2008, covers the energy range from 20 MeV up to 300 GeV. The extended Air-shower particle detector Milagro [34] has carried out an all sky survey of the Northern Hemisphere at energies between 250 GeV and 50 TeV. It stopped operations after seven years in April 2008. Including particle detector arrays like Tibet ASγ and ARGO-YBJ, the technique of detecting the Cherenkov light emitted by the relativistic particles in water tanks will only become competetive with the future HAWC observatory [135] [73], currently under construction.

Chapter 2

Blazar spectra at TeV energies

The majority of extragalactic γ-ray sources detected at very-high-energies (VHE) are blazars. Blazars are a specific subtype of Active Galactic Nuclei (AGN), characterized by the close alignment of their relativistic jet with the line of sight of the observer. Active Galactic Nuclei are introduced in Section 2.1. Section 2.2 describes the emission of γ-rays by relativistic particles. In Section 2.3, the power-law spectrum of γ-rays at VHE is explained, along with the possibility of deviations from a power-law (i.e., spectral curvature). This discussion motivates the search for spectral features such as exponential cut-offs, or curvature in general.

2.1 Active Galactic Nuclei

AGN, the general class of Active Galactic Nuclei, can appear differently to the earth-based observer. Because the emission from AGN is highly anisotropic, the observational differences can be explained by the orientation of the AGN and its relativistic jet with respect to the line of sight of the observer according to the AGN unification concept (for a review see Padovani & Urry, 1995 [143]). In the next subsection, the classification of AGN and the AGN unification scheme are explained. In Subsection 2.1.2, the underlying physics is briefly discussed. The last Subsection 2.1.3 focusses on blazars, introducing all blazars discovered at TeV energies.

2.1.1 Historical classification and unification scheme

AGN were first observed in the radio band as quasi-stellar objects (quasars) in the 1960s, making use of new, powerful radio telescopes. Quasi-stellar objects are strong extragalactic radio sources and appear to be point-like in the optical due to their large distance.

The radio-loud quasars were first classified according to their morphological structure [63]. The two subgroups are low-luminosity Fanaroff-Riley class I (FR-I) and high-luminosity FR-II objects. The established limiting luminosity is $\sim L_R \approx 10^{32}$ erg s^{-1}Hz^{-1}sr^{-1} at a frequency of 175 MHz (see e.g. [63])[1]. FR-I galaxies show rather compact radio emission from the core compared to FR-II galaxies, which are dominated by radio lobes.

---

[1]Padovani & Urry (1995) give a comparable limiting value $L_{178} \approx 2 \times 10^{25}$W Hz^{-1} at 178 MHz.

Radio-loud quasars are further subdivided into Flat Spectrum Radio Quasars (FSRQ) and Steep Radio Spectrum Quasars (SRSQ). Characteristic of SRSQ, as for FR-II galaxies, is the radio lobe emission of the host galaxy, while FSRQ appear to be compact in the radio band. FSRQ together with BL Lac objects form the AGN subtype of blazars. In contrast to FSRQ, BL Lac objects do not have strong (optical) emission lines in their spectra[2]. According to Beckmann & Shrader (2012) [39], the established limiting width between BL Lacs and FSRQ is an equivalent width of 5Å in their optical emission lines[3].
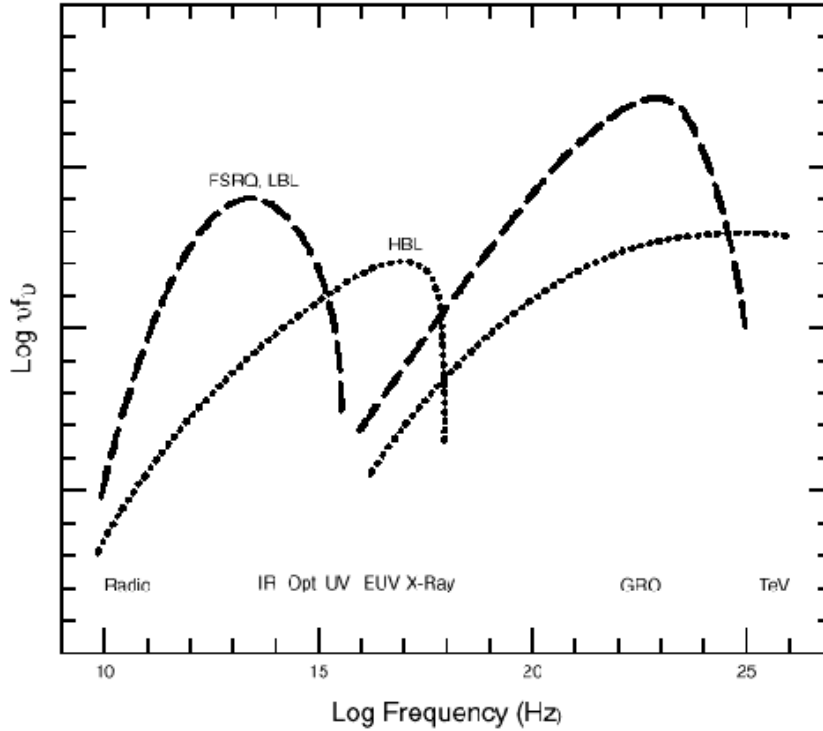
Figure 2.1: Spectral energy distribution (SED) of blazars: the characteristic double hump structure (synchroton radiation at lower energies and Inverse Compton emission at higher energies) of the SED is illustrated (see Section 2.2). The peaks of FSRQ and low-frequency peaked BL Lac objects (LBL) appear at lower energies compared to high-frequency peaked BL Lac objects (HBL). Picture taken from Urry (1998) [142].

Blazars have a characteristic double humped spectral energy distribution, the lower energy bump of which is attributed to synchrotron emission and the higher energy hump may be due to

---

[2]Recently Stocke et al. (2011) [136] however have seen weak emission lines in Markarian 421 and Markarian 501.

[3]The equivalent width (EW) is the width over which a constant flux f_C would have to be integrated, in order to result in the same flux strength as the measured flux as a function of the wavelength $f(\lambda)$:

$$EW = \int \frac{f(\lambda) - f_C}{f_C} d\lambda.$$

In practice it is the width of a rectangle with the same surface and height (f_C) as the emission line.

Inverse Compton scattering. BL Lac objects are furthermore classified according to the energy range where the synchroton emission in the spectral energy distribution peaks, as introduced by Padovani & Giommi (1995) [121]. See Figure 2.1 for an illustration.

Low-frequency peaked BL Lac objects (LBL) have a peak-frequency between 10^{13} Hz and 10^{14} Hz. For high-frequency peaked BL Lac objects (HBL), the X-ray emission exceeds the radio flux with a ratio (see e.g. [121] [143]),

$$(F_{5\text{GHz}}/F_{1\text{keV}})/7.68 < 0.75. \tag{2.1}$$

Intermediate-frequency peaked BL Lac objects (IBL) have a synchroton peak between LBL and HBL. In the unification model (see e.g. Padovani & Urry, 1995 [143]) blazars (both FSRQ and BL Lacs) are AGN with a relativistic jet aligned with the line of sight of the observer. Blazars in particular emit the bulk of their power in the γ-ray band. Since the observer is looking into the relativistic jet, the emission is amplified by relativistic beaming. Relativistic beaming enhances the flux, and boosts it towards higher energies (see Section 2.1.2). BL Lac objects in general are associated with FR-I galaxies while FSRQ are associated with FR-II galaxies [63] according to their respective luminosity.
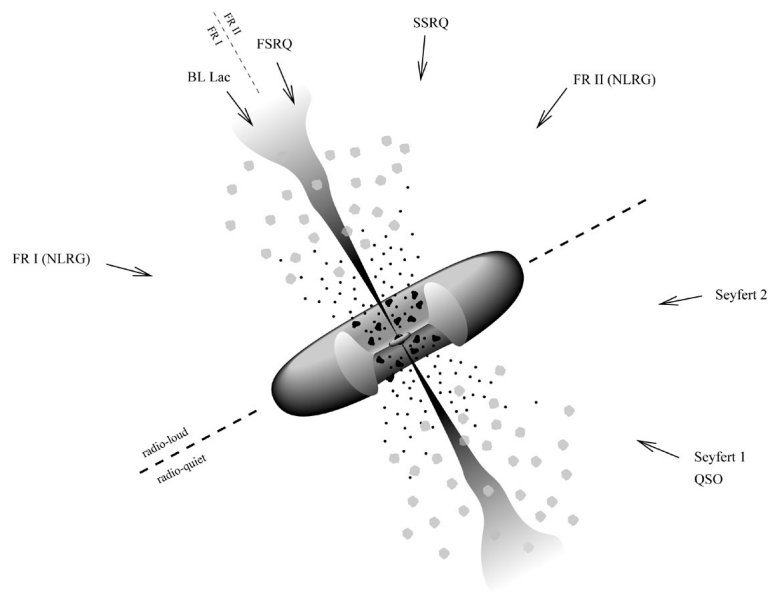
Figure 2.2: AGN unification scheme: different types of AGN associated to the corresponding angle between the line of sight and the orientation of the black hole. Picture taken from Torres et al. (2004) [140], adapted from Padovani and Urry (1995) [143].

Blazars, therefore, are radio-loud AGN. Radio-quiet quasars, on the contrary, are historically called Seyfert galaxies. Seyfert galaxies were the first type of AGN to be discovered. In 1943, Carl Seyfert already observed highly redshifted emission lines from galaxies with a very high luminosity. The bright, point-like core at the center of the galaxy is characteristic of Seyfert galaxies. Nowadays the class of Seyfert galaxies is subdivided into Seyfert 1 and

Seyfert 2 galaxies according to the spectral properties of the core [98] [97][4]. In Figure 2.2, the classification of AGNs corresponding to the orientation of the relativistic jet with respect to the line of sight of the observer is illustrated schematically.

2.1.2   AGN physics

The AGN unification scheme leads to a physical model of AGN which is characterized by a dense core, an accretion disc and relativistic jets. From the enormous luminosity it is inferred that matter is accreted onto a supermassive black hole at the center of the galaxy. Relativistic jets emanating from the core move outwards along the axis of the accretion disc.

Optical and UV emission from the core of the AGN is obscured by a dust torus in the plane of the accretion disc. The relativistic jets perpendicular to this plane emit radiation from radio to γ-ray wavelength in radio-loud AGN. If the line of sight of the observer is aligned with this relativistic jet the AGN appears as a blazar.

Overall, AGN have the following key components:

- A supermassive **black hole** of 10^6 to 10^{10} solar masses at the center of the galaxy accretes matter. Evidence for such black holes has been found first of all by estimating the mass of the dense core by means of typical values for the mass-to-luminosity ratio M/L. Secondly, the question arises whether the dark compact object is a black hole or another dense object. First elucidating studies of the velocity dispersion of stars close to the center of galaxies, proving the existence of a supermassive compact object at the center of the AGN, have been carried out by Young, Sargent et al. (1978) [150] [132]. Their object of study, M87, is shown in Figure 2.3.

---

[4]For Seyfert 1 galaxies the Balmer lines appear broader than the forbidden lines, while for Seyfert 2 galaxies both the Balmer and the forbidden lines have a narrow width.
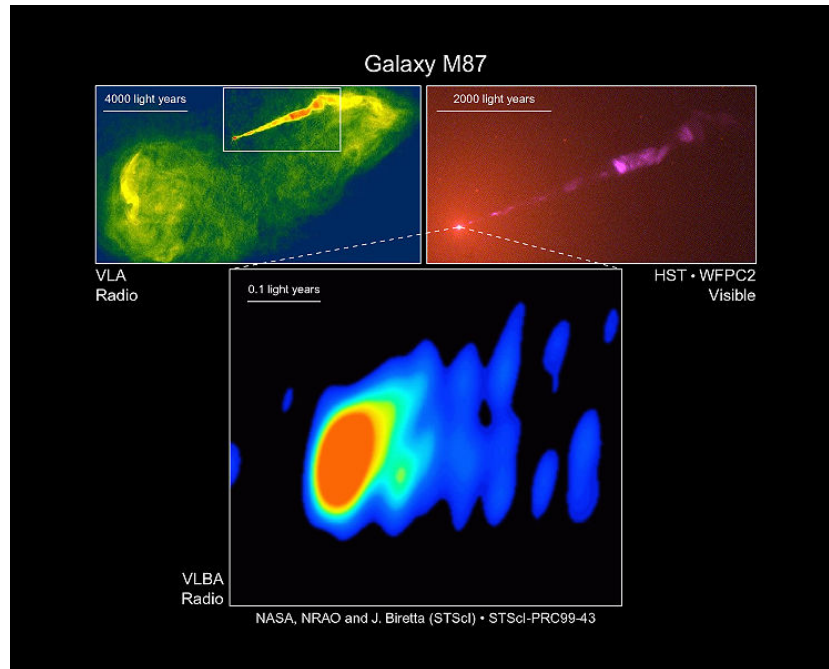
Figure 2.3: Observations of the nearby AGN M87. On the upper-left image the radio lobes are shown, as seen by the Very Large Array (VLA). The optical image (upper-right) taken by the Hubble Space Telescope (HST) zooms in, to picture the relativistic jet. Finally the Very Large Baseline Array (VLBA) image at the bottom resolves the central region close to the black hole. Picture taken from National Radio Astronomy Observatory/National Science Foundation, NASA and John Biretta (STScI/JHU), National Radio Astronomy Observatory/Associated Universities, Inc.

- Under the influence of gravity, the accretion of matter onto the black hole leads to the formation of an **accretion disk**. Because of centrifugal forces, the matter does not fall directly into the black hole. It slowly loses angular momentum by viscous forces between the neighbouring orbits in the disc. The energy is dissipated in thermal (blackbody) radiation. The maximal Eddington luminosity (see e.g. Margon & Ostriker, 1973 [111]) is reached when the radiation pressure balances gravity.

- Gas clouds in the vincinity of the black hole can be ionized by the thermal radiation from the accretion disk. Moving at high speed, the emission lines of the gas clouds are broadened by the Doppler effect, hence the name **Broad-line region**. These broad emission lines also have a narrow width counterparts. These narrow emission lines are due to lower speeds and additional forbidden, or semiforbidden emission lines. Because of the lack of variability, one concludes that they must emanate from a larger, kinematically seperate region. These regions are called **Narrow-line regions**.

- For Seyfert 2 galaxies, the optical/UV emission from the accretion is obscured by a **Dust torus** further out from the accretion disk. The dust torus then reemits the energy from the absorbed radiation in the infrared regime.

- The most extreme feature of an AGN is the highly **relativistic jet** emanating from the central core. The first observed jet (Curtis, 1918 [56]) from M87 is shown in Figure 2.3. Jets are created by an extremely energetic and highly collimated outflowing plasma with an extension of up to hundreds of kiloparsecs. They occur in radio-loud quasars, representing about 10% of AGN.

  Blandford & Znajek (1977) [49] have proposed the most common mechanism for powering the jet: the magnetic fields in the ergosphere are tied to the spin of the black hole. The natural axis of the process therefore is the rotation axis of the black hole. The reconfiguration of the field lines then leads to the launch of the relativistic material along this axis. The magnetic field lines are dragged by the rotation of the black hole, collimating the beam of particles. Lovelace & Romanova (2003) [107] have proposed a mechanism leading to the observed Lorentz factors of ~ 10 of particles in parsec-scale radio jets.

- High resolution radio interferometric images of AGN jets show localized intensity enhancements, generally referred to as **superluminal knots**. Blandford & Konigl (1979) [46] have introduced the common picture of those knots, according to which they are due to shocks in the collimated outflowing plasma. Figure 2.4 shows a radio image of knots at the radio galaxy Cen A.
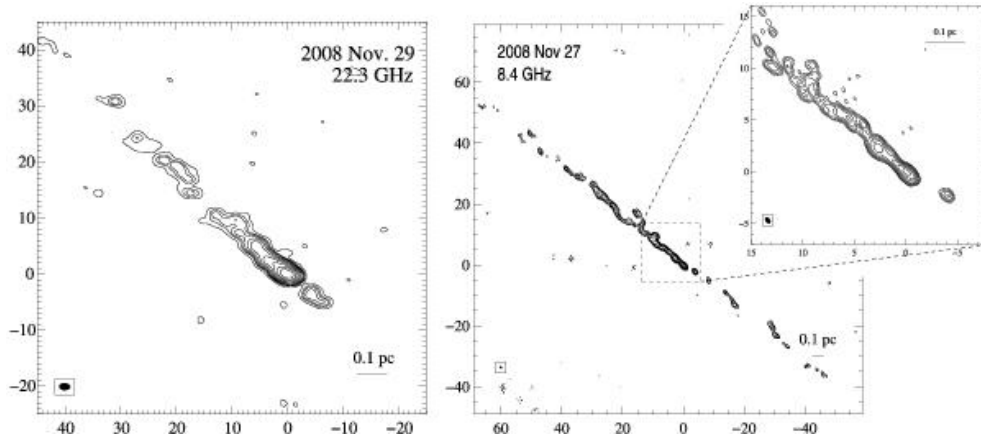
Figure 2.4: High-resolution VLBI image of Cen A, taken at 22.3 GHz (left) and 8.4 GHz (right). All axes are in units of milliarcseconds relative to the phase center. The lowest contours denote the 3σ-noise-level. Picture taken from Müller et al. (2011) [117].

Superluminal motion

Radio observations of AGN jets reveal that the knots can propagate away from the core of the AGN with an apparent speed exceeding that of light. This superluminal motion is explained by an approximate alignment of the jet with the line of sight of the observer, where the plasma is moving with highly relativistic speeds along the axis of the jet. If the knot moves at a relativistic speed $\beta = \frac{v}{c}$ under a viewing angle θ relative to the earth-based observer, then the

motion appears to happen at a speed

$$\beta_{\mathrm{app}} = \frac{\beta \times \sin\theta}{1 - \beta \times \cos\theta} \tag{2.2}$$

to the observer. Since values of up to $\beta_{\mathrm{app}} \sim 50$ have been observed by Lister et al. (2009) [105] and Piner et al. (2012) [122], there is evidence that the motion of the particles within the jet is highly relativistic.

Relativistic beaming

There are several blazars which show rapid variability in their VHE γ-ray emission on a time scale less than a few days. Indeed, variability is one of their key features [144]. This strong variability, and the size of the γ-ray emitting region, is one of the reasons by which it can be inferred (see e.g. Maraschi et al., 1992 [109] and Rees, 1967 [127]) that the γ-rays are relativistically beamed (see also Blandford & Rees, 1978 [48]). Underlying the effect of relativistic beaming are the highly relativistic speeds of the particles in the jet emanating from the core of the AGN. Assuming isotropy and a power-law emission in the rest-frame, the observed luminosity $L_{\mathrm{obs}} = \delta^4 \mathcal{L}$ is strongly amplified by the Doppler factor,

$$\delta = [\gamma(1 - \beta\cos\theta)]^{-1}. \tag{2.3}$$

This is the effect of relativistic beaming, amplifying the intrinsic γ-ray luminosity $\mathcal{L}$. Here the definition of γ is:

$$\gamma = \sqrt{1 - \beta^2}. \tag{2.4}$$

For a source approaching the observer, the time intervals measured in the observer frame are shorter than in the rest frame: $t = \delta^{-1}t'$. At the same time, the emission frequency is blue-shifted to higher energies: $\nu = \delta\nu'$. Since I_ν is a relativistic invariant the observed intensity I_ν is strongly Doppler boosted: $I_\nu(\nu) = \delta^3 I'_{\nu'}(\nu')$. For the flux $F = \int_\nu I_\nu d\nu$ this results in the expected behaviour $F = \delta^4 F'$.

So far it has been assumed that there is isotropic emission obeying a power-law in the rest frame. However real jets may be inhomogeneous and have flat spectra. Hence the observed luminosity L_j of the relativistic jet is given by the relation,

$$L_j = \delta^p \mathcal{L}_j, \tag{2.5}$$

in terms of the intrinsic luminosity $\mathcal{L}_j$. The value of p is found to range between $p = 3.10 \pm 0.25$ and $p \sim 3.8$ depending if the bulk speed is equal to, or lower than the pattern speed (see Padovani & Urry, 1995 [143]).

Since relativistic beaming enhances the flux to be observed at higher energies, most identified extragalactic sources which have been discovered in the TeV domain are blazars.

2.1.3 TeV blazars

To date there are 53 blazars which have been discovered in the TeV energy domain. Among them are 3 FSRQ. All remaining blazars are BL Lac objects. Out of these 50 BL Lac objects, the large majority (42) are HBL. Seven are IBL, and one TeV source is a LBL.

A complete list of TeV blazars is given in Table 2.1 and Table 2.2. The source name is listed together with the AGN type and the discovery date. Finally the instrument that discovered the TeV γ-ray source is given together with the respective reference of the publication. Table 2.1 lists sources up to a redshift z = 0.2 ordered according to their measured redshift. Sources without known redshift and those with a redshift bigger than z = 0.2 are listed in Table 2.2.

Mrk 421, the main topic of this work, was the first extragalactic TeV source to be discovered in 1992 by the Whipple telescope [124]. Mrk 421 is well known to have an intrinsic high energy cut-off (see e.g. Krennrich et al., 2002 [102] and Albert et al., 2007 [24]). This cut-off can not be due to interaction with the extra-galactic background light (EBL) photons, known as EBL absorption. This is because Mrk 421 has a relatively low redshift z = 0.031[5].

Markarian 501 (Mrk 501) was the second extragalacitc VHE γ-ray source to be detected. It was detected in the TeV energy range for the first time by the Whipple telescope in 1996 [125]. Its spectrum has been shown to be consistent with a power-law in recent observations by VERITAS in a low flux-state up to $\sim$ 2 TeV [7]. However, curvature could be measured by the Whipple telescope [131] in a high flux state ranging between 1 and 4.1 times the flux of the Crab Nebula in the 1997 observing season. With a spectrum extending up to 10 TeV and a fit between 1.1 - 10.4 TeV, no cut-off before 7 TeV could be measured with 95% confidence level. The best fit to the energy spectrum was given by a log-parabolic function (Equation 2.11).

The third TeV source for which curvature could be measured is PKS 2155-304. Aharonian et al. (2008) [16] reported on an extreme outburst on July 28, 2006 reaching up to 7 times the flux of the Crab Nebula. PKS 2155-304 showed a spectral break at $\sim$ 430 GeV. While the data is well fit by a broken power-law function, with a χ^2 = 17.1 for 13 degrees of freedom (d.o.f.), a simple power-law (χ^2 = 138 for 15 d.o.f.) or a power-law with an exponential cut-off (χ^2 = 45 for 14 d.o.f.) are not acceptable. From the observed fast flux variability, a factor of 5 higher than the extreme variability previously measured from Mrk 421 [69], they conclude that either the jet material must have very large Doppler factors, or that this flux variability is not connected to the central black hole.

---

[5]The EBL is thought to have been produced by the first stars, which formed in the early Universe. TeV γ-rays from distant sources interact with the EBL via electron-positron pair creation. Therefore the very-high-energy γ-rays from distant sources have a higher probability of getting absorbed. In contrast, Mrk 421 is a rather nearby AGN. Hence Mrk 421 does not significantly constrain models for the EBL. More distant blazars however recently allowed the EBL flux density to be measured with Fermi [1] and H.E.S.S. [2].

Name	Type	Date	Redshift	TeV discovery
IC 310	HBL	3/2010	0.0189	MAGIC [87]
Markarian 421	HBL	8/1992	0.031	Whipple [124]
Markarian 501	HBL	1/1996	0.034	Whipple [125]
1ES 2344+514	HBL	7/1998	0.044	Whipple [52]
Markarian 180	HBL	9/2006	0.045	MAGIC [22]
1ES 1959+650	HBL	8/1999	0.048	Telescope Array [120]
AP Lib	LBL	7/2010	0.049	H.E.S.S. (ATel #2743)
1ES 1727+502	HBL	11/2011	0.055	MAGIC [108]
BL Lacertae	IBL	4/2001	0.069	Crimea [118]
PKS 0548-322	HBL	7/2007	0.069	H.E.S.S. [137]
PKS 2005-489	HBL	6/2005	0.071	H.E.S.S. [11]
RGB J0152+017	HBL	2/2008	0.08	H.E.S.S. [19]
1ES 1741+196	HBL	8/2011	0.083	MAGIC [43]
SHBL J001355.9-185406	HBL	11/2010	0.095	H.E.S.S. [83]
W Comae	IBL	8/2008	0.102	VERITAS [4]
1ES 1312-423	HBL	12/2010	0.105	H.E.S.S. [74]
VER J0521+211	IBL	10/2009	0.108	VERITAS [33]
PKS 2155-304	HBL	6/1999	0.116	Durham [53]
B3 2247+381	HBL	10/2010	0.1187	MAGIC [27]
RGB J0710+591	HBL	2/2009	0.125	VERITAS [6]
H 1426+428	HBL	2/2002	0.129	Whipple [95]
1ES 1215+303	HBL	1/2013	0.13	MAGIC [28]
1ES 0806+524	HBL	12/2008	0.138	VERITAS [3]
1ES 0229+200	HBL	12/2006	0.14	H.E.S.S. [18]
1RXS J101015.9-311909	HBL	12/2010	0.142639	H.E.S.S. [82]
H 2356-309	HBL	4/2006	0.165	H.E.S.S. [13]
RX J0648.7+1516	HBL	3/2010	0.179	VERITAS [62]
1ES 1218+304	HBL	5/2006	0.182	MAGIC [21]
ES 1101-232	HBL	4/2006	0.186	H.E.S.S. [12]
1ES 0347-121	HBL	8/2007	0.188	H.E.S.S. [17]
RBS 0413	HBL	10/2009	0.19	VERITAS [30]
RBS 0723	HBL	01/2014	0.198	MAGIC (ATel #5768)

Table 2.1: Table of VHE γ-ray detected blazars ordered by redshift. Displayed are the canonical name, the blazar type, the year of the first TeV detection together with the redshift and TeV discovery instrument according to [tevcat.uchicago.edu] as of Apr. 10, 2014 [146].

Name	Type	Date	Redshift	TeV discovery
1ES 1011+496	HBL	9/2007	0.212	MAGIC [23]
MS 1221.8+2452	HBL	5/2013	0.218	MAGIC (ATel #5038)
1ES 0414+009	HBL	11/2009	0.287	H.E.S.S. [81]
S5 0716+714	IBL	4/2008	0.31	MAGIC [32]
1ES 0502+675	HBL	11/2009	0.341	VERITAS [149]
PKS 1510-089	FSRQ	3/2010	0.361	H.E.S.S. [145]
3C66A	IBL	3/1998	0.41	Crimea [119]
4C +21.35	FSRQ	6/2010	0.432	MAGIC [26]
1ES 0647+250	HBL	9/2011	0.45	MAGIC [59]
PG 1553+113	HBL	3/2006	0.5	H.E.S.S. [14]
3C 279	FSRQ	6/2008	0.5362	MAGIC [61]
PKS 1424+240	IBL	6/2009	-	VERITAS [5]
PKS 0447-439	HBL	12/2009	-	H.E.S.S. [84]
MAGIC J2001+435	IBL	7/2010	-	MAGIC (ATel #2753)
1ES 1440+122	HBL	8/2010	-	VERITAS (ATel #2786)
HESS J1943+213	HBL	11/2010	-	H.E.S.S. [80]
1ES 0033+595	HBL	10/2011	-	MAGIC (ATel #3719)
KUV 00311-1938	HBL	7/2012	-	H.E.S.S. [86]
PKS 0301-243	HBL	7/2012	-	H.E.S.S. [85]
RGB J0136+391	HBL	7/2012	-	MAGIC (Gamma2012)
H 1722+119	HBL	5/2013	-	MAGIC (Atel #5080)

Table 2.2: Table of VHE γ-ray detected blazars ordered by redshift (z>0.2) and those without redshift. Displayed are the canonical name, the blazar type, the year of the first TeV detection together with the redshift and TeV discovery instrument according to [tevcat.uchicago.edu] as of Apr. 10, 2014 [146].

2.2 Astrophysical processes and origin of γ-rays

The most important astrophysical processes leading to the production of γ-rays in blazars are introduced in this section. The spectral energy distribution (SED, see Figure 2.5) of blazars is represented by a so called double-hump structure. **Synchroton radiation** (see Section 2.2.1) of the relativistic particles dominates the spectrum of blazars from the radio to X-ray domains. The VHE emission is believed to be due to **Inverse Compton** scattering of photons on these highly relativistic particles, in the case that they are leptons (see Section 2.2.2). According to this scenario, photons of the synchroton radiation or external photons, from the disk, or the dust torus, for example, interact with the relativistic electrons via Inverse Compton scattering. The first case is called Synchroton-self Compton (SSC). See for example the pioneering works

of Ginzburg & Syrovatskii (1965) [72] and Rees (1967) [127], or more recent models by Marscher & Gear (1985) [112] and Maraschi, Ghisellini & Celotti (1992) [110]. The second case is called External Compton (EC, see e.g. [60]). In the hadronic scenario (see Section 2.2.3), the VHE component is either due to proton synchroton radiation or pion decay. Overall, it is plausible that a combination of these processes accounts for the origin of γ-rays[6].
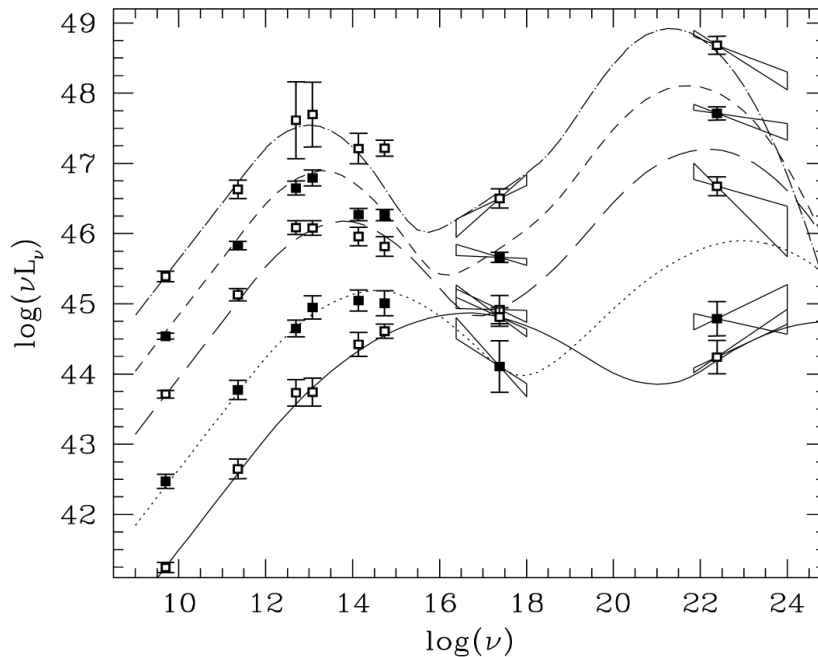

Figure 2.5: The blazar sequence obtained by Fossati et al. (1998) [68] from a sample binned according to radio luminosity. The peak frequencies of the synchroton and Inverse Compton radiation shift to lower values with increasing luminosity. Picture taken from Fossati et al. (1998) [68].

The blazar sequence from Fossati et al. (1998) [68], illustrated in Figure 2.5, shows that the peak of the Inverse Compton radiation is believed to shift to lower energies with increasing luminosities. According to this trend, strong γ-ray emitters at TeV energies have a relatively low intrinsic luminosity. Varying parameters (of magnetic field strength and/or critical energy in the electron population) as a function of luminosity would be a plausible interpretation of this blazar sequence.

2.2.1 Synchroton radiation

Synchroton radiation is produced when charged particles are accelerated in a magnetic field. In a pure B-field (with a constant field strength B) particles of charge q and mass m move at a velocity v perpendicular to the B-field in orbits with the gyroradius $r = \frac{mc}{|q|B} \times v\gamma$. Here c

---

[6]For example, Synchroton-self Compton processes must always be present, even if external Compton radiation is dominating. This is due to the presence of the photons from synchroton radiation, independent of external sources.

denotes the speed of light and γ the Lorentz factor (Equation 2.4).

In general, electric fields will exert an additional force on the charged particle, and so they follow a spiral trajectory. Due to the emission of synchroton radiation, the particle loses energy at a rate, given by:

$$-\left(\frac{dE}{dt}\right)_{sync} = \frac{4}{3}\sigma_T c \times U_{\text{mag}}\left(\frac{v}{c}\right)\gamma^2,\tag{2.6}$$

when integrated over all angles. Here $U_{\text{mag}} = \frac{B^2}{2\mu_0}$ is the energy of the magnetic field and $\sigma_T = \frac{e^4}{6\pi\epsilon_0 c^4 m_e^2}$ the Thomson cross-section. The charged particles therefore exponentially lose their energy on a timescale inversely proportional to the energy and B^2. This process is called *synchroton cooling*.

For a power-law energy distribution of electrons $N(E)dE = \kappa E^{-p}dE$, where $N(E)dE$ denotes the number density of electrons in the energy interval E to $E+dE$, the resulting spectrum of synchroton radiation in principle follows a power-law shape. The emitted flux density F_ν can be written as:

$$F_\nu \propto \kappa \times B^{(p+1)/2}\nu^{-(p-1)/2} = \kappa B^{\Gamma+1}\nu^{-\Gamma}.\tag{2.7}$$

The spectral index is thus $\Gamma = \frac{p-1}{2}$.

However, this picture is not complete. The principle of detailed balance states that each emission process is matched by an absorption mechanism. This synchroton self-absorption dominates at low energies, where the energy spectrum becomes independent of p:

$$F_\nu \propto \kappa \times B^{-1/2}\nu^{5/2}.\tag{2.8}$$

2.2.2   Inverse compton scattering

γ-rays can be produced by the interaction of relativistic electrons with photons from synchroton radiation or external sources (e.g. the disk or the dust torus). The photon field of energy density U_{rad} gains energy by Inverse Compton (IC) scattering of the low energy photons on electrons. The rate of this energy gain is:

$$\left(\frac{dE}{dt}\right)_{IC} = \frac{4}{3}\sigma_T c \times U_{\text{rad}}\left(\frac{v}{c}\right)\gamma^2.\tag{2.9}$$

Note the similarity to the rate of energy loss due to synchroton cooling (Equation 2.6) which means that the spectrum of scattered radiation, resulting from a power-law distribution of electron energies $N(E)dE = \kappa E^{-p}dE$, will again have the corresponding spectral index $\Gamma = \frac{p-1}{2}$. Expressed as photon flux density, the spectral index is increased by one power of energy: $\Gamma_{\text{ph}} = \frac{p+1}{2}$.

This result however assumes that the energy of the photons is neglible against the rest mass energy $m_e c^2$ of the electron. In this case the classical constant Thomson cross-section σ_T describes the elastic scattering of the photons. The average energy gain per Compton process in this Thomson limit is $\langle\frac{\Delta E}{E}\rangle = \frac{4}{3}\gamma^2$.

For higher energetic photons however, quantum corrections have to be taken into account. In

this Klein-Nishina regime, the cross-section decreases roughly with $\left(\hbar\omega/m_e c^2\right)^{-1}$. This has the effect that Compton scattering becomes inefficient for $\hbar\omega/m_e c^2 \gtrsim 1$, and limits the maximal energy of the scattered photons to $E_{\mathrm{max}} = \gamma \times m_e c^2$.

2.2.3 Hadronic models

Inverse Compton scattering is the dominant process which accounts for the γ-ray spectrum of cosmic accelerators of electrons. However, from the hadronic composition of cosmic rays one can conclude that also protons, for example, are accelerated to very-high-energies. This illustrates the alternative hadronic scenario for the origin of γ-rays.

Protons can either produce γ-rays directly via proton synchroton radiation, or due to hadronic interactions. The acceleration of hadrons to very-high-energies leads to a hadronic particle cascade in which neutral (π^0) and charged ($\pi^{\pm}$) pions, the lightest hadrons (with rest masses $m_{\pi^0} \approx 135$ MeV and $m_{\pi^{\pm}} \approx 140$ MeV), are produced with equal probability. The dominant decay channel (with a probability of 98.823 ± 0.034 %) of the neutral pions is the immediate (mean lifetime $\tau = (8.4 \pm 0.5) \times 10^{-17}$ s) production of two gamm-rays. For a review of hadronic models see Mücke et al. (2003) [116].

2.3 Spectral curvature at TeV energies

The VHE electromagnetic spectrum of most blazars follows a power-law over several decades in energy. The high-energy end of the γ-ray spectrum extends to about 30 TeV (e.g. [15]), where current ground-based instruments reach their statistical limit given by the convolution of flux and effective area. In specific cases however, the TeV spectrum is curved or cuts off sharply at much lower energies. On the one hand, this can be due to absorption in between distant sources and the earth-based observer (e.g., EBL absorption due to the interaction of the γ-rays with the extragalactic background-light [1] [2], see also 2.1.3). On the other hand this can be caused by the maximal power available in the acceleration processes intrinsic to the source.

In general, the measurement of spectral features in TeV energy spectra can be modeled by the following spectral shapes within uncertainties: A **power-law with an exponential cut-off** is the most common parameterization of curvature in the energy spectrum:

$$\phi_0 (E/E_0)^{-\Gamma} \times e^{-\frac{E}{E_C}}, \tag{2.10}$$

where Γ is the spectral index and E_C the cutoff-energy. A **log-parabola** spectrum,

$$\frac{dN}{dE} = \phi_0 (E/E_0)^{-a-b\times\log(E/E_0)}, \tag{2.11}$$

is another prominent instance of a parameterization of a curved spectrum. Other more complex possibilities are an **exponential cut-off log-parabola** function

$$\frac{dN}{dE} = \phi_0 (E/E_0)^{-a-b\times\log(E/E_0)} \times e^{-\frac{E}{E_C}}, \tag{2.12}$$

and a **super-exponential cut-off power-law** function

$$\frac{dN}{dE} = \phi_0 (E/E_0)^{-\Gamma} \times e^{-(E/E_C)^{\gamma}}. \tag{2.13}$$

Each of these possiblities leads to curvature in the energy spectrum deviating from a power-law:

$$\frac{dN}{dE} = \phi_0 (E/E_0)^{-\Gamma}. \tag{2.14}$$

In this section the power-law shape of the spectrum is motivated (2.3.1) and physical mechanisms leading to an exponential cut-off (2.3.2) or to log-parabolic spectra (2.3.3) are introduced.

2.3.1 Diffusive shock acceleration

The power-law shape of the cosmic ray and VHE γ-ray energy spectrum can be modeled by a stochastic acceleration mechanism at strong shock fronts. This diffusive shock acceleration was first introduced (see e.g. Blandford & Eichler, 1987 [45] [36] [103] [40] [47], for a review see Kirk and Duffy, 1999 [99]) following Fermi's [65] original version of stochastic acceleration at shock fronts, second order in the shock velocity $\frac{v}{c}$.

Diffusive shock acceleration is first order in the shock velocity. Like second order Fermi acceleration, it leads to a power-law energy spectrum. Its main characteristic however is the resulting spectral index of $\Gamma \approx 2$ for the spectral energy distribution $\frac{dN}{dE} \sim E^{-2}$ of the accelerated particle population.

The original version of Fermi acceleration was introduced as a mechanism where particles are accelerated in collisions with the interstellar medium. Let $E = \beta E_0$ be the particle's average energy after one collision (with E_0 beeing the energy before the collision, increasing by a factor β), and P the probability that the particle does not escape from the acceleration region after this collision. Then from the original N_0 particles, $N = N_0 P^k$ will be accelerated to an energy $E = E_0 \beta^k$ after k collisions. Hence, by eliminating k, a power-law spectrum is obtained:

$$\frac{N_k}{N_0} = \left(\frac{E_k}{E_0}\right)^{\ln P/\ln \beta} \tag{2.15}$$

In Fermi's original version, the index

$$\ln P/\ln \beta = -(\alpha\tau_{\text{esc}}), \tag{2.16}$$

is related to the characteristic time τ_{esc} the particles are contained in the acceleration region and the rate of the energy increase α, where α is proportional to $(v/c)^2$.

Introducing Diffusive Shock Acceleration, the relative increase in energy

$$\frac{\Delta E}{E} = \frac{v}{c}\cos\theta \tag{2.17}$$

is first order in the shock velocity U. Here $v = \frac{3}{4}U$ is the velocity at which the gas in the downstream region moves towards the particle in the upstream region. θ is the angle of the particle's trajectory with respect to the shock front. The energy gain is maximal for head-on collisions ($\theta = 0$). The energy E' of the particle in the downstream region compared to the energy on the upstream side E will be,

$$E' = \gamma(E + p_x v). \tag{2.18}$$

Under the assumption that the shock is non-relativistic $\gamma = 1$, but that the particle is relativistic ($E = pc$), the component of the momentum perpindicular to the shock is $p_x = (E/c)\cos\theta$. Averaging over all relevant angles one obtains:

$$\langle\frac{\Delta E}{E}\rangle = \frac{v}{c}\int_0^{\pi/2} 2\cos^2\theta\sin\theta d\theta = \frac{2}{3}\frac{v}{c}. \tag{2.19}$$

After one round trip, being scattered both upstream and downstream, the relative energy gain is $\langle\frac{\Delta E}{E}\rangle = \frac{4}{3}\frac{v}{c}$ which yields $\beta = 1 + \frac{4v}{3c}$. In the reference frame of the shock front, the upstream gas is floating towards the shock front at a velocity U, and swept away with $\frac{1}{4}U$ downstream. So the relativistic particles moving at a velocity c are advected away from the shock front at a rate $\frac{1}{4}NU/\frac{1}{4}Nc$. Hence, the escape probability is $P = 1 - (U/c)$, and together with $\ln\beta = \ln(1 + \frac{4}{3}\frac{v}{c}) \approx \frac{4}{3}\frac{v}{c} = \frac{U}{c}$, expanding the logarithm one obtains $\frac{\ln P}{\ln\beta} = -1$. Thus, the differential energy spectrum of the VHE particles reads:

$$N(E)dE \sim E^{-2}dE. \tag{2.20}$$

The plausibility of diffusive shock acceleration as the mechanism underlying the energy distribution of the relativistic particles has also been demonstrated by Rieger et al. (2007) [128]. While nonlinearities lead to spectral indices < 2 (Berezhko & Ellison, 1999 [41]), accounting for non-diffusive transport properties can lead to values up to ~ 2.5 (Kirk et al., 1999 [100]). Overall, the variety of the observed spectral indices can be explained by a combination of different acceleration mechanisms.

2.3.2 Exponential cut-offs

Many models of cosmic particle acceleration assume a maximal energy in the electron population at the source (e.g. Rieger et al. (2007) [128] have elucidated those limits of diffusive shock acceleration). Particle escape, the limited jet activity as well as radiative synchroton losses represent the main constraints for the acceleration of highly energetic particles in relativistic jets. The main parameter determining the cooling time and the maximal possible

Lorentz factor is the magnetic field strength.

Assuming a leptonic origin for γ-ray emission by Inverse Compton scattering, a sharp cut-off in the energy distribution of the electrons causes an exponential cut-off in the TeV spectrum. The synchroton radiation emitted by monoenergetic electrons at $E_{\max}$ will determine the shape at the high energy end of the spectrum. It is then upscattered by Inverse Compton processes to TeV energies.

The total spectral emissivity j of a single electron with a Doppler factor γ emitting synchroton radiation with a frequency ω is given as a function of the pitch angle α between the particle's trajectory (with a curvature radius a) and the magnetic field B. According to Longair (2011, p. 208) [106]:

$$j(\omega) = \frac{\sqrt{3}e^3 B \sin \alpha}{8\pi\epsilon_0 c m_e}. \tag{2.21}$$

For high energies ($x \gg 1$) this can be approximated by an exponential function:

$$F(x) = (\frac{\pi}{2})^{1/2} x^{1/2} \exp(-x), x \gg 1, \tag{2.22}$$

with $x = 2\omega a/3c\gamma^3$, where $F(x) = x \int_x^\infty K_{5/3}(z)dz$ is the integral over the modified Bessel function of order 5/3, $K_{5/3}$. The synchroton spectrum of a particle population following a power-law energy distribution is the convolution over the energies of the particles. In general, this is also a power-law. If the particle population has a maximal energy $E_{\max}$, then the high energy end of the synchroton spectrum is determined by the exponential cut-off of the electrons with energy $E_{\max}$. This spectral feature is naturally preserved by the Inverse Compton upscattering of the synchroton radiation photons to TeV energies. Therefore, the simplest case of a spectral feature is a differential energy spectrum which is described by a power-law with an exponential cut-off (Equation 2.10).

2.3.3   Modeling log-parabolic spectra

As has been shown by Massaro et al. (2006) [114] [141], a log-parabolic energy spectrum can be explained by an energy dependent stochastic scattering process. Compared to the classical scenario of Diffusive Shock Acceleration, in this case the condition that the acceleration probability is independent of energy is dropped. Instead it is assumed that the probability to accelerate to a higher energy is decreasing with the particle energy in each step of the acceleration mechanism. A decreasing confinement efficiency of the magnetic fields responsible for the acceleration is a possible reason for this scenario. In this case, the confinement efficiency is assumed to decrease for an increasing gyration radius.

Hence, the probability P_k for the particle to be accelerated again after $k-1$ acceleration steps is assumed to be a function of the particle's energy in that step k:

$$P_k = g/E_k^q, \tag{2.23}$$

where g and q are positive constants. The number N_k of particles accelerated k times then is,

$$N_k = N_0 \frac{g^k}{\prod_{j=0}^{k-1} E_j^q}. \tag{2.24}$$

Together with $E_k = \beta^k E_0$ one obtains,

$$\prod_{j=0}^{k-1} E_j^q = E_0^{kq} \prod_{j=1}^{k-1} \beta^{jq} = E_0^{kq} \beta^{q \times k(k-1)/2}. \tag{2.25}$$

Inserting this result yields,

$$N_k = N_0 \times \frac{g}{E_0^q}^k \beta^{q-k(k-1)/2}. \tag{2.26}$$

So the integral energy distribution is given by

$$N(> E) = N_0 \frac{E}{E_0}^{-(s-1+r\log(E/E_0))}, \tag{2.27}$$

with $s = -\frac{\log(g/E_0)}{\log \beta} - \frac{q-2}{2}$ and $r = \frac{q}{2\log \beta}$. This results in a differential energy spectrum,

$$N(E) = \frac{N}{E} \frac{d\log N}{d\log(E/E_0)} \Rightarrow \tag{2.28}$$

$$N(E) = \frac{N_0}{E_0} |s - 1 + 2r\log(E/E_0)| \times (E/E_0)^{-s-r\log(E/E_0)}. \tag{2.29}$$

This result is not a log-parabolic law. However, the difference is smaller than 10% over several decades in energy (see e.g. [113]).

2.3.4 Conclusions

In summary, a log-parabolic spectral shape can be motivated by an energy-dependent stochastic scattering process. The case of an exponential cut-off is even simpler. It can be explained by a maximal energy available in the source (e.g. due to synchroton cooling).

So far no alternative mechanisms for particle acceleration apart from stochastic acceleration at shock fronts have been discussed. Magnetic reconnection (e.g. Schopper et al., 1998 [134]) and shear acceleration (e.g. Rieger & Duffy, 2006 [129]) are alternative approaches leading to a larger variety of theoretically possible spectral indices and spectral features.

The measurement of spectral features is a useful tool to elucidate the physical mechanisms in the source. To date, curvature in TeV spectra has been observed from 3 sources (see also 2.1.3). The goal of this work is a systematic study of the capacity to detect spectral features with VERITAS and CTA (in Chapter 4), and an application of this method to the most prominent example: Markarian 421 (see Chapter 5).

Chapter 3

The VERITAS experiment

The Very Energetic Radiation Imaging Telescope Array System is an array of four imaging atmospheric Cherenkov telescopes located at the Fred Lawrence Whipple Observatory, in southern Arizona ($31° \ 40'$ N $110° \ 57'$ W), 1268 m above sea level (for a status report see Holder et al., 2011 [94]). It is a γ-ray observatory sensitive in the energy range from 85 GeV to 30 TeV. The energy dependent angular resolution and energy resolution reach $0.1°$ and 15% respectively for γ-ray primaries of 1 TeV.

Each of the four VERITAS telescopes consists of a 12 m diameter reflector equipped with 350 mirror facets. A 499-pixel photomultiplier tube (PMT) camera is placed at the focus of the reflector, covering a field of view of $3.5°$.

In Section 3.1, the imaging atmospheric Cherenkov technique, by means of which VERITAS detects γ-rays, is introduced. The VERITAS array is described in Section 3.2.

3.1 Imaging atmospheric Cherenkov technique

An air shower of highly relativistic particles is initiated by the γ-ray due to pair creation in interactions with the atmosphere. This particle cascade emits Cherenkov radiation under a small angle of less than $\lesssim 1.38°$. This light can be detected by Cherenkov telescopes on the ground. The imaging atmospheric Cherenkov technique concerns the indirect detection of γ-ray primaries by means of this Cherenkov light foot print. The principle of the technique is the measurement of the shape of the particle air shower with multiple telescopes. The direction of the Cherenkov light cone allows the reconstruction of the origin of the γ-ray primary. Furthermore, from the size of the shower and the number of Cherenkov photons reaching the ground, one can infer the energy of the γ-ray.

The physcis underlying the development of the particle air shower is briefly discussed in Section 3.1.1. The mechanism of emission of Cherenkov radiation by relativistic particles is introduced in Section 3.1.2. Finally, the principle of stereoscopic measurement by multiple telescopes is illustrated in Section 3.1.3.

3.1.1 Particle air showers

High energy cosmic ray hadrons and γ-ray photons constantly hitting the earth's atmosphere interact with the molecules of the air, generating a cascade of secondary particles. This cascade of relativistic particles approaching the ground is called an air shower.

In a first step, the energy of a primary γ-ray photon is converted into secondary particles by pair production. A shower maximum in the number of secondaries is reached when ionisation losses of the electrons start to dominate over bremsstrahlung processes, and the shower energy is absorbed by the atmoshphere.

The particle air shower can have different components. While γ-ray photons interact electromagnetically, only the interaction of hadrons with the atmsophere can have both an electromagnetic and a hadronic component.

Electromagnetic shower

Considering a γ-ray primary, the dominating cross-section for the first interaction is given by pair production. Hence an electron-positron pair will be created. The direction of the primary γ-ray is approximately preserved in the shower (due to a low transversal momentum p_T transfer), and the origin of the primary photon can be inferred from the shower orientation.

In a next step, the electrons and positrons interacting with the electromagnetic field of a charged atomic nucleus emit a bremsstrahlung photon. Those two processes, pair production and the emission of bremsstrahlung, are iterated in an electromagnetic particle avalanche. When the electrons on average reach the critical energy $E_C = 80$ MeV, the dominating process will be the energy loss of the electrons due to the ionisation of the ambient air molecules. At this point, the shower has reached its maximum particle number, and from here on, it becomes attenuated as increasingly more particles fall below the energy threshold for particle production.

Hadronic showers

In contrast to γ-ray photons, cosmic ray nuclei hitting the earth's atmosphere scatter inelastically. Due to the higher transversal momentum p_T transfer in hadronic interactions, the shape of the air shower is more irregular for cosmic ray primaries compared to γ-rays.

Secondary hadrons are produced, by the inelastic scattering on the nuclei in the air. These can be mesons, such as pions and kaons, or similarily nucleons, such as neutrons and protons. Therefore, the core of the shower consists of hadrons. Furthermore, approximately after each hadronic interaction length, one third of the energy gets lost to an electromagnetic shower component via decay of the mesons. For example, neutral pions immediately decay into two photons. The remaining two thirds of the energy persist in the hadronic core leading to a multiplication of hadrons via interaction with the atmosphere. This avalanche continues until a critical energy is reached, where the decay of mesons into muons becomes dominant. Overall, the air shower induced by cosmic ray hadrons consists of a hadronic core, a muonic component and electromagnetic sub-showers. This is illustrated schematically in Figure 3.1.
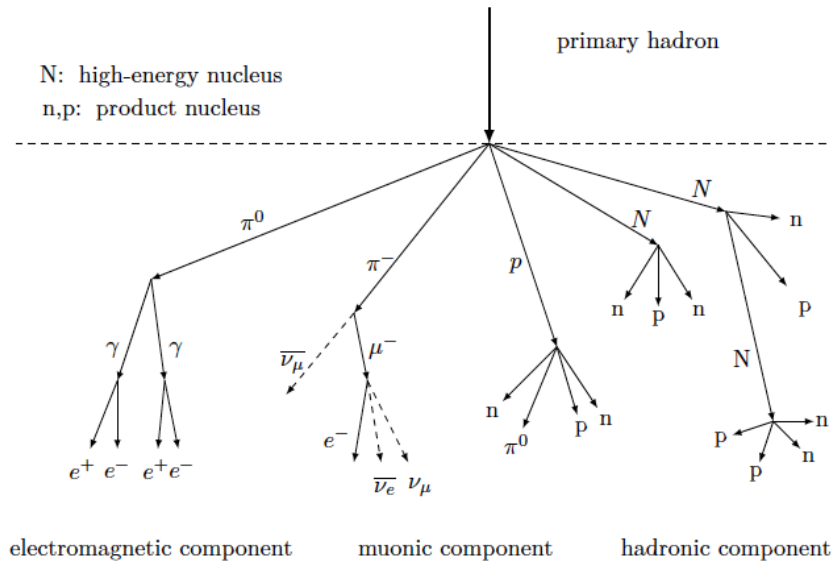
Figure 3.1: Schematic illustration of a hadronic air shower which is caused by a primary cosmic ray particle. Picture taken from Prokoph (2013) [123].
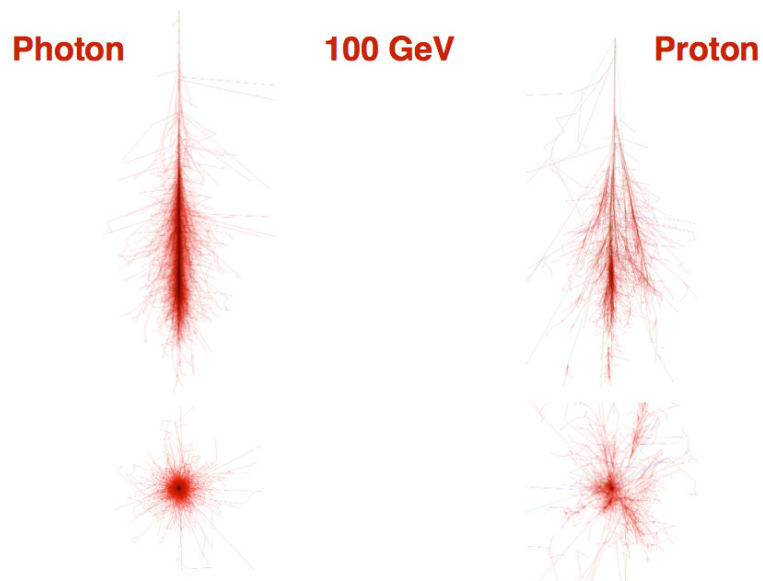

Figure 3.2: CORSIKA air shower simulations of a 100 GeV primary particle. The upper part depicts the development of the air shower along the longitudinal axis (image from 0 to 30 km, xz-projection with first interaction height fixed to 30 km), while the lower images depict the lateral plane (xy-projection ± 5 km around shower core). Air showers of a photon (left) and a proton (right) are shown. Red particle tracks are electrons, positrons and γ-rays. Muons are displayed in green. Hadron trajectories are blue. Picture taken from Schmidt (2005) [133].

In general, air showers initiated by a photon have a more regular shape, compared to those caused by hadrons, as is shown in Figure 3.2. This difference in the shower structure allows

discrimination between the two types of showers.

3.1.2   Cherenkov radiation

Since most of the secondary particles in the air shower have highly relativistic speeds beyond the phase velocity of light in the atmosphere, Cherenkov radiation [54] is emitted. This Cherenkov radiation is the foot print by which the properties of the primary particle can be measured. Because the Cherenkov light is emitted in a narrow cone around the trajectory of the particles, the total Cherenkov light cone points to the direction of the γ-ray primary.

The angle θ under which the Cherenkov radiation is emitted is a function of the velocity v of each particle. Defining the speed relative to the speed of light $\beta = \frac{v}{c}$, with c being the speed of light in vacuum, the emission angle θ is given by

$$\cos\theta = \frac{1}{\beta n}. \tag{3.1}$$

Here, $n = \frac{c}{c'}$ is the refractive index which is equal to the ratio of the speed of light in vaccuum c to the speed of light in the medium (air) c'.

Cherenkov emission can only take place for $\beta > \frac{1}{n}$. This results in a minimum particle energy $E_{\min}$ necessary for Cherenkov emission. From $\beta_{\min} = \frac{1}{n}$ it follows that:

$$E_{\min} = \frac{mc^2}{\sqrt{1 - \beta_{\min}^2}} = \frac{mc^2}{\sqrt{1 - n^{-2}}}. \tag{3.2}$$

Since the density of air decreases with altitude the refractive index and therefore also the threshold energy are increasing with altitude. The mass dependence shows that heavy particles, like muons or protons, must be more energetic than light particles, like electrons or positrons, in order to emit Cherenkov light. Therefore, the electromagnetic shower component dominates the Cherenkov light cone.

The number of photons of wavelength λ emitted per wavelength band of the Cherenkov light $d\lambda$ and path length dx of the particle's trajectory is given by the Frank-Tamm [138] formula:

$$\frac{d^2N}{dxd\lambda} = \frac{2\pi Z^2 \alpha}{\lambda^2} \left(1 - \frac{1}{\beta^2 n^2(\lambda)}\right). \tag{3.3}$$

Here Z is the charge of the particle in units of the elementary charge e, and α denotes the fine structure constant.

The refractive index n is not constant, but instead a function of the density of the atmosphere and hence also of the height. Therefore, the angle θ under which the Cherenkov light is emitted depends on the altitude h. Assuming an isothermal atmosphere it is possible to use the barometric formula. Since $n - 1$ is proportional to the density of the gas, one therefore obtains:

$$n = n(h) = 1 + \eta_0 \times e^{-h/h_0}, \tag{3.4}$$

with the constant $\eta_0 = 2.9 \times 10^{-4}$ and the scale height $h_0 \approx 7.1$ km[1].

From this it can be seen that the emission angle θ is small at high altitudes, where the refractive index is close to unity, and increases to about $\theta \approx 1.38°$ at sea level. The resulting light pool on the ground is a superposition of the light cones of Cherenkov radiation emitted along the trajectory of the relativistic particle. This is illustrated in Figure 3.3.
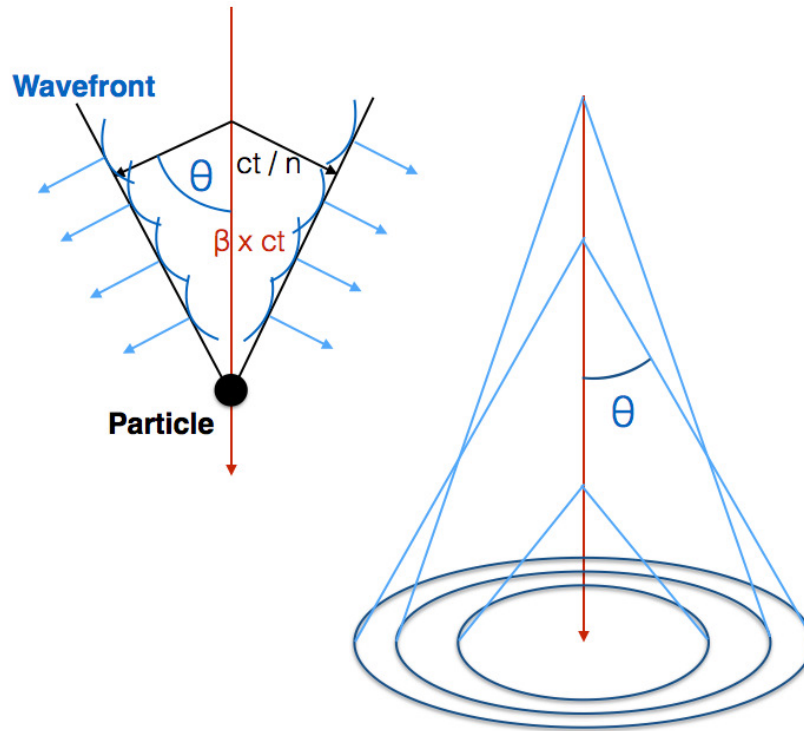

Figure 3.3: Schematic illustration of the emission of Cherenkov radiation (blue) along the trajectory (red) of a relativistic particle. The light is emitted in a cone with an angle θ to the direction of the particle. The light corresponding to each point of the particle's trajectory is represented by an ellipse on the ground. The increase of the refractive index along the trajectory of the particle leads to an increase of the emission angle θ to a value of $\sim 1.38°$ at sea level. Therefore, the superposition of all the light emitted along the track of the particle results in the typical Cherenkov light profile on the ground.

The intensity of the Cherenkov light cone depends on the number of particles in the shower and hence on the energy of the primary (γ-ray). Furthermore, a fraction of the initial Cherenkov radiation is absorbed and scattered in the atmosphere. The dominating processes are absorption due to excitation of molecules, Rayleigh scattering on molecules and Mie scattering on aerosols[2].

The number of Cherenkov photons reaching the ground is proportional to the energy of the pri-

---

[1]The scale height is given by $h_0 = \frac{kT}{Mg}$, where k is the Boltzmann constant, T the mean atmospheric temperature, M the mean molecular mass of dry air and g the acceleration due to gravity.

[2]Rayleigh scattering is an approximative process, describing elastic scattering of light by spheres which are much smaller than the wavelength of light. In contrast, Mie scattering is an approximation valid for spheres much larger than the wavelength of light.

mary. For a 1 TeV γ-ray, ~ 100 photons / m^2 can be measured at the altitude of the VERITAS experiment.

3.1.3 Stereoscopic measurement by telescopes

Imaging atmospheric Cherenkov telescopes (IACTs) use the earth's atmosphere as a calorimeter. In the case of the VERITAS experiment the 4 telescopes are seperated by a distance (~ 100 m) matching the size of the Cherenkov light pool of ~ 150 m radius. This allows the stereoscopic measurement of the Cherenkov light cone from the air shower with an effective collection area of $\sim 10^5$m^2. The detection principle of imaging Cherenkov telescopes is illustrated schematically in Figure 3.4.
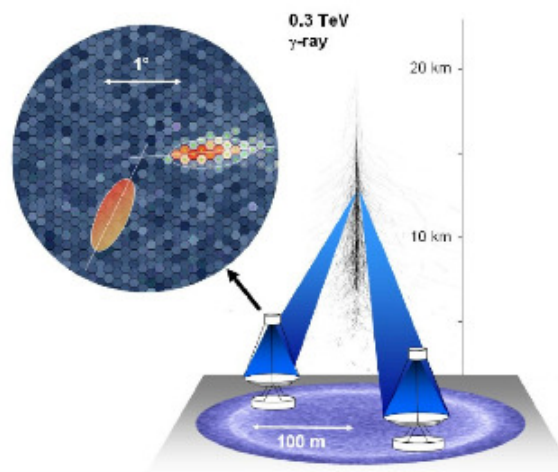
Figure 3.4: Detection principle of γ-ray astronomy using IACTs: An electromagnetic particle cascade is caused by a 300 GeV photon primary. The IACT, located inside the Cherenkov light pool, reflects the Cherenkov light from the air shower onto the camera. This camera, consisting of photo-multiplier tube pixels, is located in the focal plane of the telescope. The camera image of the detected photons (upper left), can be parameterized by an ellipse. Stereoscopic measurement means that multiple images of the same event can be overlaid in the camera coordinate system to reconstruct the shower direction by intersection of the elongated axis of the elipse. Picture taken from Hinton & Hofmann (2009) [90].

The Cherenkov light emitted by the charged air shower particles is collected by mirror facets and reflected onto a camera in the focal plane of the telescope. For a 100 GeV γ-ray air shower only 10 photons / m^2 reach the ground. The large total area of the mirrors (~ 100m^2) allows the collection of a sufficient amount of light.

The VERITAS cameras consist of 499 photomultiplier tubes (PMTs). The PMTs are designed so that they provide a sufficient resolution of the elliptical image of the Cherenkov light cone, which is elongated along the shower axis. Furthermore the PMT size allows for efficient suppression of night sky background (NSB).

The simultaneous stereoscopic measurement of the air shower by two or more telescopes [101] allows for a better reconstruction of the shower shape. This results in a better energy resolution and angular resolution due to the different viewing angles of the air shower. Additional advantages of the stereoscopic approach are the larger effective collection area and the better sensitivity[3].

3.2   The VERITAS array

VERITAS started operating with a single telescope in early 2005. The complete array of four IACTs has been taking data since summer 2007. A major enhancement in the continuously improved VERITAS sensitivity occured in summer 2009, when one of the telescopes was transferred to a new position. The relocation of this telescope led to comparable distances of ~ 100 meters between the four telescopes. The rectangular symmetry of the array thus established led to an increase in sensitivity of about $\sim 30\%$. Further improvements were achieved by upgrades of the trigger system and a complete camera upgrade. A faster pattern trigger has been in operation since fall 2011, and in summer 2012, the PMTs of all cameras were replaced. The quantum efficiency of the new Hamamatsu PMTs, comprising new super-bialkali photo cathodes, is significantly higher than in the old Photonis PMTs with classical bialkali photo cathodes, which were in use before.
Currently, VERITAS can detect a source of 1% the flux of the Crab Nebula in 26 h with a significance of 5 standard deviations. The VERITAS array of 4 telescopes, before and after the move of one of the telescopes in summer 2009 is shown in Figure 3.5.

---

[3]This is due also to a better background rejection. For a review see Fegan (1997) [64].

(a) 4 VERITAS telescopes pre-upgrade

(b) 4 VERITAS telescopes post-upgrade

Figure 3.5: The array of 4 VERITAS telescopes before (a) and after (b) the relocation of one of the telescopes in summer 2009. Credit: VERITAS collaboration.

### 3.2.1 The VERITAS telescope hardware

Each individual VERITAS telescope consists of a 12 m diameter telescope dish composed of 350 hexagonal mirros. The camera is held in the focus of the telescope by an optical support structure. Additional hardware components include the trigger system and the data acquisition (DAQ) system. For a detailed description see Holder (2006) [93].

Mechanics

The central mechanical components of the VERITAS telescopes are the altitude-over-azimuth drive and the optical support structure (OSS), which is made of tubular steel. The camera is supported by a quadrupod arm, and its load is balanced by a counterweight structure [93]. The maximum slew speed of the telescope drive is about one degree per second with a pointing

accuracy typically better than $< 0.01°$ [93].

Optics
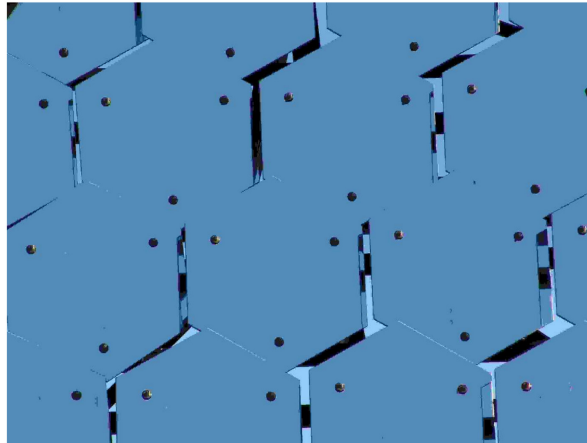
(a) VERITAS mirrors
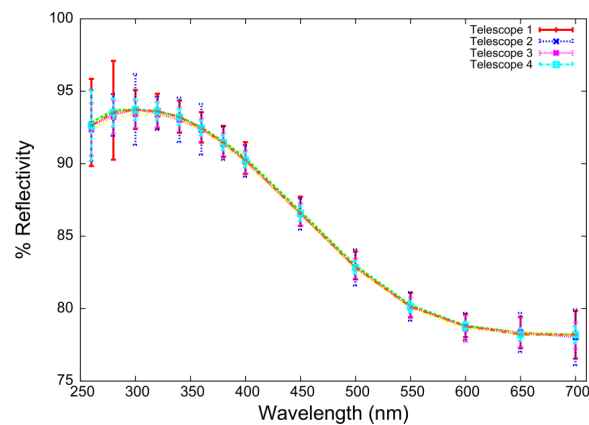
(b) Mirror reflectivity

Figure 3.6: (a) Picture of the VERITAS telescope mirror facets, taken from [93]. The black dots are the three adjustment points used for alignment.
(b) VERITAS telescope mirror reflectivity versus wavelength for each individual telescope. Image taken from Roache et al. (2008) [130]. The design-specified reflectivties of 90% at 320 nm and better than 85% between 280 nm and 450 nm are achieved.

The VERITAS telescopes are designed according to the principle described by Davies and Cotton (1957) [58], with a 12 m reflector and 12 m focal length. In this design, the identical mirror facets have spherical curvature of radius equal to twice that of the overall dish. This leads to improved off-axis imaging. The 350 hexagonal mirror facets, each with an area of 0.322 m^2, are mounted on the OSS covering a total area of 110 m^2. The hexagonal shape of the mirrors allows the entire surface of the dish to be used.
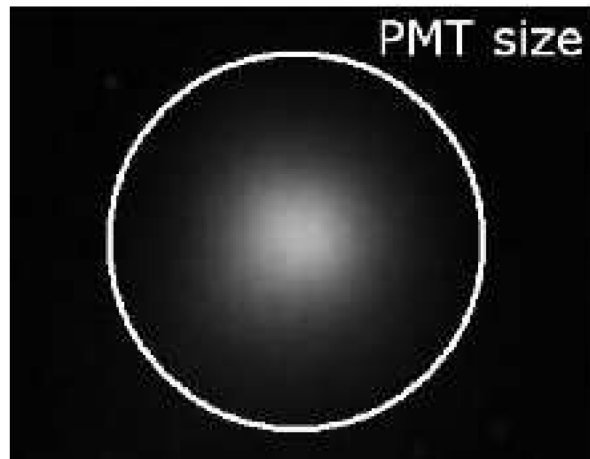
(a) PSF

(b) Camera

Figure 3.7: The upper image (a), taken from [93] shows a picture of Polaris taken with a CCD camera in the focus of the telescope. For comparison, the size of a VERITAS PMT (0.15° diameter) is shown as a white circle. The size of the PMT, compared to the mirror PSF allows point sources to be resolved as seen in the image of Polaris.

(b) The lower image (also taken from [93]) shows the 499 PMT camera. The box housing the camera is 1.8 m square. During daylight hours the box can be closed with a shutter for protection.

The mirrors are made of glass, coated with aluminium (see Figure 3.6 (a)). Their reflectivity at normal incidence is characteristically > 90 % at 320 nm, and typically better than > 85 % between 280 nm and 450 nm [130]. Figure 3.6 (b) shows the functional dependence of the reflectivity on wavelength.

The mirrors facets have a 24 m radius of curvature with 1% accuracy. By means of a triangular frame, they are installed on the front surface of the OSS. An accurate manual alignment is possible by means of three alignment screws, such that the mirror facets act together as a single dish. The point spread function (PSF) is a measure of this optical property. It describes the

reaction of the optical system to a point of light at infinite distance. The 80% light containment radii of the PSFs are below $0.05°$ at elevations above $30°$ [115] (see Figure 3.7).

Camera electronics

The front of the camera box situated in the focal plane of the telescope is shown in Figure 3.7. The box in which the 499 PMTs of the imaging camera are housed is square with a side length of 1.8 m. Before the camera upgrade, the pixels consisted of Photonis 2.86 cm diameter, UV sensitive PMTs. The angular pixel spacing is $0.15°$ covering a total field-of-view of diameter $\sim 3.5°$. Winston light cones have been installed in front of each PMT. These help to reflect photons that would otherwise be lost in the space between the pixels onto the sensitive area of the PMTs, increasing the total photon collection efficiency.

The high voltage supply is controlled individually for each PMT. It is adjusted (characteristic values range from 700 to 800 V) such that the resulting PMT gain is of the order of 2×10^5. The PMT signals are intensified by a high-bandwidth pre-amplifier, which is built into the base of the PMTs. The pre-amplifiers also permit monitoring of the PMT anode currents. The PMTs characteristically operate with anode currents of 3 μA for dark fields, up to 6 μA for bright fields. This corresponds to a night-sky photoelectron background of 100-200 MHz per PMT at the VERITAS site. Finally, the PMT output signals are sent to the control room, which houses the telescope trigger and data acquisition system.

In summer 2012, the Photonis PMTs of the camera were completely replaced by significantly faster Hamamatsu PMTs. Therefore the pulse shape and photon detection efficiency changed. The pulse shape of the Hamamatsu PMTs (4.2 ns) is almost 40 % narrower than the previous 6.8 ns full width at half maximum (FWHM). This results in improved signal-to-noise ratio in the trace analysis.

Furthermore, the quantum efficiency improved significantly. At 320 nm, about 23% of photons were detected before the camera upgrade. This value increases to 34% for the new Hamamatsu PMTs.

Trigger

The aim of the trigger system is to reduce the amount of data to be stored for later offline analysis. It filters out the relevant γ-ray events from the background events of the Night Sky Background (NSB) and from local muons. VERITAS operates with a three level trigger system. For a review, see [148].

The first trigger level (L1) operates on the level of individual pixels. A constant fraction discriminator (CFD) [76] only triggers events with a signal strength exceeding a programmable threshold. The CFD allows for precise timing between trigger channels in order to reduce the coincidence time and hence lower the detector energy threshold. The CFD output signal is a logic pulse with a width of 10 ns. Each channel is equipped with a programmable delay which can take into account systematic differences in the relative signal paths due to different cable length and the voltage-dependent PMT transit times. A rate feed-back (RFB) circuit

automatically increases the effective threshold when the noise level rises. It provides real-time optimization of the CFD performance under variable NSB conditions with a jitter < 1 ns with background noise values up to 0.8 pe/ns.

The CFD output signals are sent to a trigger system (L2) working on the camera level. This topological pattern trigger selects events with more compact γ-ray-like Cherenkov light images and further suppresses the rate of triggers due to fluctuations of the NSB. The standard pixel coincidence requirement is 3 adjacent pixels within a patch. The necessary overlap time between adjacent CFD (L1) trigger signals typically is ~ 6 ns. The pattern trigger was upgraded in fall 2011, in view of the camera upgrade and increased trigger rates.
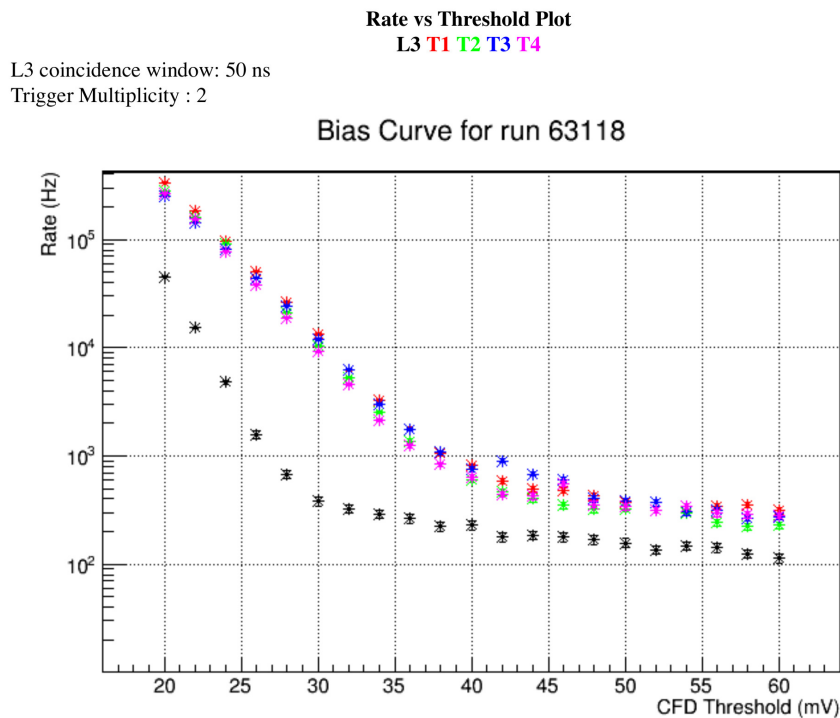
Figure 3.8: Bias curve taken during dark conditions. The trigger rates are displayed as a function of the CFD threshold. The black crosses are the L3 trigger rates. The colors represent the L2 trigger rates of the four telescopes (T1: red, T2: green, T3: blue, T4: magenta). The steeply falling NSB rate at very low thresholds can be identified. The rate above 30 mV is dominated by cosmic rays.

The final trigger stage (L3) combines the L2 outputs from the individual telescopes on the array level. Typically two or more telescopes are required to send a L2 signal within 50 ns. The L3 trigger then initiates the DAQ system to record the event. During the time of the readout of the buffer by the DAQ system, no new event can be triggered. This leads to a dead time of the system. It is of the order of 10% for an L3 trigger rate of 250 Hz (to 15% after the camera upgrade with trigger rates of 400 Hz). Events that are consistent with a simultaneous observation of an air shower in multiple telescopes are identified by the L3 trigger. In contrast,

the background from muons which dominates at low energies, is significantly reduced. This allows the CFD threshold to be further lowered, hence also lowering the energy threshold of γ-ray observations.

The choice of the CFD threshold is a compromise between a low energy threshold and a small contribution from the NSB. The best trigger settings are selected following calibration runs. These so-called bias-curves study the L2 rates of each camera and the overall L3 rate as a function of the L1 CFD threshold. Figure 3.8 shows an example bias curve. The optimal L1 trigger CFD threshold is at the point where the curves from the steeply falling rate from NSB fluctuations and the relatively flat rate due to cosmic ray background intersect. Typical values for the CFD thresholds of the individual pixels are 45 - 50 mV for dark sky conditions. This matches approximately 4 - 5 photoelectrons.

Data Acquisition

VERITAS runs a multi-stage DAQ chain. In a first step, the 500 Mega-sample per second flash analog-to-digital converter (FADC) electronic signals are read out by means of Versa Module Europa bus crates (VME). Then the single telescope events are reconstructed, and finally the data from each individual telescope is assembled at the array level (see [78]). In general, the data acquisition system permits the L1 triggers and the FADCs to be individually programmed. The task of the FADCs is to digitize the analog output from the PMTs [126]. This digital information is steadily saved by a ring buffer with a memory depth of 32 μs. Each L3 trigger signal initiates the read out of the PMT signal from the corresponding part of this buffer (characteristically 32 to 48 ns). For signals exceeding the 8-bit range of the FADC, it is switched from the standard high-gain path to a delayed low-gain path with a dynamic range increased from 256 to 1500 digital counts (dc). A telescope-level event-building computer then processes the data from the FADCs. The entire information from the events is assembled, checked, and sent to a data harvester machine. At the harvester computer, the telescope-level event information is completed with array-level information from the L3 (e.g., event numbers and timing information). The data is archived for later analysis in a customized VERITAS data format.

3.2.2 Experimental setup and calibration

The goal of calibrations is to allow the accurate interpretation of the PMT signals. It is necessary to know the conversion factor by which the light of a single photon translates to the number of digital counts in the electronics chain. Hence, the absolute calibration consists of measuring the signal size produced by a single photon, which is used as an input in Monte-Carlo simulations. This factor is crucial for the correct energy reconstruction and the understanding of the detector response. Relative calibration can be undertaken more easily on a daily basis, and is concerned with the variations between the individual PMT-channels.

Absolute calibration

The total photon conversion factor of the telescope results from the mirror reflectivity, the collection efficiency and the quantum efficiency of the PMT photocathode. Additionally, the conversion factor of the electronics chain has to be taken into account. The mirror reflectivity and PMT photocathode properties can be measured in the laboratory; the conversion factor of the number of FADC counts for a single photon is measured in situ. By simultaneously and uniformly illuminating the camera with a LED flasher system, the absolute gains of the PMT-channels can be determined. The two methods to calculate the absolute gains are photostatistics and single photoelectron measurements. They are described in full by Hanna et al. (2010) [77]. The Photostatistics method assumes a Poissonian distribution for the number N_{pe} of photoelectrons. From the mean digital counts $\mu = G N_{\mathrm{pe}}$ and the standard deviation $\sigma = G\sqrt{N_{\mathrm{pe}}}$, the absolute gain G can be calculated.

The standard method to determine the absolute gain, however, is to extract the position of the single photoelectron peak in the pulse-size spectrum. A significant number of single photoelectron events are obtained by mounting a plate in front of the camera with a small hole for each PMT which allows only single photons to pass.

Relative calibration

The same LED flasher system which permits calculation of the absolute gains is also used to measure channel-to-channel deviations within a given camera. So called flasher runs are taken each night (typically lasting less than 5 minutes) to measure the time differences and relative gain variations within each camera. The time differences can be caused by electronic delays and different cable length. The relative gain is a function of the power of the Winston cone light concentrators, the quantum efficiency of the photocathode, and the gain of each PMT. The relative gains can be obtained by a linear interpolation of the PMT signal between different light intensities of the LED flasher.

3.2.3   Data analysis

The analysis presented in this thesis is carried out with the software package EVENTDISPLAY. EVENTDISPLAY was originally developed to display the VERITAS prototype data. It was implemented by Gernot Maier (DESY) and Jamie Holder (University of Delaware), and has since become a full analysis package used by the VERITAS collaboration. The VERITAS data analysis employs Monte-Carlo (MC) simulations to interpret and model the measured electronic PMT signals and to reconstruct the energy and direction of the primary γ-rays from the detected Cherenkov light.

Monte-Carlo simulations

The simulation chain can be divided into two stages. First of all, the development of the air shower and the propagation of the Cherenkov light in the atmosphere is simulated. In the

second stage, the detector response to the Cherenkov photons emitted by the air shower is modeled.

The simulation of the air shower development with the CORSIKA program (version 6.960, Heck et al., 1998 [79]) comprises the emission of Cherenkov light, using the IACT option [44]. Only Cherenkov light crossing fiducial spheres around the detector posisition is recorded in these simulations. The parameters specific to the VERITAS array, e.g. the altitude, geomagnetic field and telescope positions, are taken as an input. After the simulation of the shower, corrections for atmospheric extinction are applied to the Cherenkov light. These corrections have a systematic uncertainty of about 15% due to differences of the local atmosphere with respect to the assumed atmospheric profile. Two different atmospheric profiles taking into account seasonal variations between summer and winter are used.

The spatial extent and intensity of the Cherenkov light pool observed by the telescopes are a function of the energy of the γ-ray primary, the direction of the incident particle, and the distance of the telescopes to the impact point with respect to the shower axis. Therefore, the shower simulations cover the full range of azimuth angles. This is also important because the dependence of the shower development on the geomagnetic field at the VERITAS site is non-negligible and differs for different azimuth angles. Furthermore, ten steps in zenith angles ranging from $0°$ to $65°$ are simulated. The maximal distance of the impact point to the array center is 750 m. The energy of the primary γ-rays, simulated on the energy range from 30 GeV to 200 TeV, follows an E^{-2} spectrum. In the analysis, this discrepancy of the simulated power-law to the spectrum of the source is corrected for by reweighting the MC events.

The modeling and simulation of the detector response is performed with the GrISU software package[4]. This is a two-part-process. The first part includes the optical propagation of the Cherenkov photons from the mirrors to the PMTs. The mirror reflectivity, as well as shadowing effects from the optical support structure, are taken into account by ray-tracing.

The second stage is concerned with the camera response and the electronics chain. The single photoelectron pulse digitized by the FADC is simulated. Four different noise levels of the NSB are then introduced to the digitized FADC trace of 2 ns samples. Finally, the trigger is simulated. For the single-pixel level L1 trigger, this happens with a simplified[5] version of the CFD and a standard trigger threshold of 50 mV. The pattern trigger and the L3, however, are fully realized in the simulation. The detector simulation is estimated to have a systematic uncertainty of $\sim 15\%$.

Shower image and Hillas parameters

The parameterization of the shower image is done in three major stages: the trace analysis, the image cleaning, and the Hillas parameterization.

The first step consists of the integration of the total charge measured by the FADC trace in each

---

[4]http://www.physics.utah.edu/gammaray/GrISU

[5]The CFD model is consistent with data above the energy threshold. In contrast, at low energies the NSB significantly contributes to the trigger. This is taken into accound by a new simulation package: CARE (CAmera and REadout; http://www.gtlib.gatech.edu/pub/IACT/CARE.git)

pixel. In order for the NSB[6] contribution to be as small as possible, a two-step *double-pass method* (for a detailed description see Holder (2005) [92]) is applied. First of all, a default integration window of 18 samples (with a 2 ns sampling) is implemented to compute arrival times and the total charge of the FADC trace. In a second step, this information is used to narrow the integration window to typically 7 or 12 samples in order to obtain a better signal-to-noise ratio.

After the integration of the total charge in each pixel, an image cleaning algorithm is applied. This algorithm determines which pixels are identified as parts of the shower image, and there-fore, should be taken into account in the parameterization of the shower image. This is done by comparing the charge of the pixel to the RMS of the trace from so called pedestal events (*pedvar*), caused by the NSB. Pixels with a charge exceeding 5 times the pedvar are identified as *image pixels*, and all neighbouring pixels of the chosen image pixels exceeding 2.5 times the pedvar are selected as *border pixels*. Border pixels together with image pixels which are not isolated from the main image constitute the image of the Cherenkov light shower.

Parameter	Definition	Physical significance
size	Total integrated charge of all pixels contained in the image	Function of the energy of the primary particle
width	RMS of the charge distribution along the minor axis of the image	Projected lateral shower development
length	RMS of the charge distribution along the major axis of the image	Projected longitudinal shower development
centroid	Coordinates of the center of the gravity of the shower image in the camera	
distance	The distance of the image centroid from the center of the field of view of the camera	
fui	The fraction of charge of the image within the image ellipse	Relevant to remove less compact images
loss	The fraction of charge of the image contained in the edge pixels	Relevant to remove truncated images at the camera edge

Table 3.1: Hillas Parameters of the shower image in the camera. The parameter name is listed together with a short characterization. Adapted from Prokoph (2013) [123].

When the shower image has been identified, it can be parameterized. This means the image is fit with a model of the so-called Hillas parameters [88]. The shape and the orientation of the image in the camera can be characterized by these parameters. They are calculated according

---

[6]The fluctuations from the NSB are permanently digitized and therefore contribute to the total charge in the FADC trace.

to the definitions given in Fegan (1997) [64]. The Hillas parameters are described in Table 3.1.

The Hillas parameters provide a useful set of criteria according to which γ-ray events can be extracted while suppressing the cosmic ray background by means of so-called γ-hadron cuts. Additionally, quality cuts are applied on the loss parameter (loss $<$ 0.5) to exclude images at the edge of the camera, which are difficult to reconstruct properly. Further quality requirements are a minimum number of image/border pixels of at least 4 and a minimum image size of 600 digital counts (dc).

Event reconstruction

The major properties of the incident γ-ray primary are its energy and direction. The direction can be reconstructed from the geometry of the shower (by the stereoscopic approach introduced in Section 3.1.3). The energy reconstruction makes use of shower simulations with known (true) energy in addition to the geometrical parameters.
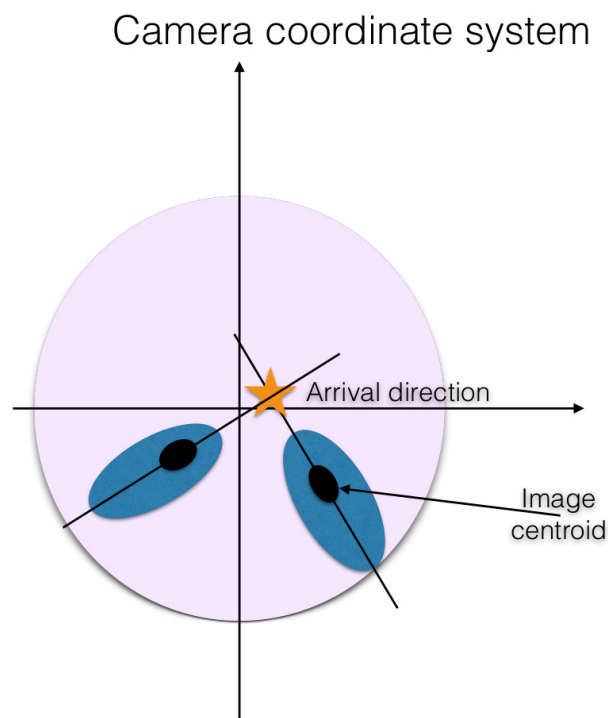
Figure 3.9: Reconstruction of the direction of an air shower: The stereoscopic approach is to superimpose the camera images and then to intersect the major axes derived from the Hillas parameterization. This allows the reconstruction of the origin of the γ-ray in the camera coordinate system.

The stereoscopic reconstruction of the shower geometry using the image parameters corresponds to Algorithm 1 in Hofmann et al. (1999) [91]. The reconstruction of the direction is illustrated in Figure 3.9. For all pairs of telescopes, the major image axes, defined by the

Hillas parameters, are superimposed in the camera coordinates and intersected to determine the direction. The resulting intersection points are averaged and weighted with the sine of the angle between the image axes. The weight takes into account the uncertainty in intersections with small angles.

The position of the shower core is obtained by intersecting the major image axes in the shower plane. The major image axes are elongated along the line from the telescope positions to the location of the core of the shower, where they cross (see Figure 3.10). The distance of the shower core location to the individual telescopes positions is called the *impact parameter R*. Since the images of very distant showers are rather parallel, the angular resolution worsens for large impact parameters. Therefore, a cut on the shower core position is imposed, and all events more than 250 m away from the array center are discarded.

Furthermore, the *emission height* of the shower is reconstructed as described in Aharonian et al. (1997) [20]. The emission height is the height at which the air shower development attains the point with the maximal number of particles emitting Cherenkov radiation.
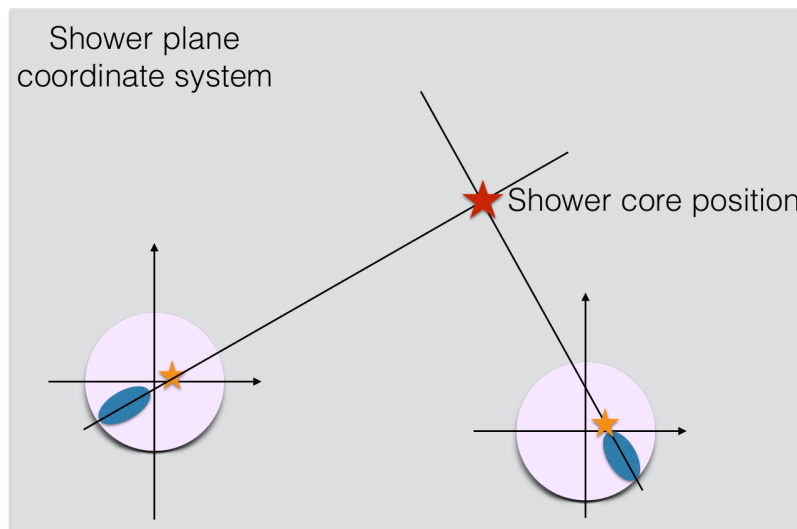
Figure 3.10: Reconstruction of shower core position: The major axes from the Hillas parameterization between the telescopes are intersected in the shower plane. This allows the calculation of the impact parameter: the distance of the shower core to the individual telescopes, resp. the array center.

In order to reconstruct the energy, the proportionality of the number of Cherenkov photons to the energy of the γ-ray primary is used. Hence, given that the observational conditions, directions and impact parameters are the same, the energy is proportional to the total charge of the image: the *size s*. To account for these parameters, MC simulations are performed for the complete parameter space. For a given energy of the primary γ-ray and a given impact parameter, so-called *lookup tables* are filled with the median and the 90%-width values of $\log s$. This allows the energy of the γ-ray primary to be estimated based on the images in each

telescope. From the energy estimates in the individual telescopes, an average energy E_{event},

$$E_{\text{event}} = \frac{\sum_{i=1}^{N} E_i / \sigma_i^2}{\sum_{i=1}^{N} 1 / \sigma_i^2}, \qquad (3.5)$$

is derived, based on the median value E_i of the MC distribution, weighted with the 90%-containment value σ_i, in each individual telscope.

The simultaneously calculated χ^2-value of E_{event},

$$\chi^2(E_{\text{event}}) = \frac{1}{N-1} \sum_{i=1}^{N} \left(\frac{E_{\text{event}} - E_i}{\sigma_i^2} \right) \qquad (3.6)$$

provides a criterion by which cuts for γ-hadron separation can be established. Since hadronic showers are more irregular, the energy estimates in individual telscopes will show a larger variation for cosmic ray primaries leading to a larger χ^2.

γ-Hadron separation and background

Since cosmic hadrons and other background events are thousands of times more numerous than air showers initiated by γ-rays, the major challenge for IACTs is to discriminate these background events from the signal. This can be achieved by cuts on the image shape and the arrival direction of the events.

The Hillas parameterization defines the width and the length of the image. These width and length parameters are compared with MC simulations to identify the expected γ-ray like values. Since the width and length are a function of the energy of the primary particle, the direction and impact parameter, as well as the contribution of the NSB, lookup tables as in the case of the energy reconstruction are employed. The lookup tables are filled with the median and the 90%-containment width (w_{MC}, σ_{MC}^w) and length (l_{MC}, σ_{MC}^l) values for a given impact parameter R and image size s. The γ-hadron separation is then applied on the deviation between measured width (width$_i$) and length (length$_i$) in each image i, and the simulated value of the particular event. The relevant parameters are called mean-scaled with (MSCW) and mean-scaled length (MSCL), and are defined in the following:

$$MSCW = \frac{1}{N_{\text{images}}} \sum_{i=1}^{N_{\text{images}}} \left(\frac{\text{width}_i - w_{\text{MC}}(R,s)}{\sigma_{\text{MC}}^w(R,s)} \right), \qquad (3.7)$$

$$MSCL = \frac{1}{N_{\text{images}}} \sum_{i=1}^{N_{\text{images}}} \left(\frac{\text{length}_i - l_{\text{MC}}(R,s)}{\sigma_{\text{MC}}^l(R,s)} \right). \qquad (3.8)$$

According to this definition, the mean-scaled width and length are gaussian distributed around zero for showers initiated by γ-rays. Since hadronic showers are more irregular and not as compact, this will lead to more extended images of greater width and length.

However, not all background events can be removed by imposing cuts on the image shape. An efficient way to reject the isotropic cosmic ray background is based on the directional informa-

tion. A cut on the arrival direction corresponding to the angular resolution of the instrument is applied. The angle θ between the source position and the reconstructed shower direction is required to fulfill $\theta^2 < 0.008$ deg^2. This cut on the arrival direction defines the so called ON region (see Figure 3.11), and by only selecting events from this region the isotropic cosmic ray background can be reduced.

Only γ-ray like cosmic ray events survive the cuts. The remaining background is estimated by means of the reflected-region background model (for a detailed description see Berge et al., 2007 [42] and Figure 3.11). In the reflected-region model the remaining background in the ON region (fulfilling the θ^2-cut) is calculated assuming that it is equally distributed in the field of view. This isotropic background can be simultaneously measured with the observation of the source [66]. A robust way to estimate this background is wobble mode observations. In this mode the source position in the field of view is offset by $0.5°$ from the camera center. By constructing regions of equal size and with an identical offset to the camera center, it is possible to subtract the background events in the OFF regions from the events from the source in the ON region independently of the radial acceptance (see Figure 3.11). This is because the camera acceptance in general is assumed to be radially symmetric.
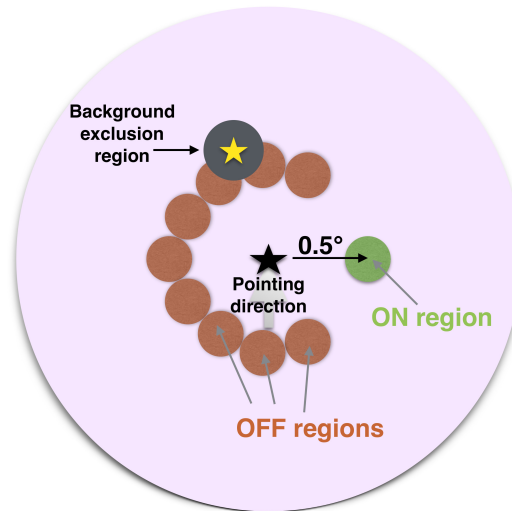
Figure 3.11: Schematic illustration of the reflected-region model for background estimation. The source position in the field of view is offset by $0.5°$ from the camera center. OFF regions of equal size and with an identical offset to the camera center as the ON region can be constructed. This allows simultaneous subtraction of the background independent of the radial camera acceptance.

The background events in all OFF regions (N_{OFF}) are added up and scaled (with a factor α) by the number of regions to normalize the OFF area to the ON area.. The number of excess events ($N_{\text{signal}} = N_{\text{ON}} - \alpha N_{\text{OFF}}$) is the difference between the number of events in the ON region (N_{ON}) and $\alpha \times N_{\text{OFF}}$.

The detection significance S is then calculated according to Equation 17 in Li & Ma (1983) [104],

$$S = \sqrt{2} \left\{ N_{\text{ON}} \times \ln \left[\frac{1+\alpha}{\alpha} \left(\frac{N_{\text{ON}}}{N_{\text{ON}} + N_{\text{OFF}}} \right) \right] + N_{\text{OFF}} \times \ln \left[(1+\alpha) \left(\frac{N_{\text{OFF}}}{N_{\text{ON}} + N_{\text{OFF}}} \right) \right] \right\}^{1/2} .$$

3.2.4 Spectral reconstruction

Effective collection area

The effective collection area is a measure of the probability to detect γ-rays with a given instrument. Hence, this detector efficiency is an important quantity for the calculation of the arriving flux of γ-rays. The effective collection area can be computed based on simulations of the air showers of γ-rays. The whole detector response, electronics chain, and data analysis procedure is realized in these MC simulations, as described in Section 3.2.3.
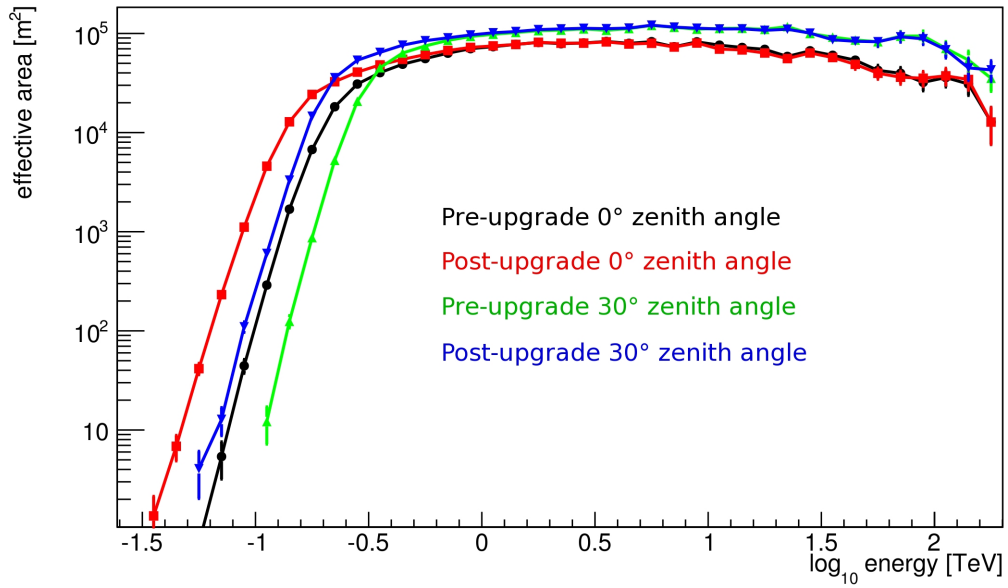
Figure 3.12: Effective areas from before and after the camera upgrade, for $0°$ and $30°$ zenith angles.

The effective area can be written as,

$$A_{\text{eff}} = \left(\pi R^2 \right) \frac{N_{\text{selected}}(E)}{N_{\text{simulated}}(E)}. \tag{3.9}$$

Here πR^2 is the surface in the shower plane, over which the impact points of the γ-rays are evenly distributed. $N_{\text{simulated}}(E)$ denotes the total number of simulated showers in this area. $N_{\text{selected}}(E)$ is the number of events, which trigger the telescope and pass the selection cuts, and hence are finally detected as γ-ray events. This effective area is a function of many

observing parameters, such as the zenith angle and the azimuth angle, the pointing offset from the source position, the applied cuts and the NSB noise level. Effective areas for typical values of these parameters are displayed in Figure 3.12.

Flux calculation

The effective collection area is needed to calculate the flux produced by a specific source. The integral flux ϕ is the number of events N integrated above the threshold energy E_{min} divided by the (dead time corrected) time interval T and the averaged effective area $\langle A \rangle$:

$$\phi(E > E_{\text{min}}) = \frac{N}{T \times \langle A \rangle}. \tag{3.10}$$

The averaged effective area is calculated from the effective area $A_{\text{eff}}(E)$ as a function of energy,

$$\langle A \rangle = \frac{\int_{E_{\text{min}}}^{\infty} A_{\text{eff}}(E) \times \phi_0 \left(\frac{E}{E_0}\right)^{-\Gamma} dE}{\int_{E_{\text{min}}}^{\infty} \phi_0 \left(\frac{E}{E_0}\right)^{-\Gamma} dE}, \tag{3.11}$$

assuming a specific spectral shape,

$$\phi(E) = \phi_0 \left(\frac{E}{E_0}\right)^{-\Gamma}. \tag{3.12}$$

To calculate a differential spectrum of the γ-ray source the same procedure is applied in each energy bin of the spectrum. The value of the spectral index Γ must be assumed in order to calculate the differential flux of the source in each energy bin. This assumption for the spectral index is then checked against the index of the reconstructed spectrum. If the two do not coincide, the reconstruction of the spectrum is iterated with the resulting spectral indices, until the input value and the reconstructed value match.

Energy resolution

Due to fluctuations in the particle air shower, the reconstructed energy E_{rec} as a function of the true energy E_{true} follows a statistical distribution. The energy bias E_{bias} is defined as the expectation value of the relative deviation of the reconstructed energy E_{rec} from the true energy E_{true}:

$$E_{\text{bias}} = \langle \frac{E_{\text{rec}} - E_{\text{true}}}{E_{\text{true}}} \rangle. \tag{3.13}$$

The energy bias E_{bias} is non-negligible at low energies ($\lesssim 200$ GeV) due to threshold effects. γ-ray primaries with an energy E_{true} below the threshold can only be detected if the air shower is an upward fluctuation with a shape corresponding to a reconstructed energy E_{rec} above the threshold. Therefore, a positive energy bias $E_{\text{bias}} > 0$ is present at and below the threshold energy. The energy resolution ΔE is defined as the standard deviation (RMS) of this distribution (see Equation 3.13). The energy resolution for typical parameters of observations is displayed

in Figure 3.13.
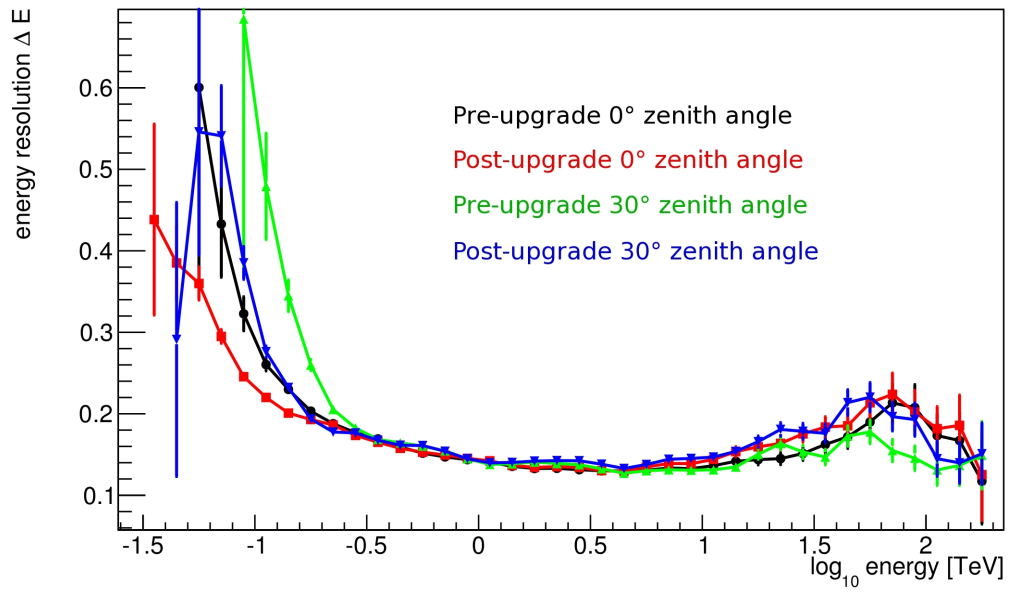
Figure 3.13: Energy resolution from before and after the camera upgrade, for $0°$ and $30°$ zenith angles.

Chapter 4

Observing spectral cut-offs

An essential part of the available information from γ-ray sources is contained in the energy spectrum. It is known that the spectra of most VHE sources follow a power-law over a wide energy range, but in some cases a deviation from a power-law is observed. One possible case is a spectral feature due to pair creation on the EBL (See Section 2.1.3 and e.g. Abramowski et al., 2013 [2] and Abdo et al., 2010 [1]). Other spectral features observed at very-high-energies contain information about the acceleration mechanism in the source (see Section 2.3).

Electrons are a common, relevant particle population contained in γ-ray sources. An **exponential cut-off** in the energy spectrum of Markarian 421 (Mrk 421) can be explained by a maximal energy in the energy distribution of these electrons, which leads to a sharp exponential cut-off in the synchroton radiation spectrum (see Section 2.3.2). A cut-off in the synchroton peak then leads to a similar exponential cut-off in the Inverse Compton peak, as it is an upscattered version of the synchroton peak. Therefore, if the high energy cut-off of the Inverse Compton component can be measured, an important insight into the physical processes at work is gained.

As has been shown by Massaro et al. (2005) [114] and Tramacere et al. (2011) [141], a **log-parabolic** energy spectrum can be explained by an energy dependent stochastic scattering process. In this case the acceleration probability decreases with higher energies, leading to a lower flux and hence a curvature in the VHE spectrum (see Section 2.3.3).

In order to measure spectral cut-offs at very-high-energies it is crucial to understand the uncertainties in the energy reconstruction. This includes the bias, the difference between reconstructed and true energy, as well as the energy resolution (see Section 3.2.4).

Statistical fluctuations of the particle air shower (initiated by a γ-ray primary of true energy E_{true}) in the atmoshphere and the detector response lead to a distribution of reconstructed energies E_{rec} for an ensemble of events. This limited energy resolution and a possible energy bias have to be taken into account in order to be sensitive to spectral features. VERITAS has an energy resolution of $\sim$15-20%, limiting the capacity to resolve spectral cut-offs at TeV energies.

In this chapter, the effect of the limited energy resolution on the measurement of spectral cut-offs at TeV energies is investigated. The capacity to measure such a spectrum, deviating from

a power-law, is then quantified for different energy resolutions ranging from the VERITAS to CTA values. This is done by means of a toy Monte-Carlo simulation using a Forward Folding algorithm. This Forward Folding is finally tested on data to reconstruct the spectrum.

4.1   Unfolding the energy spectrum

The detection of very-high-energy γ-rays is limited by statistical fluctuations. A shower caused by a γ-ray with true energy E_{true} can be reconstructed with a different energy $E_{\text{rec}} \neq E_{\text{true}}$ due to the quantum mechanical probabilistic nature of the particle cascade. The fluctuating number of particles of the shower leads to uncertainties in the energy estimation. This section describes a method to take into account these statistical detection effects. *'Unfolding'*, the inverse process to the convolution of the measurement with the instrument's response, is introduced.

Simulating the shower and detector response in a Monte-Carlo experiment, the instrument response function can be approximated statistically. The distribution of γ-rays with true energy E_{true} measured to have the reconstructed energy E_{rec} can be obtained and the result can be represented as a binned 2D histogram. This 2D histogram is also called an energy migration matrix. The normalized number of events in each bin is the probability for a true energy E_{true} to be reconstructed with E_{rec}. The width of the distribution for a given E_{true} is a measure of the finite energy resolution of the detector. An offset between the mean value of E_{rec} from the mean of E_{true} is characteristic of a bias.

By means of the unfolding principles from Blobel (1984) [50] and Blobel (2002) [51], the energy spectrum as a function of true energy E_{true} can be obtained. The uncertainty in the energy estimation can be described by the probability $M(y, x)$ to measure the value y, given that the true value is x. The statistical distribution of measurements, the number of events per energy $g(y)$, is given by,

$$g(y) = \int_a^b M(y, x) f(x) dx + \epsilon(y) \tag{4.1}$$

where f is the true distribution and ϵ accounts for statistical errors. In a counting experiment, it is possible to introduce discrete variables with a finite number of energy bins (m) in the true distribution f:

$$g_i = \sum_{j=1}^m M_{ij} f_j + \epsilon_i. \tag{4.2}$$

Here M_{ij} is the migration matrix. It is normalized in order to preserve the number of events $\sum_i M_{ij} = 1$.

Correction factor method

Taking into account the detector's acceptance only, the *correction factor* method can be used. In a Monte-Carlo simulation a number $\bar{f}_j$ of true events in each energy bin j is simulated. The simulation leads to a number $\bar{g}_j$ of detected events per energy bin j, resulting in an acceptance

$\frac{\bar{f}_j}{\bar{g}_j}$. This is the correction factor. Here the possibility of limited energy resolution, represented by non-zero off-diagonal elements ($M_{ij} \neq 0$ for $i \neq j$) in the migration matrix is ignored as a first approximation. It is taken into account only as far as a migration of events leads to a fixed correction factor in each energy bin. From the correction factor, obtained by simulations, one can calculate the true number of events f_j in the energy bin j, from the number of measured events g_j:

$$f_j = g_j \left(\frac{\bar{f}_j}{\bar{g}_j} \right). \tag{4.3}$$

One disadvantage of the correction factor method is that it is biased towards the model which has to be assumed in the Monte-Carlo simulation already [55]. In general, this model will be a power-law, neglecting spectral cut-offs.

Inversion and Regularization

One way of directly taking into account the whole response matrix M_{ij} is by inversion. The inverse M_{ij}^{-1} of the migration matrix can be obtained for example by Gauss-Jordan elimination or Newton's method. By applying the inverse of the response matrix M^{-1} to the measured distribution g, the true distribution f then simply is:

$$f = M^{-1}g. \tag{4.4}$$

However this yields the following covariance matrix $V(f)$ of f,

$$V(f) = M^{-1}V(g)M^{-1}. \tag{4.5}$$

In general, after inversion, M^{-1} will have a significant amount of non-zero off-diagonal elements, due to non-zero off-diagonal elements in M ($M_{ij} \neq 0$ also for $i \neq j$). This means that after matrix multiplication, $V(f)$ has significant non-zero off-diagonal contributions, and so the resulting true values f are expected to be highly correlated.
The statistical uncertainty in the measurement g, therefore, leads to strongly amplified oscillations in the resulting true distribution f. Error propagation from g to f amplifies the statistical uncertainties by the inversion of the response matrix M_{ij}.
One way of handling these fluctuations is to impose additional conditions on f. Assuming that it is a smooth function, the derivatives are expected to be small. This can be taken into account.
Direct inversion is computationally similar to solving the least squares χ_0^2 expression for the difference between the measured distribution g and the unknown M applied to the true distribution f:

$$\chi_0^2 = (g - Mf)^T V^{-1}(g)(g - Mf). \tag{4.6}$$

Hence it is possible to introduce an additional "Regularization" term Reg(f) (with a weight factor ω) in the least squares expression:

$$\chi^2 = \frac{\omega}{2} \times \chi_0^2 + Reg(f). \tag{4.7}$$

This regularization suppresses fluctuations in the solution f. In Tikhonov's method [139], for instance, the regularization term is given by the second derivative of the true distribution f:

$$Reg(f) = \left(\frac{d^2 f}{dx^2}\right)^2. \tag{4.8}$$

As a result of the minimization the regularized solution f has minimal curvature.

Forward Folding

Regularization holds for the condition that f is a smooth function without oscillations. An even stronger requirement is to model f with a parameterized function. The χ_0^2 minimization will then yield the best fitting parameters of the model. This unfolding scheme is called *Forward Folding*.

Since TeV γ-ray spectra generally follow a power-law over a wide energy range, it is possible to model the energy spectrum by such a power-law. In case of additional spectral features, further parameters, such as an exponential cut-off at very-high-energies, can be introduced. The resulting χ^2 is a measure of how well the model fits the data.

Forward Folding has been applied before to γ-ray astronomy (see for example [25]).

4.2   Capacity of detecting spectral features

The VERITAS performance shows an energy resolution of 15-20% and the CTA is aiming for 5% [37]. The ability to measure spectral features with these instruments using a Forward Folding scheme is investigated in this section. The influence of the energy resolution on the sensitivity to detect a spectrum deviating from a power-law is studied.

4.2.1   Scheme of the toy Monte-Carlo

A toy MC experiment is set up to simulate different energy spectra. A true energy spectrum deviating from a power-law is folded with the instrument's response. The instrument response function is composed of the effective collection area A_{eff} (the detector's acceptance) and the energy migration matrix $M_{ij} = p(E_{\text{true}}^i \rightarrow E_{\text{rec}}^j)$ (the probability p for a γ-ray with true energy E_{true} to be measured with energy E_{rec}). This yields the expected number of measured events λ in each bin of the reconstructed energy E_{rec}. The integer number n of measured events in E_{rec} is then drawn from a Poisson distribution with mean λ. The probability $P(n)$ to draw the

integer number n is given by,

$$P(n) = \frac{\lambda^k e^{-\lambda}}{k!},$$ (4.9)

where n is the simulated number of measured events in each energy bin of E_{rec}. The ensemble of $n(E_{\mathrm{rec}})$ yields the histogram g to which the Forward Folding is applied. A log-binning of $\log(\Delta E) = 0.05$ is applied to this histogram g in order for each bin to contain a significant number of events. The relatively fine binning has the advantage to better resolve the energy scale of spectral features.

Once the histogram in reconstructed energy has been obtained from the (in this case) known spectrum in true energy, Forward Folding is applied. The true energy spectrum can then be compared to the output from the Forward Folding, and ideally, they should match. In this way, the performance of the Forward Folding can be investigated.

The Forward Folding algorithm is implemented by a log-likelihood fit of a given spectral model. The spectrum in true energy folded with the instrument's response is fit to the histogram of reconstructed events in E_{rec}. The fit-function is a convolution of the parameterized spectrum with the energy migration matrix and effective collection area.

The spectrum, as a function of true energy, is a power-law with exponential cut-off. It is fit with a power-law and a power-law with exponential cut-off. For each model a maximal log-likelihood is extracted. Using this likelihood, a likelihood-ratio test is performed to show which model is favored. The scheme of the toy MC is illustrated in Figure 4.1.
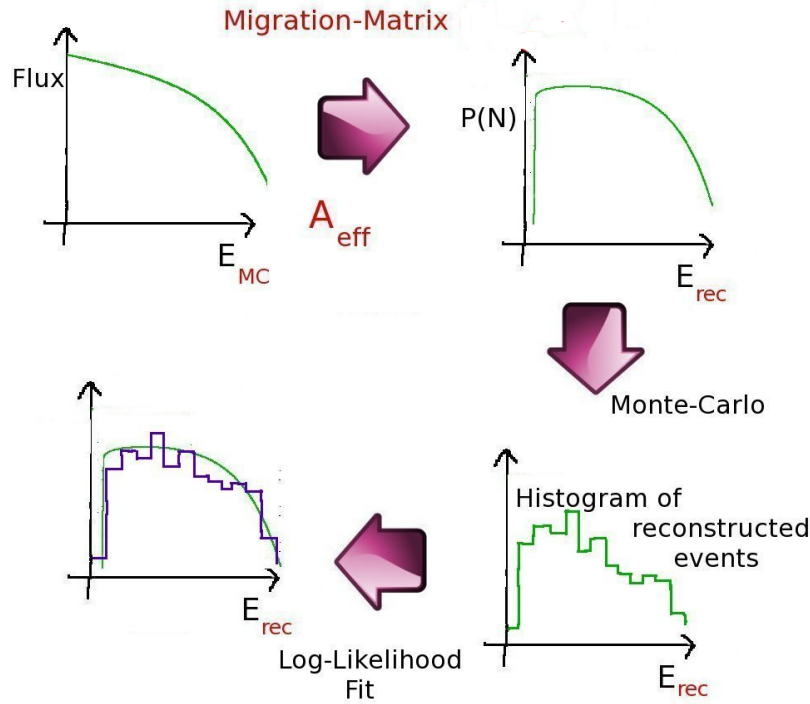
Figure 4.1: Toy MC scheme: the intrinsic spectrum (flux as a function of true energy E_{true}) is folded with the effective collection area A_{eff} and the energy migration matrix. This yields an expected number of measured events λ as a function of reconstructed energy E_{rec}. In each energy bin a poissonian random experiment with mean λ is performed yielding an integer event number n in each energy bin. Assuming a given spectral shape, the resulting histogram is fit with a convolution of the instrument's response function with this spectral shape. Resulting from this Forward Folding are the spectral parameters, as well as a log-likelihood.

Figure 4.2 shows the histogram of reconstructed events g for an observation time of 100 hours. In this toy MC 62 bins ranging from 35 GeV to 45 TeV are filled with Poissonian random numbers. The simulated intrinsic spectrum is a power-law with an additional exponential cut-off (Equation 2.10). Parameters from a typical spectrum of the blazar Mrk 421 (Section 4.3.2) as observed in a low state in 2011 are taken. The flux normalization is $\phi_0 = 1.4 \times 10^{-7}$ m^{-2} s^{-1} with a spectral index $\Gamma = 2.7$. Due to the energy threshold of the instrument ($\sim$ 100 GeV), the unfolding is done on the energy range from 90 GeV to 45 TeV. In the red model, Forward Folding is applied with a power-law (Equation 2.14). In blue, the spectrum is unfolded with a power-law with an exponential cut-off (Equation 2.10), while it is unfolded with a log-parabolic spectrum (Equation 2.11) in the green model. All models are plotted together with the reconstructed histogram.
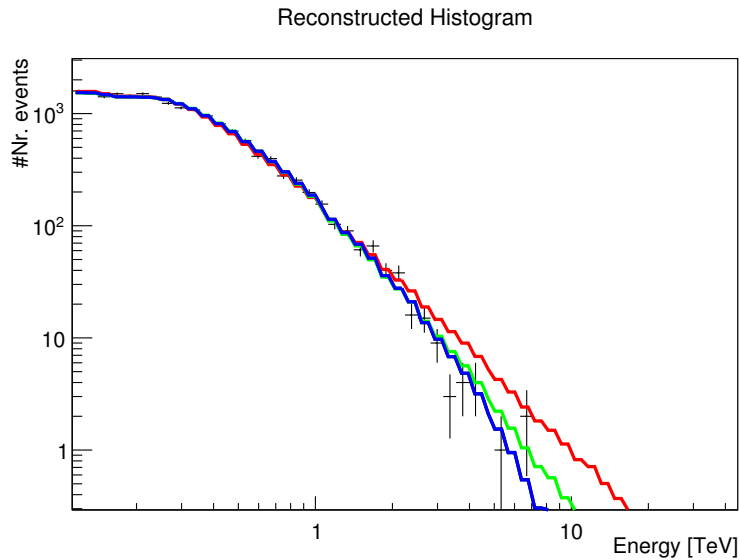
Figure 4.2: Histogram of events per energy bin for a simulation of a power-law with exponential cut-off. Fit with a powerlaw (red), cut-off (blue), log-parabola (green).

From the log-likelihood-fit, the normalization ϕ_0, the cut-off energy E_C, and the spectral indices Γ, a and b are extracted.

4.2.2 Likelihood-ratio test on the spectral shape

It is possible to compare a null model,

- H_0 = null hypothesis,

which is a special case of the alternative model,

- H_1 = alternative hypothesis,

by performing a likelihood-ratio test.

For instance, in the case of a power-law as the null hypothesis (H_0), tested against a power-law with exponential cut-off (H_1), the cut-off energy in the null hypothesis is fixed to $E_C \rightarrow \infty$. (E.g. see [96]). This means that the parameter space Θ_0 of the null model H_0 is the complement to the parameter space Θ_1 of the alternative model H_1.

The likelihood-ratio Λ then is defined as:

$$\Lambda(x) = \frac{\sup_{\theta \epsilon \Theta_0} f^{X_1, \cdots}(x_1, ..., x_n; \theta)}{\sup_{\theta \epsilon \Theta_1} f^{X_1, \cdots}(x_1, ..., x_n; \theta)}, \tag{4.10}$$

where the probability density functions f are maximized, in order to have a supremum at the resulting parameter values θ for the given data $x_1, ..., x_n$. Λ is equal to the logarithm of the quotient of the likelihoods for the resulting maximal values.

Assuming the difference of the log-likelihoods to be χ^2-distributed,

$$-2 \log \Lambda(X) \rightarrow \chi^2, \tag{4.11}$$

it is possible to calculate the probability that the alternative hypothesis H_1 is favored over
the null hypothesis. The significance of this assumption can be quantified by the p-value, the
probability that the null hypothesis is true but rejected.

The p-value is defined as the integrated probability density, in χ^2-statistics, integrated from
the resulting test statistics value x to infinity:

$$p(x) = \int_x^\infty \chi^2(y) dy \qquad (4.12)$$

The significance level of the p-value corresponds to a particular multiple of standard devia-
tions σ by which H_1 is favored over H_0.

In the case of Forward Folding, a certain model spectrum is assumed. By means of the sig-
nificance level obtained from the likelihood-ratio test, one can determine if a more complex
model, such as the log-parabolic spectrum or a power-law with exponential cut-off, is favored
over the null hypothesis over the whole energy range.

4.2.3   Simulating an exponential very-high-energy cut-off

In this section, a power-law with an exponential cut-off is simulated. Energy resolutions rang-
ing from VERITAS to the foreseen CTA value are used. The instruments' energy resolution is
simulated by adjusting the width of the migration matrix.
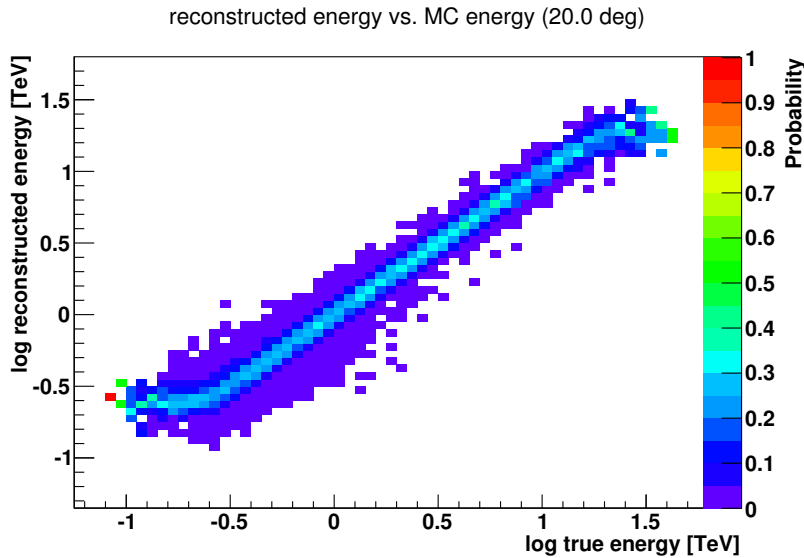
Figure 4.3: The VERITAS energy migration matrix of E_{true} vs. E_{rec} for 20 degrees zenith
angle.

Fitting the energy migration matrix (see Figure 4.3) at a fixed true energy $E_{\text{true}} = 1$ TeV
with a normal distribution as in Figure 4.4 yields a $\chi^2/\text{d.o.f.} \approx 1$. This justifies the assumption
of a gaussian shape of the distribution of each row and column in the energy migration matrix.
The variance σ^2 of this normal distributed histogram is scaled by a factor λ. Adding a bias η

this reads:

$$M(y, x) = \frac{1}{\sigma\sqrt{2\pi}} e^{-\frac{1}{2}\left(\frac{x-y+\eta}{\sigma}\right)^2}. \tag{4.13}$$

$$M(y, x) \rightarrow M(y, x)^{\frac{1}{\lambda}} \Leftrightarrow \sigma^2 \rightarrow \sigma^2 \times \lambda. \tag{4.14}$$
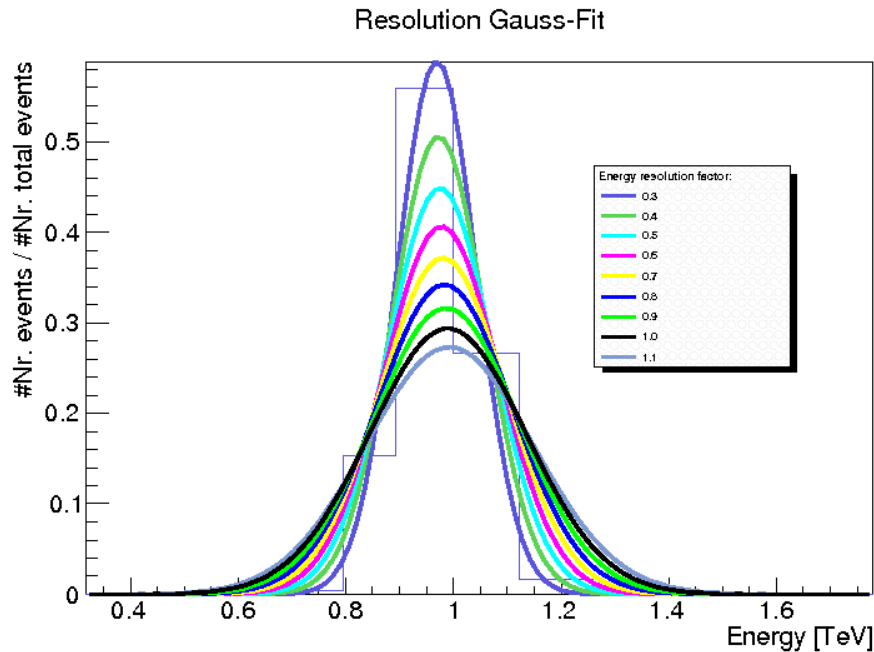
Figure 4.4: Width of the Gaussian migration matrix for the 9 different energy resolutions.

The factor λ is equal to $\lambda = 0.3$ for CTA ($\approx$ 5% energy resolution [37]), and $\lambda = 1.0$ for VERITAS ($\approx$ 15-20% energy resolution), which is comparable also to H.E.S.S. and MAGIC [15] [29]. Figure 4.4 shows the Gaussians of the energy migration matrix for the different energy resolutions, which are simulated. The χ^2/d.o.f. is equal to 0.4 for VERITAS. This is consistent with the assumption of a normal distribution.

Four different observation times are simulated: $t_1 = 10$ h, $t_2 = 20$ h, $t_3 = 40$ h and $t_4 = 80$ h. The flux level is 20% C.U.[1], with a flux normalization $\phi_0 = 1.4 \times 10^{-7}$ m^{-2} s^{-1} and a spectral index $\Gamma = 2.7$. These spectral parameters were taken from Markarian 421 (see Section 4.3.2), a well studied source known to show an exponential cut-off.

The simulated true energy spectrum is a power-law with exponential cut-off. It is unfolded and reconstructed with a power-law, plus a power-law with exponential cut-off. From the likelihood-ratio test a significance by which the power-law with exponential cut-off is favored over a power-law is obtained. This is done for different random seeds, resulting in a histogram of significances by which an exponential cut-off is favored over a power-law. Each entry in this histogram is a different simulation with a different random seed. As expected, the histogram is normally distributed, as shown in Figure 4.5. From the gaussian fit, a mean value and an error on the mean can be extracted.

---

[1]C.U. (Crab Units) refer to the flux of the Crab Nebula

Significance distribution
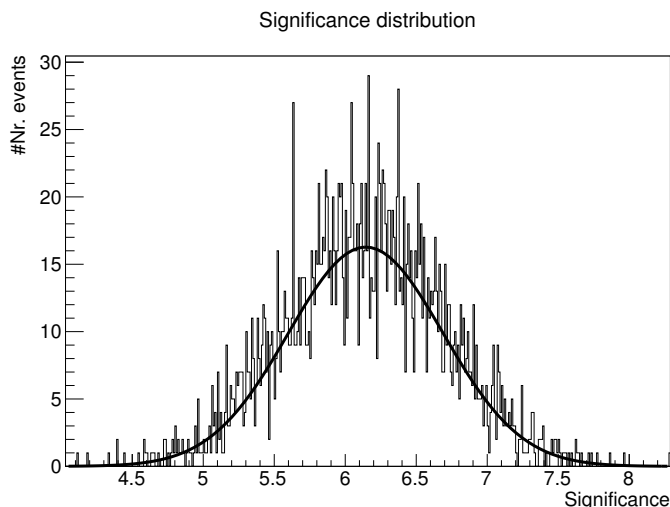
Figure 4.5: Normally distributed significance to detect an exponential cut-off at $E_C = 1.7$ TeV in 100 h for a flux of 20% Crab Units.

4.2.4 Dependence on cut-off energy

The significance to detect an exponential cut-off as a function of the simulated cut-off energy is illustrated in this section. A power-law with exponential cut-off is simulated with cut-off energies chosen to be $E_C^1 = 0.2$ TeV, $E_C^2 = 0.3$ TeV, $E_C^3 = 0.5$ TeV, $E_C^4 = 0.8$ TeV, $E_C^5 = 1.2$ TeV, $E_C^6 = 1.7$ TeV, $E_C^7 = 2.5$ TeV, $E_C^8 = 4$ TeV, $E_C^9 = 6$ TeV and $E_C^{10} = 10$ TeV. The VERITAS energy migration matrix (and energy resolution) and effective collection area are taken into account as the instrument's response function. Figure 4.6 displays the significance as a function of the exponential cut-off energy. The 5σ detection threshold is plotted as a light blue line. A flux of 20% C.U. (Crab Units) is simulated for a total observation time of 80h. The significance is shown as a function of the simulated cut-off energy for 4 different observing times 10 h (red), 20 h (green), 40 h (blue) and 80 h (pink). The significance scales with the square root of the observation time within errors. The significance exhibits a maximum around a simulated cut-off energy of ~ 1 TeV, decreasing with lower and higher cut-off energies. For low cut-off energies, the impact of the exponential cut-off is significant enough to suppress events in the sensitive range. This leads to a lack of statistics in the sensitive energy range, comparable to the effect of smaller observation times, and so the significance decreases. For high cut-off energies, the exponential cut-off does not have a significant effect in the sensitive energy range.
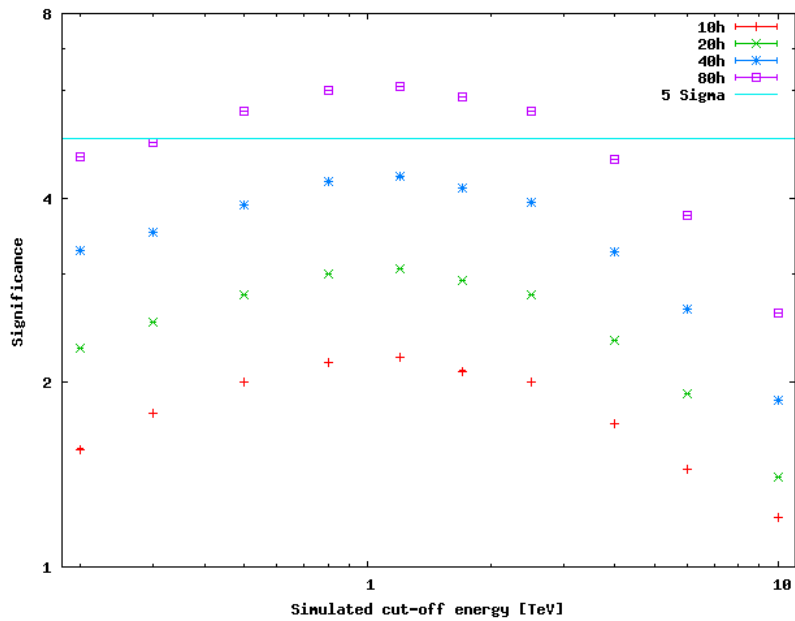
Figure 4.6: Significance (by which an exponential cut-off spectrum is favored over a power-law) as a function of simulated cut-off energy. Simulated observing times: 10 h (red), 20 h (green), 40 h (blue) and 80 h (pink).
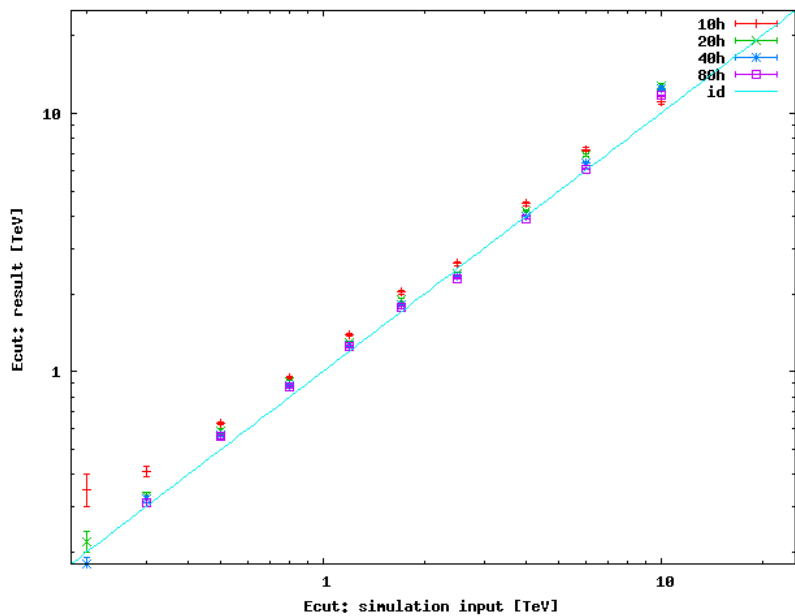
Figure 4.7: Simulated value for E_C [TeV], compared to the reconstructed value extracted from unfolding the spectrum with an exponential cut-off, for four different simulated observing times: 10 h (red), 20 h (green), 40 h (blue), 80 h (pink)

In Figure 4.7 the simulated value for E_C is compared to the parameter value extracted from the Forward Folding. This is done for four different observing times 10 h (red), 20 h (green),

40 h (blue) and 80 h (pink). The values are compatible with the identity (input=output, blue line), showing that this method yields the expected outcome. A systematic effect is evident for shorter observation times of the low cut-off energies, due to a lack of statistics. If the cut-off energy is close to the energy threshold the number of simulated events is limited by the exponential suppression from the cut-off. Furthermore, the cut-off energy is systematically overestimated. This could be due to the loss of information in the convolution process.

The significance scales with the square root of the observation time, as shown in Figure 4.8, where the four significance curves align when divided by $\sqrt{\text{time}}$. The significance divided by the square root of the observation time in hours shows a similar dependence on the cut-off energies for all simulated observation times.
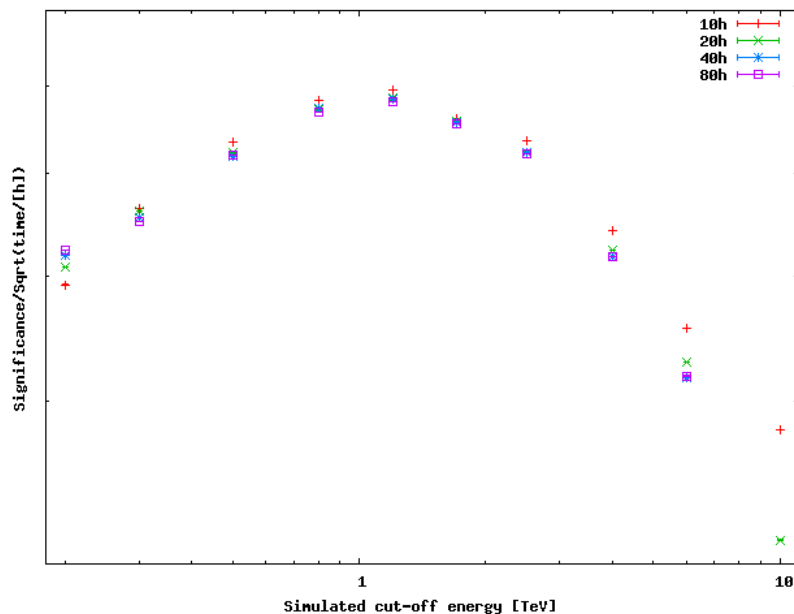
Figure 4.8: Significance $[\sigma] / \sqrt{\text{time[h]}}$ as a function of simulated cut-off energy. Simulated observing times: 10 h (red), 20 h (green), 40 h (blue) and 80 h (pink).

Instead of changing the observation times, it is also possible to look at the significance as a function of the flux level for a fixed observation time of 20 h. Figure 4.9 illustrates that cut-offs between 300 GeV and 3 TeV can be detected in 20 h for sources reaching the flux of the Crab nebula. It is apparent from this work that the maximal detection sensitivity for an exponential cut-off is located at cut-off energies of ≈ 1 TeV.
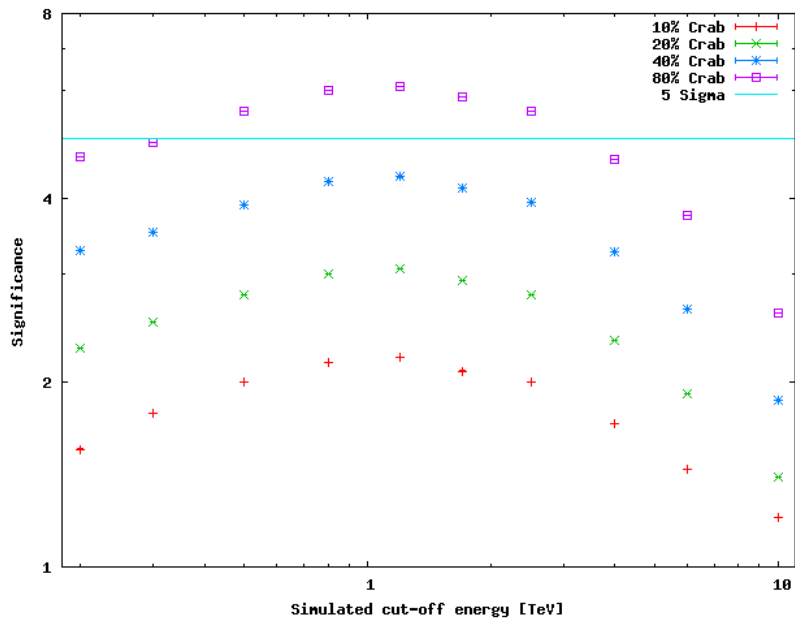
Figure 4.9: Detection significance $[\sigma]$ in 20 h as a function of simulated cut-off energy. Simulated fluxes: 10% C.U. (red), 20% C.U. (green), 40% C.U. (blue) and 80% C.U. (pink).

4.2.5 Detection threshold as a function of time

In this section, the simulated cut-off energy, which previously showed the highest significance, $E_C = 1.2$ TeV, is investigated in more detail. The significance $[\sigma]$ is fit with the square root of the observation time and interpolated to the detection threshold of 5σ (Figure 4.10).
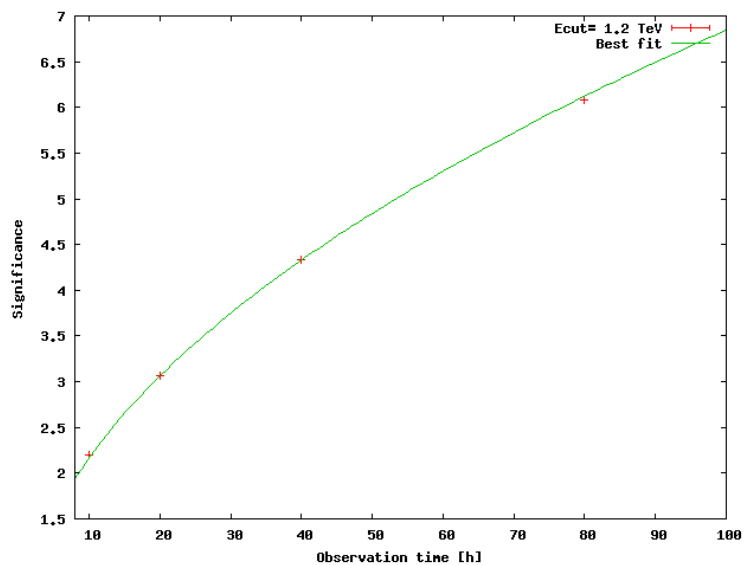
Figure 4.10: Detection significance $[\sigma]$ for $E_C = 1.2$ TeV as a function of observation time. The best fit is shown in green.
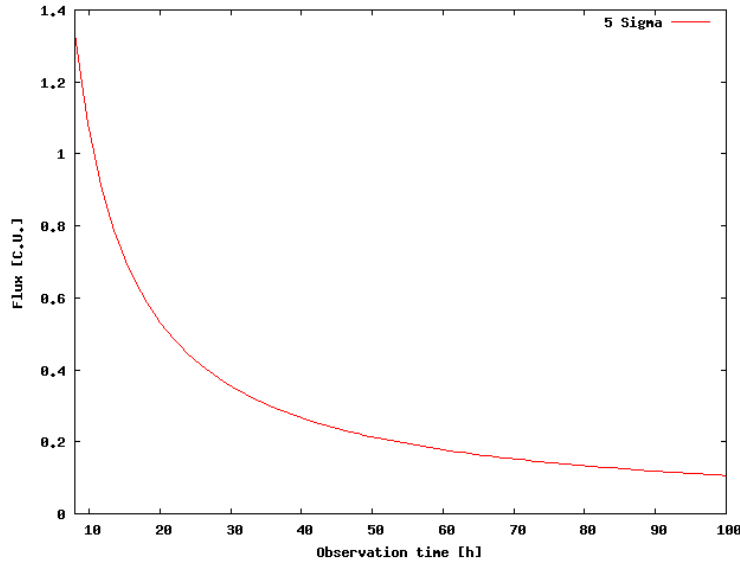
Figure 4.11: Minimum flux level [C.U.] for a 5σ detection of a cut-off energy $E_C = 1.2$ TeV for a given observation time.

The best fit for the significance is given by Significance $[\sigma] = (0.684 \pm 0.002) \times \sqrt{(\text{time/h})}$ resulting in a necessary observation time of 53.4 ± 0.4 h for a 20% C.U. flux. The detection threshold is identical in the parameter space: Flux $\times$ Time = Const. This allows the necessary observation time as a function of a given flux level to be plotted (Figure 4.11).
Accordingly, it is possible to detect an exponential cut-off of a 50% C.U. source in ≈ 20 h, whereas an exponential cut-off a source of twice the strength can be detected in almost 10 h.

4.2.6   Log-parabola spectrum

A spectrum with an exponential cut-off has been simulated, and the capacity to detect such a spectral feature has been quantified. The second spectral shape describing a curvature, which will be investigated in this section, is a log-parabolic spectrum (Equation 2.11).
Again, the ability to detect such a spectral feature with a VERITAS-like instrument response function is quantified in terms of a significance. Hence, the power-law with exponential cut-off is unfolded not only with a cut-off model but also with a log-parabolic shape. Secondly, also a log-parabola spectrum is simulated and unfolded with both an exponential cut-off and a log-parabola shape. The significance by which both models are favored over a power-law is calculated in each of these cases.
First, a power-law with an exponential cut-off for 80h observation time and 20% C.U. flux level is simulated. The spectrum is reconstructed with a power-law with exponential cut-off and a log-parabolic spectrum. The detection significance for such a spectral feature compared to a power-law is illustrated in Figure 4.12 in green together with the 5σ detection threshold in blue. The detection significance of an exponential cut-off (from Figure 4.6) is also shown in red for comparison. The true log-parabola model is favored over a power-law more significantly than the exponential cut-off is preferred over a power-law, as expected.
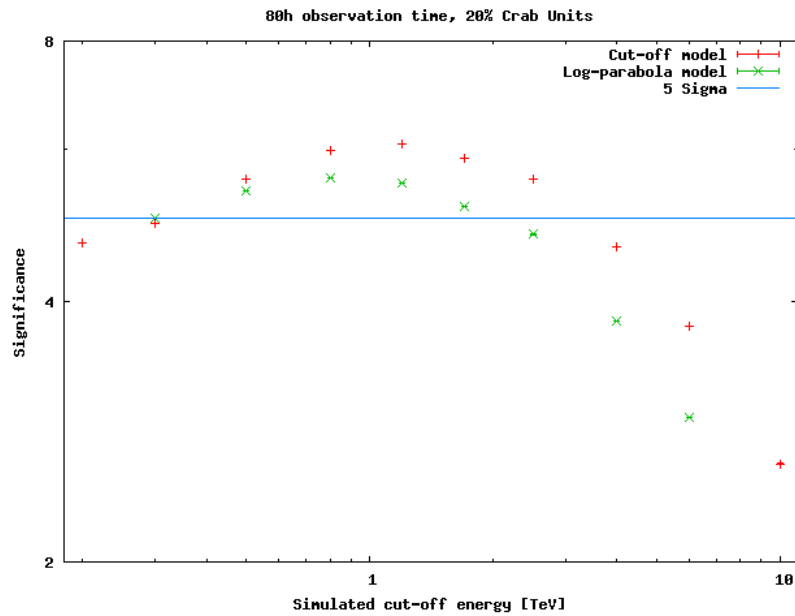
Figure 4.12: Comparison of the detection significance of a Cut-off (red) and Log-parabola Forward Folding model (green) favored over a power-law. Simulations were performed with exponential cut-off energies from 200 GeV to 10 TeV.
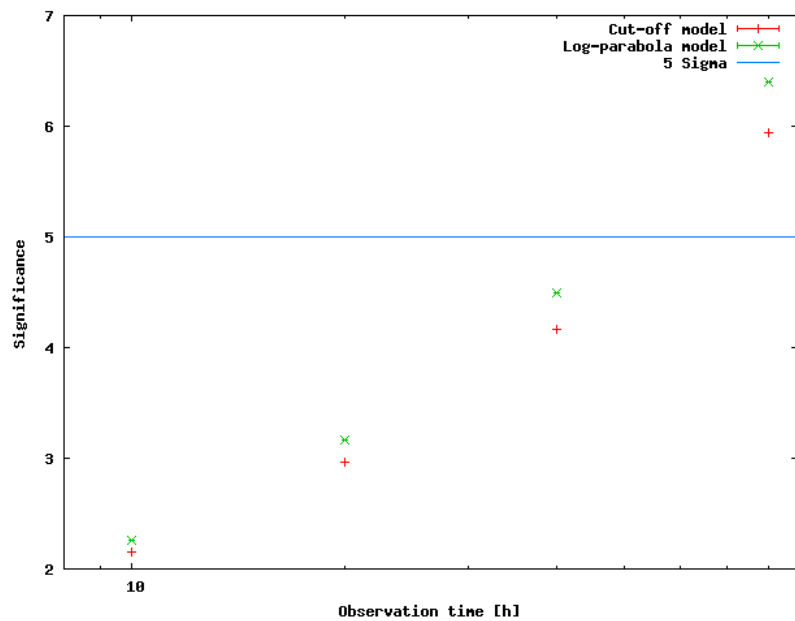
Figure 4.13: Comparison of Cut-off (red) and Log-parabola (green) Forward Folding model for a Log-parabolic spectrum. The significance is plotted as a function of observing time (10 h, 20 h, 40 h and 80 h).

Finally, a log-parabolic spectrum is also simulated. The normalisation used is $\phi_0 = 1.4 \times 10^{-7}$ m^{-2} s^{-1} as in the case of an exponential cut-off. The indices are $a = 2.5$ and

$b = 0.13$ as observed for Mrk 421 (Section 4.3.2) in 2011.

The results for the detection significance are plotted in Figure 4.13. The significance for the simulated log-parabola spectrum is continously higher for all observation times $t_1 = 10$ h, $t_2 = 20$ h, $t_3 = 40$ h and $t_4 = 80$ h than the significance to detect an exponential cut-off. For an 80 h observation duration, the detection threshold of 5σ is reached. However, although the significance for a log-parabola spectrum is higher, it is difficult to distinguish between these two spectral shapes. The likelihood-ratio test does not allow for discrimination between these two completely different models with the same number of parameters.

4.2.7   Influence of the energy resolution

The significance as a function of the cut-off energy has been shown. For a cut-off energy $E_C = 1.2$ TeV the necessary observation time for a 5σ detection has been illustrated. These results hold for the typical energy resolution of VERITAS.
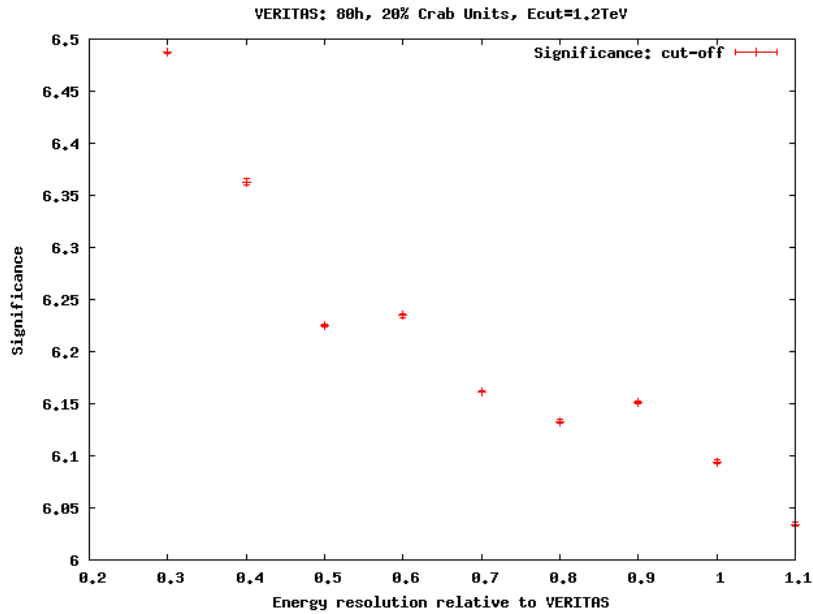
Figure 4.14: Significance as a function of energy resolution factor λ (Equation 4.14): simulation of a power-law with exponential cut-off, Forward Folding: significance of an exponential cut-off spectrum favored over a power-law. VERITAS: $\lambda = 1$. CTA: $\lambda = 0.3$.

One objective of the toy Monte-Carlo study however was to quantify the effect of the limited energy resolution. In this section therefore, the energy resolution is modified ranging from the typical VERITAS value to the expected performance of CTA. An exponential cut-off spectrum is simulated with the cut-off energy fixed at the value $E_C = 1.2$ TeV in order to quantify the effect of a limited energy resolution. The source strength is set to 20% C.U., and the observation time is 80 h. In Figure 4.14, the increase of the detection significance as

a function of an improved energy resolution is displayed. The spectrum is unfolded with an exponential cut-off. From the VERITAS factor (Equation 4.14) $\lambda = 1.0$ to the CTA factor $\lambda = 0.3$, the detection significance of an exponential cut-off rises from $\sim 6\sigma$ to $\sim 6.5\sigma$.

4.2.8 Prospects for CTA

So far an energy resolution with values typical of VERITAS and expected for CTA has been chosen. However this energy resolution has been simulated for a VERITAS sensitivity only. In this section, the detection of an exponential cut-off with CTA sensitivity is studied. A flux of 20% C.U. is simulated for an observation time of 8 h for energy resolutions from VERITAS (factor $\lambda = 1.0$) to the CTA value (factor $\lambda = 0.3$). The detection significance for an exponential cut-off is illustrated in Figure 4.15.
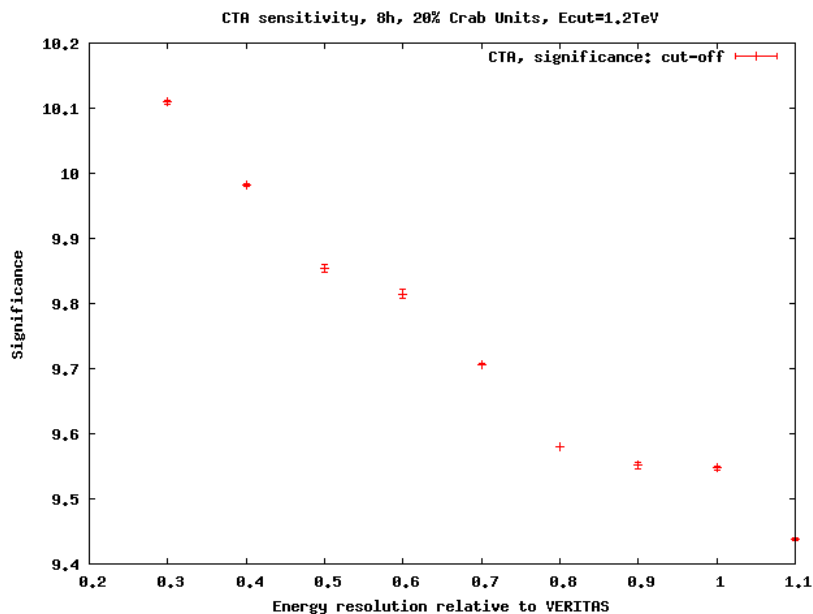
Figure 4.15: Significance of an exponential cut-off favored over a power-law as a function of energy resolution for a power-law with exponential cut-off simulated with CTA sensitivity. Resolution factor λ (Equation 4.14), VERITAS: $\lambda = 1$, CTA: $\lambda = 0.3$.

The dependence on the energy resolution is comparable to the dependence from Forward Folding with VERITAS sensitivity. An increase of the order of 10% from $\lambda = 1$ to $\lambda = 0.3$ is observed.

It is clearly shown that the improved sensitivity leads to a better capacity to detect a very-high-energy cut-off. Looking at the significance as a function of the simulated cut-off energy E_C (Figure 4.16) one can see that the whole range of exponential cut-off from 200 GeV to 10 TeV can be detected in less than 8h. The maximal significance occurs at 1.7 TeV compared to 1.2 TeV with VERITAS-like sensitivity. For this study, a CTA-like energy resolution is assumed.
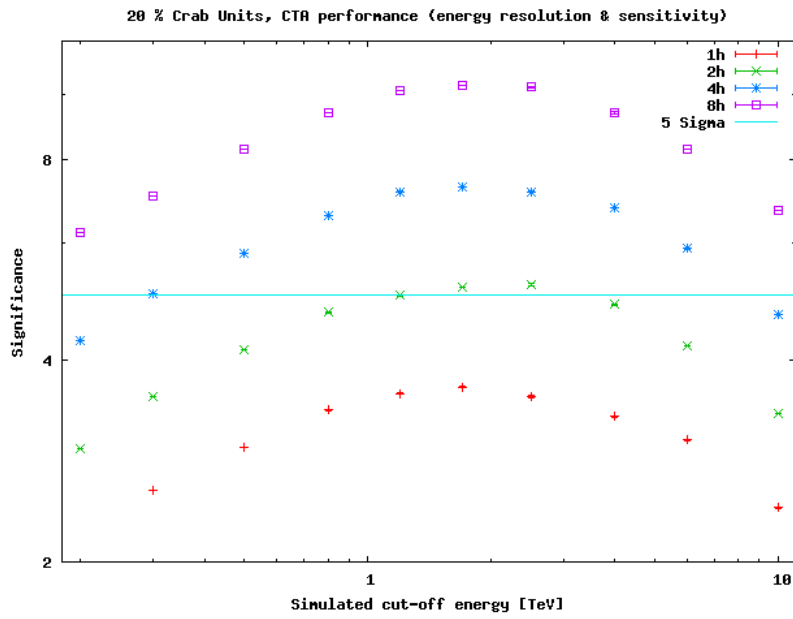
Figure 4.16: Significance as a function of the simulated cut-off energy E_C for observations of 1 h (red), 2 h (green), 4 h (blue) and 8 h (pink). 5σ displayed as light blue line.
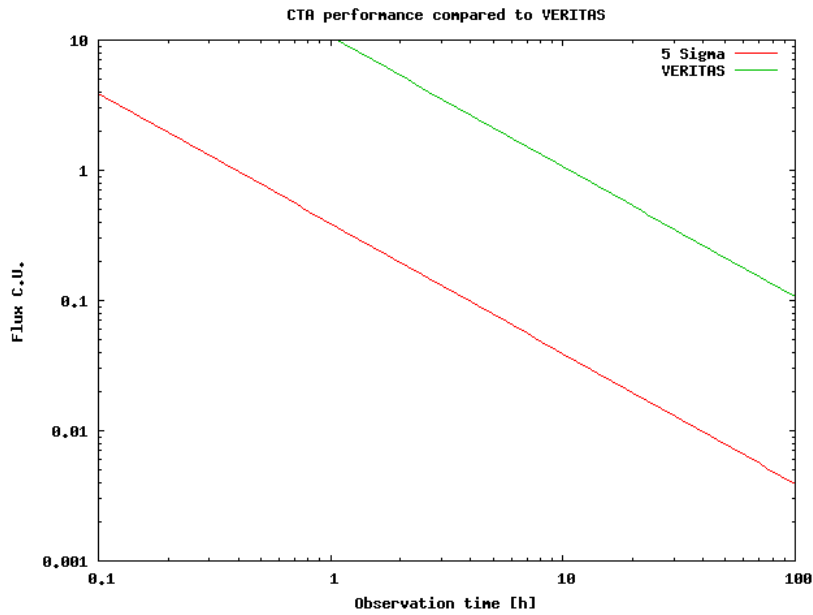
Figure 4.17: Observation time [h] for a 5σ detection of an exponential cut-off for a given flux level in C.U. (for a cut-off energy $E_C = 1.2$ TeV). CTA performance (red) compared to VERITAS (green).

As for VERITAS, the significance scales with the square root of the observation time. Accordingly, it is possible to interpolate the necessary observation time (1.96 ± 0.09 h) for a 5σ detection for a fixed cut-off energy $E_C = 1.2$ TeV (as in the case of VERITAS-like

performance) at the flux level 20% C.U.

The observation time necessary for a 5σ detection can be extrapolated to different flux levels. The resulting flux level in C.U. as a function of time [h] is illustrated in Figure 4.17. An exponential high energy cut-off of a 1% C.U. source for example could be detected in 30 h with the CTA.

In Figure 4.18, the calculation is done for all simulated cut-off energies E_C. The necessary observation time for a 5σ detection of an exponential cut-off is displayed as function of the flux level in Crab Units and the simulated cut-off energy E_C.
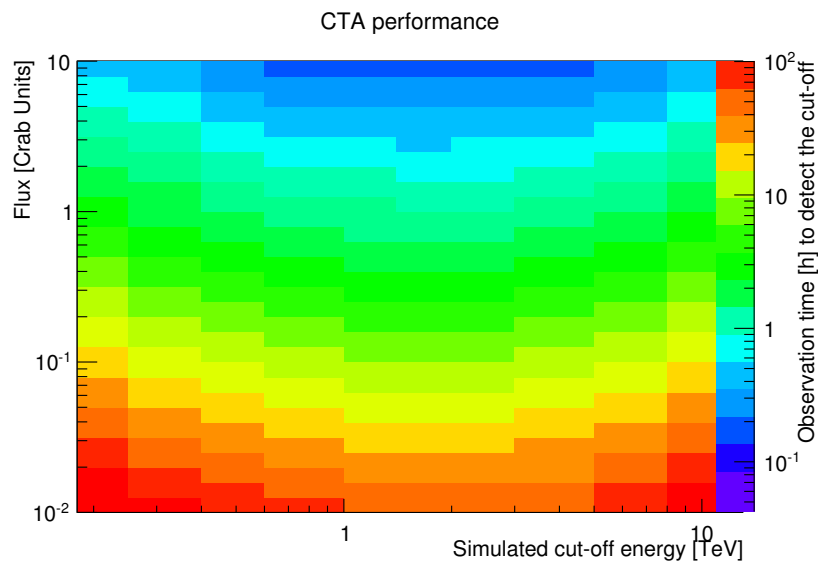
Figure 4.18: Observation time [h] for a 5σ detection as a function of cut-off energy E_C and flux level in Crab Units for CTA sensitivity and energy resolution.

4.2.9 Conclusions

In conclusion, Forward Folding is a powerful method to take into account the effect of a limited energy resolution. By unfolding the energy spectrum it is possible to reconstruct spectral features, such as an exponential cut-off at high energies, to great accuracy.

In Figure 4.19 the observation time necessary for a 5σ detection of an exponential cut-off with VERITAS sensitivity is displayed as function of the flux level in Crab Units for all simulated cut-off energies. The VERITAS energy resolution of $\sim 15\%$ is taken into account by unfolding the energy migration matrix.
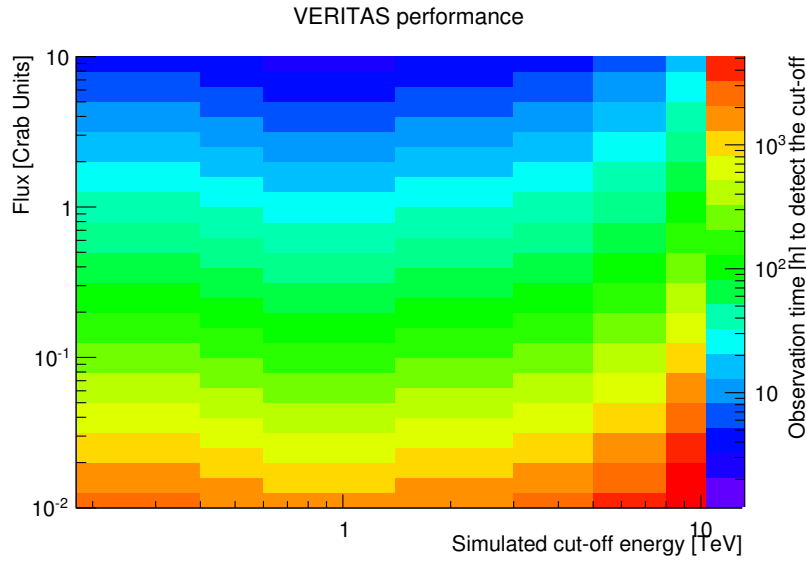
Figure 4.19: Observation time [h] for a 5σ detection as a function of cut-off energy E_C and flux level in Crab Units for VERITAS sensitivity and energy resolution.

The significance increases from high and low cut-off energies towards a maximum at a cut-off energy E_C of about 1 TeV. For a CTA-like performance, it is expected that an exponential cut-off can be detected on a timescale ~ 27 times shorter than the timescale required for a VERITAS-like performance. The sensitivity increase for CTA compared to VERITAS amounts to a factor of ~ 10.

4.3   Comparison to the correction factor method

The previous section illustrates that VERITAS is expected to be able to detect a spectral cut-off at very-high-energies for bright sources, if present. This can be achieved by Forward Folding. In this section, Forward Folding is tested on two of the brightest sources in the TeV γ-ray sky, the Crab Nebula [147] and Markarian 421 [124]. It is shown that this analysis method produces results which are consistent with the standard correction factor method. Three models are used, i.e. a power-law (Equation 2.14), a power-law with exponential cut-off (Equation 2.10) and a log-parabolic spectrum (Equation 2.11). The results from the Forward Folding method are compared to a fit of the correction factor method spectrum. The fit is performed with a power-law and a power-law with exponential cut-off. In order to compare the results of the standard correction factor method and the Forward Folding method, the same fit range (0.4 TeV - 25 TeV) is chosen. All events within this fit range are included in both methods. In comparison, the fit range for the toy Monte-Carlo was 90 GeV to 45 TeV. In contrast to the toy Monte-Carlo, we no longer assume a fixed zenith angle of twenty degrees. Hence, the migration matrix, like the effective area, is now zenith angle dependent. A time average over zenith angles is taken. This means that the overall threshold is partially determined by the

highest threshold from the largest zenith angle observations. Therefore, the method is tested above 400 GeV, as a first approximation, in order to be sensitive to an exponential cut-off at TeV energies.

4.3.1 Application to the Crab Nebula

The Crab Nebula is the standard candle of TeV γ-ray astronomy. It is a pulsar wind nebula within the Milky Way, which is powered by the Crab pulsar located at the center of the nebula. No evidence for variability of the Crab Nebula in the TeV domain is known to date [31] [75]. Its constant flux is the highest for any γ-ray source in the sky and is only surpassed by variable, flaring sources. Since no variability has been observed at TeV energies, the well-investigated constant flux therefore allows for extensive cross-checks on the instrument and analysis. Such a cross-check of the unfolding method against the stanard correction factor method is performed on 3 h 20 min of data. The observations of the Crab Nebula have been taken by VERITAS before the camera upgrade (see Chapter 3) in 2012. All data shown have passed quality (good weather, no hardware failure) checks. The significance has been calculated according to Li & Ma (1983) [104] (Equation 17). The number of off-events is extracted from a background modeled with reflected regions [9].
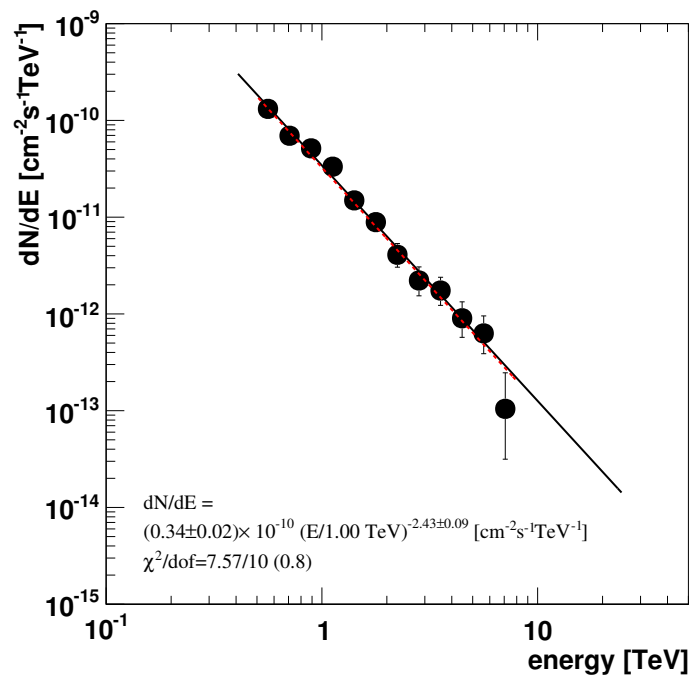
Figure 4.20: Correction factor method spectrum of the Crab Nebula fit with a power-law, compared to the Whipple observation (red dashed line). The differential flux is shown as a function of energy.

The spectrum from the correction factor method is plotted in Figure 4.20. (The analy-

sis software used to perform the correction factor method, is the standard analysis chain for VERITAS contained in the EVENTDISPLAY package.) The differential flux as a function of reconstructed energy E_{rec} is displayed. Because of the large number of events (841 ON events and 62.9 background events, resulting in 47.5σ significance), the data points can be binned in steps of $\log(\Delta E) = 0.1$ in the energy range 400 GeV to 25 TeV. The spectrum is compatible with a power-law. Fitting the data points with a power-law yields a $\chi^2/\text{d.o.f.} = 0.8$. The flux normalization $\phi_0 = (3.4 \pm 0.2) \times 10^{-7} \text{ m}^{-2} \text{ s}^{-1} \text{ TeV}^{-1}$ and spectral index $\Gamma = 2.43 \pm 0.09$ are consistent with the values observed by Whipple [147] displayed as a red dashed line.

The Forward Folding with a power-law spectrum is shown in Figure 4.21. The differential flux as function of energy is displayed. The spectrum is plotted together with the corresponding error band against the data points from Eventdisplay. The values extracted with this method are a normalization of $\phi_0 = (3.36 \pm 0.16) \times 10^{-7} \text{ m}^{-2} \text{ s}^{-1} \text{ TeV}^{-1}$ and spectral index $\Gamma = 2.45 \pm 0.06$. This is consistent with the correction factor method results within error margins.

There is no significant sign of an exponential high-energy cut-off. The Forward Folding spectrum with exponential cut-off is favored with a significance of 1.8σ over a power-law.
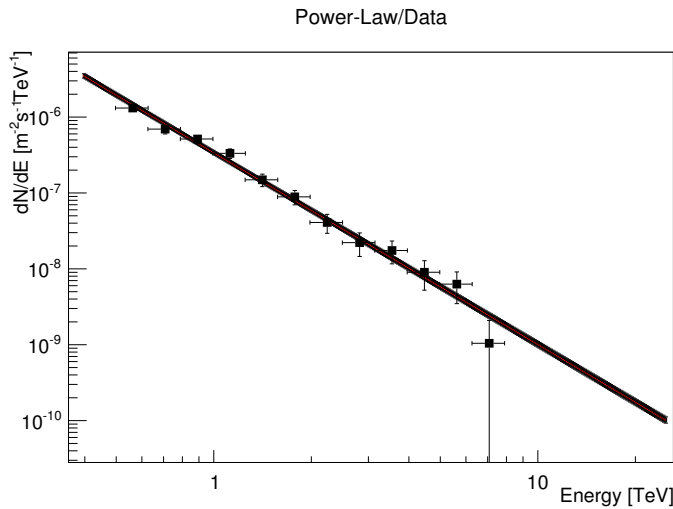
Figure 4.21: Forward Folding with a power-law spectrum compared to the data points from the correction factor method. The differential flux is displayed as function of the true energy in TeV for the Crab Nebula. The red line is the spectrum extracted from the unfolding method, together with error bars.

4.3.2 Application to Markarian 421

Markarian 421 (Mrk 421) is a highly variable Active Galactic Nucleus (AGN) [124] [24]. It is one of the brightest extra-galactic TeV sources. Recently it showed unprecedented flaring activity reaching up to $\sim$ 10 times the flux of the Crab Nebula in April 2013 (ATel #4976). A comparable flare occured in February 2010. Mrk 421 is well known to have an intrinsic high

energy cut-off not due to EBL absorption (see Section 2.1.2). This is because of the relatively moderate redshift z = 0.031. Mrk 421 has been observed by VERITAS as part of a dedicated multi-wavelength (MWL) campaign [70].

To test the unfolding method on a source with a well studied intrinsic high-energy cut-off, 18 h 20 min of VERITAS data from the February 2010 flare are taken. Only runs passing quality checks are considered. Data taken with at least three of the four VERITAS telescopes are included. To extract the signal, the background events are subtracted from the on source events, using reflected regions [9]. Overall, 494 OFF events are subtracted from the 17320 events in the ON region. This leads to a detection significance of 254.3σ according to Li & Ma (Equation 17) [104].

The Eventdisplay (correction factor method) spectrum is shown in Figure 4.22. The flux is plotted as a function of reconstructed energy. The binning and range are identical to the Crab Nebula spectrum. The Mrk 421 spectrum is again fit with a power-law function. The resulting flux normalization is $\phi_0 = (1.39 \pm 0.01) \times 10^{-6}$ m^{-2} s^{-1} TeV^{-1} with a spectral index $\Gamma = 2.63 \pm 0.01$. The flux level is far beyond the Crab Nebula flux level shown as a red dashed line, reaching 4 C.U. on average. In contrast to the Crab Nebula, the χ^2/d.o.f. = 35.6 shows that the spectrum is not well described by a power-law.
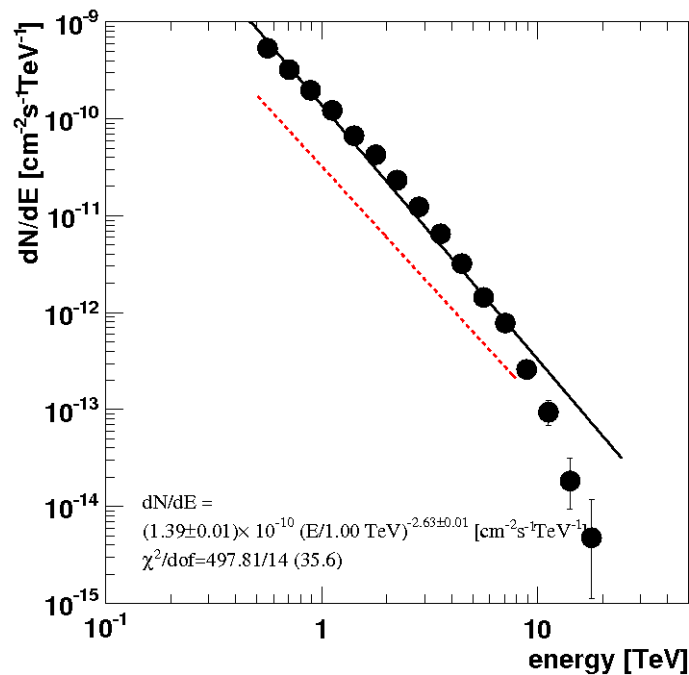
Figure 4.22: Correction factor method spectrum of Mrk 421 fit by a power-law: differential flux as a function of reconstructed energy. The dashed red line is the Crab Nebula flux level.

Since the curvature is clearly visible, a fit with exponential cut-off is performed (Figure 4.23). This provides an improved reduced χ^2/d.o.f. = 0.4
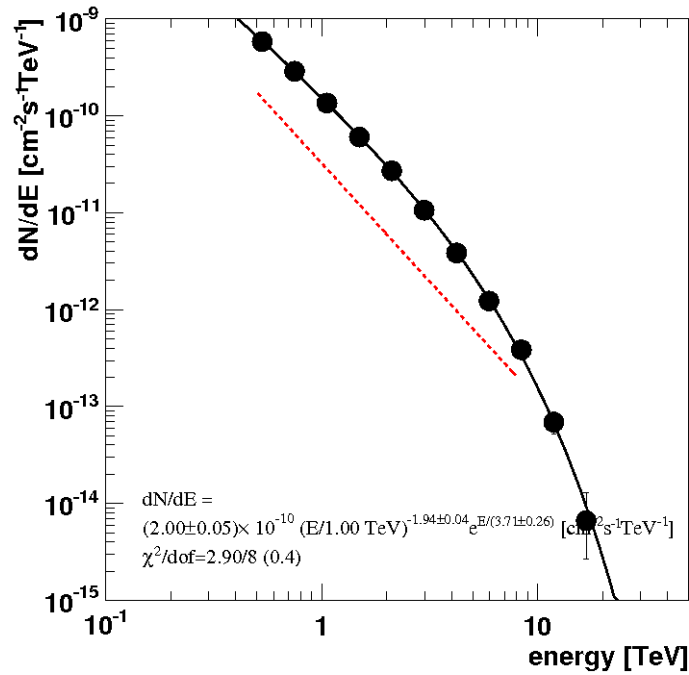
Figure 4.23: Correction factor method spectrum of Mrk 421 fitted by a power-law with exponential cut-off: differential flux as a function of energy.
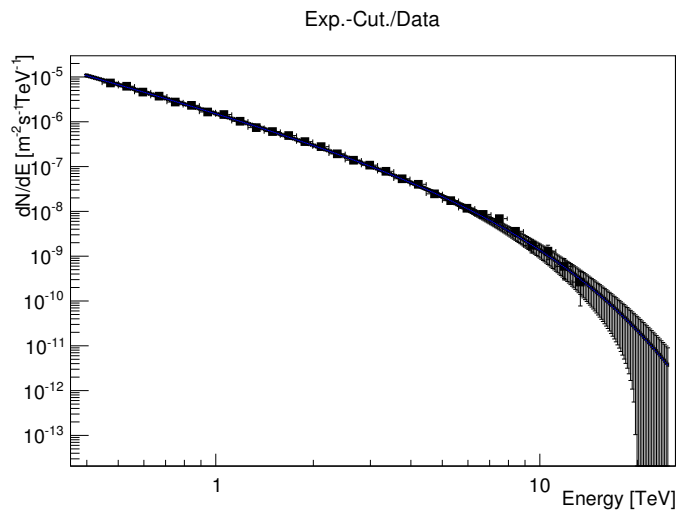
Figure 4.24: Mrk 421 spectrum unfolded with a power-law with exponential cut-off. The differential flux of the model with error band is shown together with the standard correction factor method data points as a function of energy.

In Figure 4.24 the same correction factor method data points binned in $\log(\Delta E) = 0.15$ are displayed. On top of those discrete data points, the spectrum unfolded with a power-law with an exponential cut-off is shown with its error band. The flux normalization resulting from

the fit between 400 GeV and 25 TeV is $\phi_0 = (2.00 \pm 0.05) \times 10^{-6}$ m^{-2} s^{-1} TeV^{-1} with a spectral index $\Gamma = 1.94 \pm 0.04$. The best fit for the cut-off energy is $E_C = 3.71 \pm 0.26$ TeV. Hence, a high energy cut-off is clearly detectable.

Again, the standard correction factor method is compared to the Forward Folding models. The likelihood-ratio test shows that a spectrum with an exponential cut-off is favored with 15.6σ over a simple power-law.

Forward Folding of the spectrum with a power-law results in a flux normalization of $\phi_0 = (1.298 \pm 0.012) \times 10^{-6}$ m^{-2} s^{-1} TeV^{-1} and spectral index $\Gamma = 2.38 \pm 0.01$. The corresponding error band on the differential flux as a function of energy is plotted together with the correction factor method data points in Figure 4.25. The values are consistent with the standard correction factor method. Nevertheless, the spectrum is clearly not well described by a power-law.

Hence, the spectrum is also unfolded with a power-law with exponential cut-off: this results in a normalization of $\phi_0 = (1.96 \pm 0.05) \times 10^{-6}$ m^{-2} s^{-1} TeV^{-1}, with an index $\Gamma = 1.99 \pm 0.03$ and a cut-off energy $E_C = 3.65 \pm 0.22$ TeV as displayed in Figure 4.24. The parameters show a good agreement to the standard correction factor analysis within error margins.
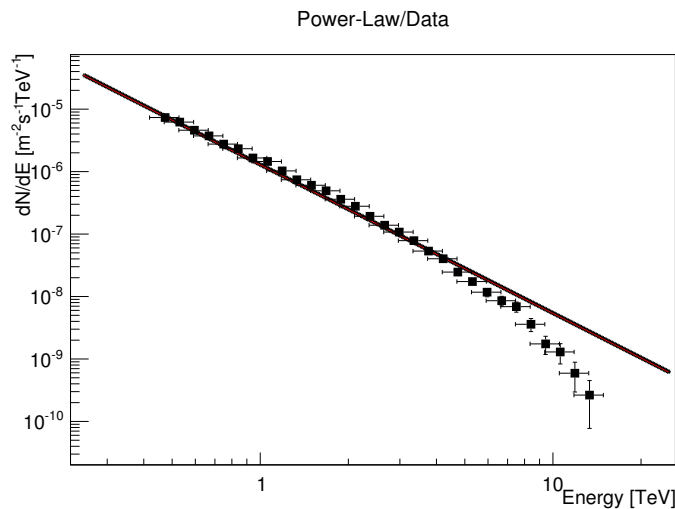
Figure 4.25: Unfolding the Mrk 421 spectrum with a power-law: the differential flux of the power-law model with error band is displayed together with the correction factor method data points as a function of energy.

Finally, the spectrum is unfolded with a log-parabolic model (Equation 2.11). The resulting normalization is $\phi_0 = (1.52 \pm 0.02) \times 10^{-6}$ m^{-2} s^{-1} TeV^{-1}, with an index $a = 2.35 \pm 0.02$ and $b = 0.22 \pm 0.02$. The Forward Folding result with error band is illustrated in Figure 4.26 together with the standard correction factor method data points. The significance by which a log-parabola shape is favored over a power-law is 14.9σ. Hence, the log-parabola spectrum is not favored as significantly over a power-law as the exponential

cut-off (15.6σ). The likelihood-ratio test does not allow for discrimination between these two different models with the same number of parameters. However, the exponential cut-off log-parabola model (Equation 2.12) is favored over a power-law with exponential cut-off by 7.5σ, and so provides a better representation of the data than the cut-off model without log-parabolic curvature.
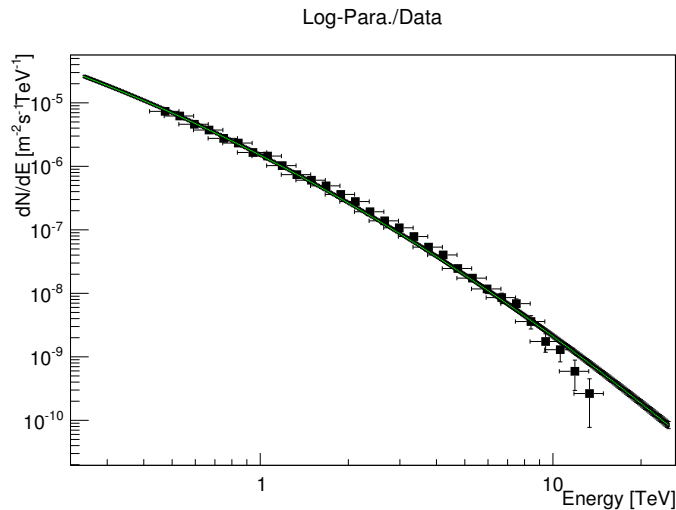

Figure 4.26: Mrk 421 spectrum unfolded with a log-parabolic spectrum: the differential flux of the model with errors is displayed together with the standard correction factor method data points as a function of energy.

In conclusion, the Forward Folding has been tested on spectra of the Crab Nebula and Mrk 421 and proven to yield results that are consistent with the standard correction factor analysis. With this method, it is possible to quantitavely distinguish between a spectrum with such characteristics and a pure power-law. Moreover, the error on the reconstructed spectral parameters is smaller after unfolding than for the standard correction factor method.

Chapter 5

VERITAS observations of Mrk 421

In this chapter, Forward Folding is applied to VERITAS data of Markarian 421 (Mrk 421) dating from February 2010 to May 2013. The motivation for this analysis is presented in Section 5.1.1. In Section 5.1.2, the observed γ-ray source, Mrk 421, is introduced. The results from the Forward Folding analysis are presented in Section 5.2 and interpreted in Section 5.3.

5.1 Introduction

5.1.1 Measuring spectral cut-offs

Physical mechanisms leading to spectral cut-offs have been introduced in Chapter 2. Detecting spectral cut-offs reveals information about the acceleration mechanism at work in the source. A power-law with an exponential cut-off can be motivated by a maximal energy available for acceleration in the source (see Section 2.3.2). Log-parabolic spectra can be modeled by an energy-dependent stochastic acceleration probability (see Section 2.3.3).

It is the goal of this work to measure the spectrum of Mrk 421 with the highest possible precision. This allows discrimination between different spectral shapes, such as a power-law, a power-law with an exponential cut-off or a log-parabola spectrum. In Chapter 4 it has been demonstrated that this can be achieved by Forward Folding, a powerful tool to reconstruct spectra of γ-ray sources. In contrast to the correction factor method, which is biased towards the model assumed in the initial simulation (a power-law in most cases), Forward Folding takes into account the complete instrument response function including effective area and energy migration matrix. An assumption about the spectral shape is only made in the final stage of the spectral reconstruction. Therefore, in this chapter, Forward Folding is used to measure spectral cut-offs of Mrk 421 with VERITAS.

5.1.2 A short history of VHE observations of Mrk 421

Mrk 421 is a highly variable Active Galactic Nucleus (AGN). It was discovered as a TeV γ-ray source in 1992 by the Whipple telescope [124]. Mrk 421 is one of the brightest extra-galactic TeV sources and the first extra-galactic source to be detected at TeV energies. Recently it

showed unprecedented flaring activity reaching up to ~ 10 times the flux of the Crab Nebula in April 2013 (ATel #4976). A comparable flare (up to ~ 8 times the Crab Nebula flux) occured in February 2010.

The γ-ray emission from Mrk 421 is well known to cut off at $\sim$ TeV energies. This high energy cut-off can not be due to interaction with the EBL photons, called EBL absorption (see Section 2.1.3). Although EBL absorption leads to a steeper spectrum at high energies for distant sources, this effect is neglible for Mrk 421, due to the relatively small redshift $z = 0.031$.

Observations with the Whipple telescope in 2001 by Krennrich et al. (2002) found a cut-off energy of $4.3 \pm 0.3_{\text{stat}} (-1.4 + 1.7)_{\text{syst}}$ TeV [102], and did not detect any significant variability in this cut-off energy. More recently, from MAGIC observations in 2004/5, Albert et al. (2007) [24] have found a cut-off energy of 1.44 ± 0.27 TeV. Concerning the underlying mechanism, they conclude that either the cosmic accelerator must be at its energy limit or that there is absorption intrinsic to the source.

In the previous observations with Whipple in 2001 [102] and HEGRA from December 1999 until May 2001 [10], the spectrum of Mrk 421 is seen to harden with increasing flux. Krennrich et al. (2002) [102] see a spectral hardening with a spectral index 1.89 ± 0.04 in the high flux state changing to a value of 2.72 ± 0.11 in the low flux state. A similar result has been obtained by CAT [71]. More recently, this observation has been confirmed by the MAGIC observations in 2004/5 [24]. From a power-law fit from 700 GeV to 4 TeV, they find a linear dependence of the spectral index on the flux normalization ϕ_0 at 1 TeV.

$$\Gamma = \text{constant} + \text{slope} \times \phi_0 \qquad (5.1)$$

The best fit (with a $\chi^2 = 43.4$ for 11 degrees of freedom) results in a slope $= (0.027 \pm 0.002) \times (10^{11} \text{ TeV s cm}^2)$.

Spectral hardening of Mrk 421 spectra has also been observed in X-ray emissions. Fossati et al. (2000) [67] see a sign of spectral hardening with increasing flux, accompanied by a shift in the peak of the synchroton component to higher energies. They interpret this as an injection of electrons at progressively higher energies. Albert et al. (2007) have seen a correlation at a significance of 2.4σ between the X-ray and γ-ray fluxes in a state of low to medium activity of the source. This supports the idea of a leptonic origin of the γ-rays. Similarly to Fossati et al. (2000) [67] they see a shift of the Inverse Compton peak to higher energies. This can explain the spectral hardening, because the flatter part of the Inverse Compton peak gets shifted up to TeV energies. Hence at higher energies a spectral softening would be expected as a result, for example, of a very-high-energy cut-off in the particle distribution, the falling cross-section due to the Klein-Nishina effect or external attenuation effects from nearby radiation fields.

5.2 Observations of Mrk 421

Mrk 421 is observed by VERITAS as part of a larger MWL campaign. The multi-wavelength data allow further constraints to be placed on the models for the Synchroton and Inverse Compton emission. In particular, it is interesting to look for a correlation between X-ray and γ-ray fluxes. A correlation between the Synchroton emission in X-rays and Inverse Compton emission in γ-rays would point to a common acceleration mechanism and region. This work, however, focusses on VERITAS observations at very-high-energies.

VERITAS observations are taken during cloudless, dark nights. The observations are usually taken in seperate data runs lasting 20 to 30 minutes. Data runs during bad weather or with less than three telescopes are excluded. Data runs during a hardware failure are usually also rejected after quality checks.

For a detailed description of the VERITAS array of Cherenkov telescopes see Chapter 3. In particular, a short overview of observations and the data analysis framework of VERITAS is given in Section 3.2.3.

5.2.1 VERITAS data

In this section, the analysis of 106 hours[1] of VERITAS data is presented. The VERITAS observations of Mrk 421 took place between February 2010 and May 2013. All data included in this analysis were taken after the relocation of Telescope 1, with 58 hours taken before the camera upgrade in 2012 (see Section 3.2) and the rest taken following the upgrade. The summary of the data obtained for Mrk 421 in each observing season is given in Table 5.1.

Season	Observation time [h]	Significance [σ]	# ON events	# OFF events
2009/2010	11.5	222	12597	292.2
2010/2011	12	42.6	1565	380.6
2011/2012	34.3	51.2	2150	498.5
2012/2013	48.3	331	41473	3222.8

Table 5.1: Summary of observations of Mrk 421 from February 2010 to May 2013. The total observation time (including dead time) in each season is given together with the number of events in the ON region and OFF region respectively. OFF events are scaled by the normalization factor of 0.08. This takes into account the larger number of OFF regions in the reflected region model. From the number of OFF events and ON events a detection significance for Mrk 421 has been calculated (see Section 3.2.3).

---

[1]Observation times are given as run times, including dead time.

5.2.2 Nightly light curve

The complete nightly light curve with the integral flux [m^{-2}s^{-1}] above 300 GeV as a function of the Modified Julian Date (MJD) is given in Figure 5.1. Figure 5.2 shows a zoomed in version of this light curve for each observing season. For each night, a spectrum has been obtained. The spectra are tested with a power-law and a power-law with exponential cut-off to see which model is preferred. If a power-law with an exponential cut-off is favored by more than 3σ, the integral flux above 300 GeV is calculated from this spectrum. Otherwise the integral flux above 300 GeV is calculated from the power-law.
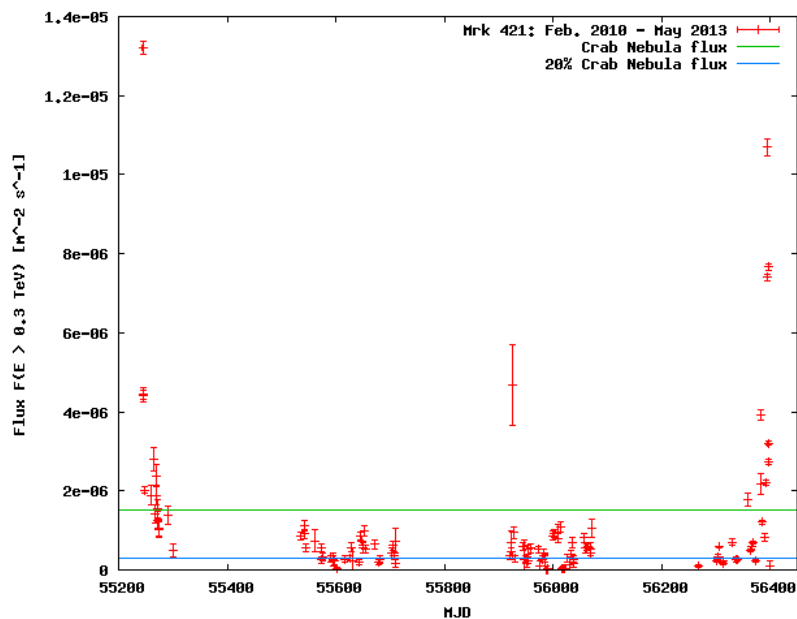
Figure 5.1: Nightly lightcurve with the flux [m^{-2}s^{-1}] above 300 GeV as a function of the MJD. VERITAS observations date from Feb. 2010 to May 2013.

The horizontal lines mark constant flux levels, with 20% the Crab Nebula flux displayed in blue, 100% Crab Nebula flux is shown in green.

In the 2009/2010 observing season, see Figure 5.2 (a), a major flare occured in February 2010 reaching up to 8 times the flux of the Crab Nebula on February 17, 2010. In the following season 2010/2011, see Figure 5.2 (b), Mrk 421 is in a relatively low state. However variability with up to a factor of 2 difference in the flux on subsequent nights can be observed. In the 2011/2012 observing season, see Figure 5.2 (c), a single flare reaching up to 3 times the flux of the Crab Nebula occured on December 29, 2011. The duration of the single data run on this night is 13 minutes only, leading to a significant uncertainty in the flux estimation. For the rest of the season, Mrk 421 is in a similarly low flux state to the previous season. In the beginning of the 2012/2013 observing season, see Figure 5.2 (d), Mrk 421 remains in a relatively low state, but in April 2013, another major flare reaching up to 8 times the flux of the Crab Nebula occurs. It is clear from these light curves that Mrk 421 is a highly variable source.
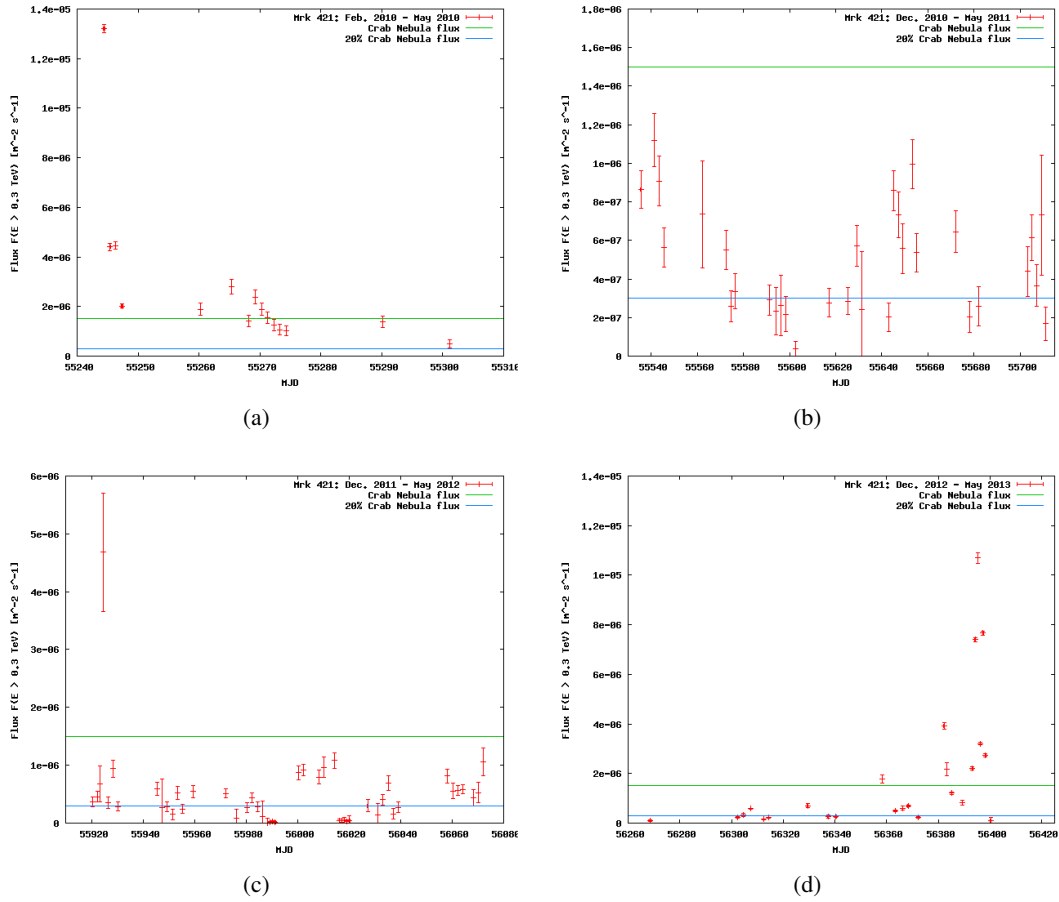
Figure 5.2: Nightly light curves of Mrk 421 showing the integral flux $[\text{m}^{-2}\text{s}^{-1}]$ above 300 GeV as a function of the MJD.

Each panel in this plot shows a single season. Observations from Feb. 2010 to May 2010 are displayed in (a), observations from Dec. 2010 to May 2011 are shown in (b), observations from Dec. 2011 to May 2012 are shown in (c) and observations from Dec. 2012 to May 2013 are shown in (d). The horizontal lines mark constant flux levels, with 20% the Crab Nebula flux displayed in blue and 100% Crab Nebula flux shown in green.

5.2.3 Analysis procedure and data selection

The flux variability shown in the lightcurves demonstrates the necessity to proceed carefully with the spectral analysis. The goal is to measure very-high-energy cut-offs and spectral variability as a function of the flux level. Therefore, the data is binned in groups of nights (resp. runs) with neglibible nightly (resp. intra-nightly) flux variability.

In order to be able to detect an exponential cut-off with a significance of 3σ, a detection significance of the source of at least 50σ to 70σ is required. This result is calculated from Figure 4.10: For a source with 20% Crab Nebula flux, a significance of 3σ for an exponential cut-off at 1.2 TeV is obtained in 19 h. The detection significance for the 12 h in 2010/11 was 42.6σ, when the flux level of Mrk 421 in was 20% Crab Nebula flux.

Hence a detection significance of about $42.6\sigma \times \sqrt{\frac{19h}{12h}} = 54\sigma$ is required for an exponential cut-off at 1.2 TeV with a significance of 3σ.

The data bins with at least 60σ detection significance are obtained by the following procedure:

- All single nights with at least 60σ detection significance of Mrk 421 constitute at least one single bin.

- Nights with a detection significance of more than 100σ are split into multiple bins.

  - Each bin should have an equal number of runs and a detection significance of at least 60σ if possible.

  - The three nights with a detection significance of $\sim 190\sigma$ (2010: Feb. 17 and 2013: Apr. 12 and Apr. 15) are split into 4 bins per night.

  - The two nights with a detection significance of $\sim 120\sigma$ (Apr. 13 and Apr. 14 2013) are split into two bins per night.

- The remaining nights are ordered according to their flux, and split into 3 equal bins of 70σ each. In the following these bins are called Low state bins.

  - All nights with an integral flux above 300 GeV below the threshold $F(E > 300 \text{ GeV}) = 2 \times 10^{-7}\text{m}^{-2}\text{s}^{-1}$ do not show a significant signal and are ignored.

  - Low state bin 1 includes nights with an integral flux above 300 GeV between $2 \times 10^{-7}\text{m}^{-2}\text{s}^{-1}$ and $7.7 \times 10^{-7}\text{m}^{-2}\text{s}^{-1}$.

  - Low state bin 2 includes nights with an integral flux above 300 GeV between $7.95 \times 10^{-7}\text{m}^{-2}\text{s}^{-1}$ and $1.53 \times 10^{-6}\text{m}^{-2}\text{s}^{-1}$.

  - Low state bin 3 includes nights with an integral flux above 300 GeV between $1.74 \times 10^{-6}\text{m}^{-2}\text{s}^{-1}$ and $4.68 \times 10^{-6}\text{m}^{-2}\text{s}^{-1}$.

The details for each of the data bins are displayed in Table 5.2.

Bin	Season	Obs. time [h]	Sign. [σ]	# ON events	# OFF events
2010 Feb. 17 bin 1	2009/2010	1.0	113.6	2843	25.8
2010 Feb. 17 bin 2	2009/2010	1.3	110.9	2794	32.5
2010 Feb. 17 bin 3	2009/2010	1.0	77.6	1401	19.5
2010 Feb. 17 bin 4	2009/2010	1.0	79.2	1400	14.4
2010 Feb. 18	2009/2010	1.7	73.6	1463	43.2
2010 Feb. 19	2009/2010	1.0	62.2	1044	30.8
Bin 1 (Low state)	2010-2013	31.6	76.6	5890	1630.3
Bin 2 (Low state)	2010-2013	8.8	71.0	2800	416.7
Bin 3 (Low state)	2010-2013	4.0	68.7	1765	131.1
2013 Mar. 31	2012/2013	1.0	68.8	1514	78.3
2013 Apr. 11	2012/2013	3.2	76.9	2509	244.1
2013 Apr. 12 bin 1	2012/2013	1.4	101.7	2956	107.6
2013 Apr. 12 bin 2	2012/2013	1.5	108.1	3226	103.6
2013 Apr. 12 bin 3	2012/2013	1.5	99.7	2637	72.5
2013 Apr. 12 bin 4	2012/2013	1.0	77.0	1445	26.3
2013 Apr. 13 bin 1	2012/2013	1.0	105.2	2634	42.1
2013 Apr. 13 bin 2	2012/2013	0.5	59.6	833	12.0
2013 Apr. 14 bin 1	2012/2013	2.0	89.9	2603	136.8
2013 Apr. 14 bin 2	2012/2013	2.5	78.6	2308	173.8
2013 Apr. 15 bin 1	2012/2013	1.5	105.8	3128	104.8
2013 Apr. 15 bin 2	2012/2013	1.5	110.3	3443	120.7
2013 Apr. 15 bin 3	2012/2013	1.1	91.7	2181	53.9
2013 Apr. 15 bin 4	2012/2013	1.2	59.4	956	28.5
2013 Apr. 16	2012/2013	2.2	77.8	1514	78.3

Table 5.2: Data bins of the Mrk 421 observations: the total observation time (including dead time) in each data bin is given together with the number of events in the ON region and OFF regions respectively. OFF events are scaled by the normalization factor of 0.08. This takes into account the larger number of OFF regions in the reflected region model. From the number of OFF events and ON events a detection significance for Mrk 421 has been calculated (see Section 3.2.3).

The goal of this procedure is to obtain data bins with similar flux levels. It is therefore checked if there is flux variability within these data bins. If flux variability is detected, it is checked if spectral variability is also present in the energy spectra. Flux and spectral variability within a bin would lead to creating an average spectrum over different physical states, which would be detrimental to this study.

Hence, the procedure is the following:

- Check each data bin for flux variability.

- If there is flux variability check for spectral variability.

The observational data bins that exhibit flux and spectral variability are later excluded from the analysis as a cross-check. In this way, all results are compared first including and then excluding the variable bins.

Additionally, the energy range of the observations within each data bin has to be considered carefully. Combining different spectral and flux states over different energy ranges could introduce curvature into the averaged spectrum, even if such curvature is not present in the source spectrum.

Flux variability

Before the application of the Forward Folding algorithm to the data bins, it is checked if there is flux variability within the data bins. Each of the data bins has been tested for flux variability by a χ^2-test. The nightly bins are subdivided into runs and the mixed bins are subdivided into nights. For each of these sub-bins, the mean integral flux above 300 GeV and the corresponding error is calculated. The result is fit to a constant. The χ^2 and d.o.f. are extracted from the fit, and the probability and significance are calculated. A low probability (high significance) indicates that the light curve is not consistent with a constant flux. The results for each data bin are shown in Table 5.3.

Three data bins,

- February 19, 2010

- April 12, 2013, bin 4

- Low state, bin 1

show flux variability with a significance $> 5\sigma$.

For those periods, an energy spectrum for each sub-bin is obtained.

Bin	χ^2	d.o.f.	Probability	Significance [σ]
2010 Feb. 17 bin 1	1.8	2	0.4	0.83
2010 Feb. 17 bin 2	6.1	2	0.05	2.0
2010 Feb. 17 bin 3	11	1	9e-4	3.3
2010 Feb. 17 bin 4	3.5	1	0.06	1.87
2010 Feb. 18	1.53	2	0.5	0.73
2010 Feb. 19	32	1	1.5e-8	**5.7**
Bin 1 (Low state)	320	60	4e-37	**12.7**
Bin 2 (Low state)	62.6	20	2.8e-6	4.7
Bin 3 (Low state)	34.4	13	1e-3	3.3
2013 Mar. 31	1.28	1	0.258	1.1
2013 Apr. 11	12.3	5	0.03	2.2
2013 Apr. 12 bin 1	12.4	2	2e-3	3.1
2013 Apr. 12 bin 2	5.5	2	0.06	1.9
2013 Apr. 12 bin 3	9.7	2	8e-3	2.7
2013 Apr. 12 bin 4	35	1	3.3e-9	**5.9**
2013 Apr. 13 bin 1	17	1	3.7e-5	4.1
2013 Apr. 13 bin 2	3.5	1	0.06	1.9
2013 Apr. 14 bin 1	18.6	3	3.3e-4	3.6
2013 Apr. 14 bin 2	12.6	4	0.013	2.5
2013 Apr. 15 bin 1	9.1	2	0.01	2.6
2013 Apr. 15 bin 2	9.5	2	9e-3	2.6
2013 Apr. 15 bin 3	1.7	2	0.43	0.8
2013 Apr. 15 bin 4	4.5	2	0.11	1.6
2013 Apr. 16	23.4	4	1e-4	3.8

Table 5.3: To test if the flux is consistent with a constant in each data bin, the data bin is divided into sub-bins (individual runs or respective nights, as described). The resulting light curve in each data bin is fit with a constant flux. The resulting χ^2 is displayed together with the probability for the data to be consistent with a constant. The significance of the χ^2-test, by which the constant flux is rejected, is given in the last column. Significances of more than 5σ are displayed as bold numbers.

February 19, 2010

(a)

(b)
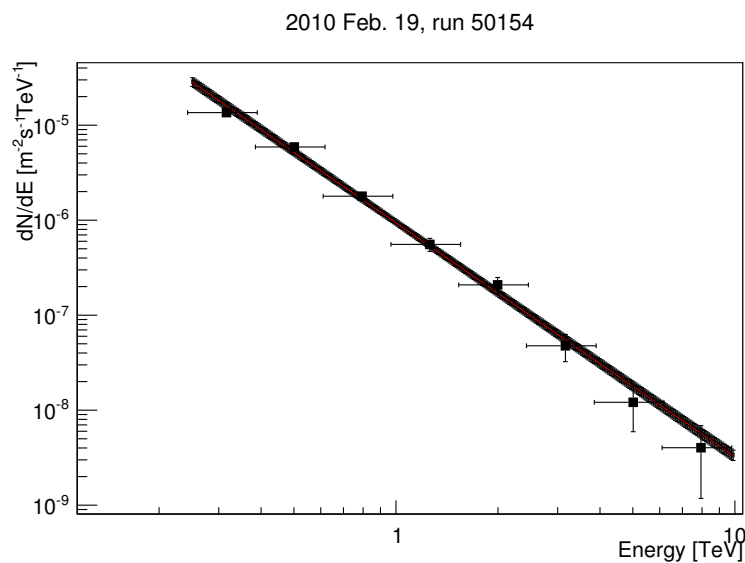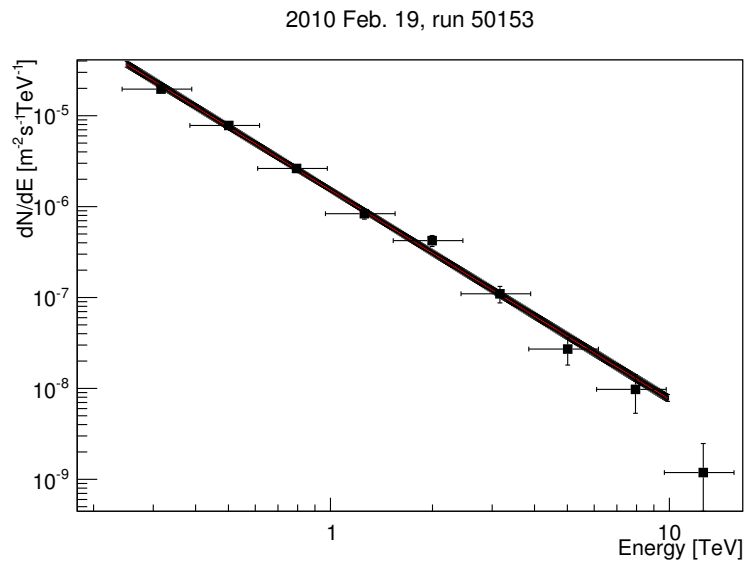
Figure 5.3: Forward Folding with a power-law spectrum in the common energy range of both runs, 251 GeV - 10 TeV. The first run 50153 is shown in (a), the second run 50154 is shown in (b). The correction factor method data points are displayed together with the error band from Forward Folding.

The nightly data of February 19, 2010 consists of 2 data runs. For run 50153, the energy bins containing events cover an energy range from $E_{\mathrm{min}} = 251$ GeV to $E_{\mathrm{max}} = 15.8$ TeV[2]. The energy range with events for run 50153 is $E_{\mathrm{min}} = 251$ GeV to $E_{\mathrm{max}} = 10.0$ TeV.

---

[2]E_{min} is the low edge of the lowest energy bin containing events, and E_{max} is the upper edge of the highest energy bin containing events.

The energy range for the Forward Folding is chosen to be the overlap in the energy ranges of both runs. This is necessary as spectral curvature can lead to different spectral indices over different energy ranges. Forwald Folding with a power-law is therefore applied on the energy range from $E_{\text{min}} = 251$ GeV to $E_{\text{max}} = 10.0$ TeV.

Run	χ^2	d.o.f.	ϕ_0 [m^{-2}s^{-1}TeV^{-1}]	Γ
50153	39.5	30	$(1.54 \pm 0.08) \times 10^{-6}$	2.30 ± 0.06
50154	41.1	30	$(0.952 \pm 0.060) \times 10^{-6}$	2.46 ± 0.08

Table 5.4: Feb. 19, 2010 sub-bins: Results from Forward Folding with a power-law over the energy range from $E_{\text{min}} = 251$ GeV to $E_{\text{max}} = 10.0$ TeV. The flux normalization at 1 TeV (ϕ_0) is listed together with the spectral index Γ, the χ^2 and the number of degrees of freedom.

The results from the Forward Folding are displayed in Table 5.4. The spectra are compatible with a power-law, as shown by the χ^2. A likelihood-ratio test is also performed to assess if the data are better described by a power-law with exponential cut-off than by a power-law. This test results in a significance $< 1.5\sigma$, confirming that the spectra are compatible with a power-law.

The spectral indices of the two data runs differ from each other by about one standard deviation. Hence, there is no significant sign of spectral variability. The Forward Folding spectra of runs 50153 and 50154 are shown in Figure 5.3 (a) and (b) respectively.

April 12, 2013, bin 4

Bin 4 of the April 12, 2013 nightly observations also consists of 2 data runs. For run 67965, the energy bins containing events cover an energy range from $E_{\text{min}} = 398$ GeV to $E_{\text{max}} = 15.8$ TeV. The energy range of the second run 67966 is between $E_{\text{min}} = 1$ TeV and $E_{\text{max}} = 10$ TeV. Forward Folding with a power-law is applied to the overlapping energy range (1 TeV - 10 TeV) of both data runs.

Run	χ^2	d.o.f.	ϕ_0 [m^{-2}s^{-1}TeV^{-1}]	Γ
67965	19.2	18	$(3.47 \pm 0.34) \times 10^{-6}$	3.06 ± 0.14
67966	20.6	18	$(5.41 \pm 0.45) \times 10^{-6}$	3.06 ± 0.12

Table 5.5: Apr. 12, 2013 sub-bins: Results from Forward Folding with a power-law on the energy range from $E_{\text{min}} = 1$ TeV to $E_{\text{max}} = 10.0$ TeV. The flux normalization at 1 TeV (ϕ_0) is listed together with the spectral index Γ, the χ^2 and the number of degrees of freedom.

2013 Apr. 12, bin 4, run 67965

(a)

2013 Apr. 12, bin 4, run 67966
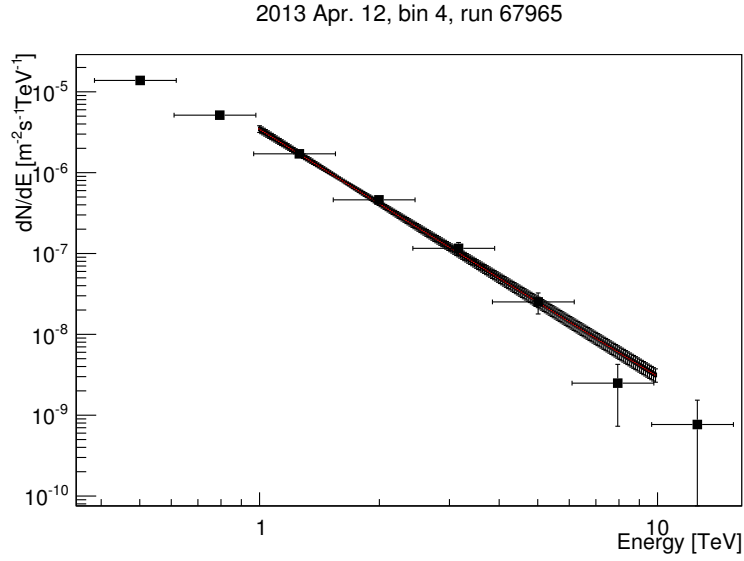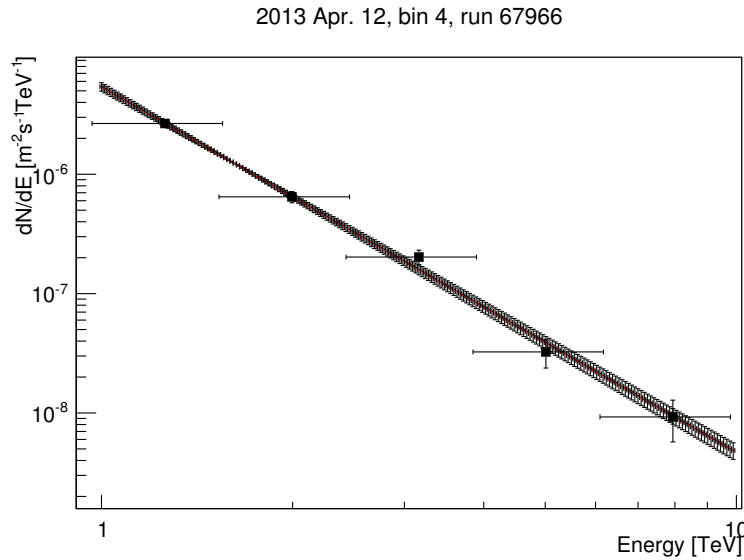
(b)

Figure 5.4: Forward Folding with a power-law spectrum is applied to the common energy range of both runs, 1 TeV - 10 TeV. The first run 67965 is shown in (a), the second run 67966 is shown in (b). The correction factor method data points are displayed together with the error band from Forward Folding.

The results from the Forward Folding are displayed in Table 5.5. The spectra are compatible with a power-law, as shown by the χ^2. A likelihood-ratio test is also performed to assess if the data are better described by a power-law with exponential cut-off than by a power-law. This test results in a significance for an exponential cut-off of 1.5σ for the first run and 0.94σ for the second run, confirming that the spectra are compatible with a power-law. Since the spectral indices are in complete agreement with each other, there is no sign of spectral variability. The Forward Folding spectra of runs 67965 and 67966 are shown in Figure 5.4.

Low state bin 1
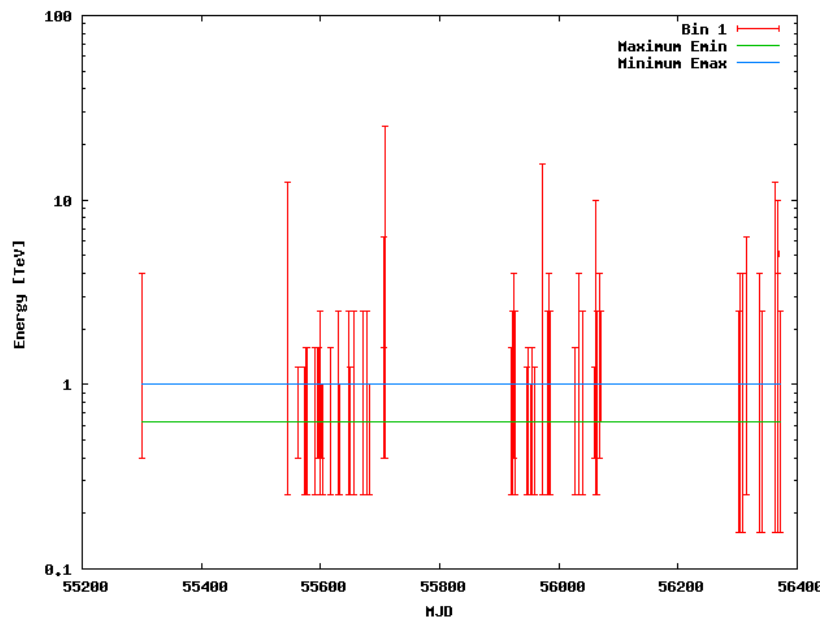
Figure 5.5: Low state bin 1. Energy range of the nightly energy spectra as a function of time, given by the MJD. The smallest $E_{\max} = 1$ TeV is displayed in blue. The largest $E_{\min} = 631$ GeV is displayed in green.
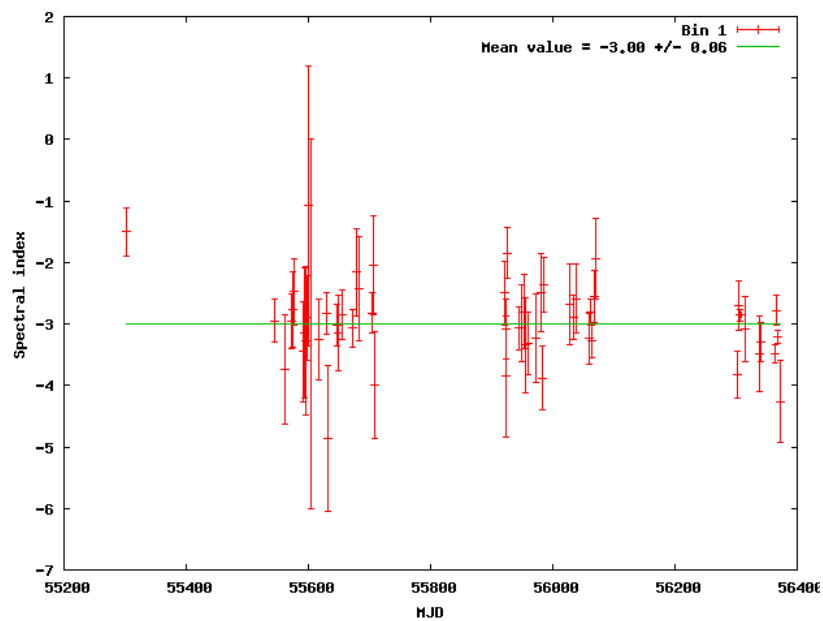
Figure 5.6: Low state bin 1. Spectral index for each individual night, given by the MJD. The mean value $\Gamma = 3.00 \pm 0.06$ is displayed as a green line

Low state bin 1 includes data from multiple nights, and has the lowest flux level overall. This bin is divided into nightly sub-bins. The usable energy range of the sub-bins varies dramatically, with $E_{\min}$ ranging from 158 GeV to 631 GeV, and $E_{\max}$ ranging from 1 TeV to 25.1 TeV. The energy range of each sub-bin is shown in Figure 5.5. A spectral fit could not be performed over the energy range common to all sub-bins as this range is so small (631 GeV to 1 TeV) that statistics are severly limited. Instead a broader range from 316 GeV to 3.163 TeV was used.

The distribution of spectral indices obtained from the power-law fit is displayed in Figure 5.6. The mean value of spectral indices, obtained from a fit with a constant, is $\Gamma = 3.00 \pm 0.06$. The fit with a constant yields a $\chi^2 = 77$ for 54 degrees of freedom. This corresponds to a probability of 0.026 equivalent to a significance of 2.3σ for the data to be consistent with a constant spectral index. Hence there is no significant sign for spectral variability.

Spectral analysis

For each data bin displayed in Table 5.2 a spectrum is obtained (see appendix A). A power-law and a power-law with an exponential cut-off is fit to the energy spectra. Both the correction factor method and Forward Folding are applied and compared over the energy range from 251 GeV to 15.8 TeV, to be sensitive to a possible cut-off. For a cross-check, data bins which do not cover this energy range completely are later excluded from the analysis. In the case of a power-law, the index depends on the energy range if curvature is present. Furthermore, the parameters of a power-law with exponential cut-off can also depend on the energy range.
A F-test is performed using the χ^2 and d.o.f. from the correction factor method for a power-law and a power-law with an exponential cut-off respectively. The F-test significance for an exponential cut-off is compared to the significance for an exponential cut-off from the Forward Folding algorithm shown in Table 5.6. The low edge $E_{\min}$ of the lowest energy bin containing events is given for each time bin along with the corresponding upper edge $E_{\max}$ of the highest energy bin containing events. As the energy threshold and the maximal reconstructed energy are a function of the elevation at which the source is observed, the average elevation of each time bin is also given.

Bin	Elevation	E_{min} [GeV]	E_{max} [TeV]	F-test [σ]	Forward Folding [σ]
2010 Feb. 17 bin 1	78°	251	25.1	5.0	8.0
2010 Feb. 17 bin 2	80°	251	15.8	4.1	6.4
2010 Feb. 17 bin 3	61°	**398**	15.8	3.4	5.0
2010 Feb. 17 bin 4	50°	**631**	15.8	2.7	6.3
2010 Feb. 18	71°	251	**10**	3.2	5.5
2010 Feb. 19	75°	251	15.8	2.6	2.7
Bin 1 (Low state)	74°	158	25.1	3.0	-
Bin 2 (Low state)	76°	158	15.8	1.7	-
Bin 3 (Low state)	69°	158	15.8	2.9	3.8
2013 Mar. 31	78°	158	15.8	2.3	2.5
2013 Apr. 11	72°	158	**10**	3.3	4.4
2013 Apr. 12 bin 1	79°	158	15.8	3.3	4.8
2013 Apr. 12 bin 2	75°	158	15.8	2.7	5.2
2013 Apr. 12 bin 3	58°	251	**10**	3.2	5.5
2013 Apr. 12 bin 4	43°	**398**	15.8	3.3	6.6
2013 Apr. 13 bin 1	58°	251	15.8	3.9	6.8
2013 Apr. 13 bin 2	42°	**631**	15.8	2.1	3.7
2013 pr. 14 bin 1	76°	158	25.1	2.7	3.3
2013 Apr. 14 bin 2	71°	158	15.8	2.5	3.8
2013 Apr. 15 bin 1	75°	158	25.1	3.9	4.1
2013 Apr. 15 bin 2	78°	158	15.8	3.1	4.1
2013 Apr. 15 bin 3	55°	251	15.8	3.7	5.2
2013 Apr. 15 bin 4	36°	251	15.8	2.6	4.7
2013 Apr. 16	67°	158	**10**	1.8	3.6

Table 5.6: Results of the significance by which a power-law with an exponential cut-off is favored over a power-law for the correction factor method obtained from a F-test. These results are compared to the likelihood-ratio test significance obtained from Forward Folding. The fit of both methods is applied from 251 GeV to 15.8 TeV. The low energy edge E_{min} of the lowest energy bin, which has events, is shown together with the corresponding upper energy edge E_{max} of the highest energy bin, which has events. Data bins which do not cover the whole energy range in which the fit is performed, are displayed in bold. The energy threshold and therefore also E_{min} rise with decreasing elevation. The elevation is listed in the second column.

5.2.4 Forward Folding results

In this section, Forward Folding is applied to the data sample of Mrk 421 from February 2010 to May 2013. A power-law, a power-law with an exponential cut-off and a log-parabola

spectral model are used. This allows the spectral shape of the source to be studied as a function of flux level. Results are first obtained including all data bins. Bins that exhibit flux or spectral variability, or that do not have events over the entire energy range of the fit are then excluded, and the results are recalculated. This more conservative analysis provides a cross-check for the initial analysis that includes all data bins.

Power-law

Bin	ϕ_0 [10^{-6}m^{-2}s^{-1}]	Index Γ	F [10^{-6}m^{-2}s^{-1}]	χ^2 (9 d.o.f.)
2010 Feb. 17 bin 1	6.22 ± 0.36	1.88 ± 0.07	16.9 ± 1.5	9.1
2010 Feb. 17 bin 2	4.48 ± 0.26	1.87 ± 0.07	12.1 ± 1.1	6.6
2010 Feb. 17 bin 3	3.58 ± 0.29	1.73 ± 0.11	8.59 ± 1.07	15.1
2010 Feb. 17 bin 4	4.80 ± 0.43	1.53 ± 0.16	9.83 ± 1.56	8.8
2010 Feb. 18	1.53 ± 0.12	2.05 ± 0.10	4.79 ± 0.57	7.3
2010 Feb. 19	1.51 ± 0.15	2.05 ± 0.11	4.73 ± 0.66	9.6
Low state bin 1	0.094 ± 0.006	2.93 ± 0.65	0.633 ± 0.403	12.3
Low state bin 2	0.286 ± 0.021	2.48 ± 0.79	1.31 ± 0.96	10.3
Low state bin 3	0.570 ± 0.047	2.32 ± 0.10	2.26 ± 0.29	6.1
2013 Mar. 31	1.32 ± 0.14	2.29 ± 0.11	5.10 ± 0.73	7.1
2013 Apr. 11	0.593 ± 0.046	2.53 ± 0.09	2.84 ± 0.34	4.2
2013 Apr. 12 bin 1	2.33 ± 0.16	2.14 ± 0.08	7.88 ± 0.78	10.5
2013 Apr. 12 bin 2	2.13 ± 0.14	2.24 ± 0.07	7.87 ± 0.71	7.2
2013 Apr. 12 bin 3	2.25 ± 0.14	2.24 ± 0.07	8.31 ± 0.74	10.5
2013 Apr. 12 bin 4	3.5 ± 0.31	1.96 ± 0.15	10.3 ± 1.7	8.1
2013 Apr. 13 bin 1	3.32 ± 0.20	2.19 ± 0.07	11.7 ± 1.1	15.9
2013 Apr. 13 bin 2	3.93 ± 0.41	2.09 ± 0.18	12.7 ± 2.5	14.2
2013 Apr. 14 bin 1	1.06 ± 0.08	2.45 ± 0.08	4.73 ± 0.51	8.7
2013 Apr. 14 bin 2	0.689 ± 0.053	2.54 ± 0.09	3.34 ± 0.39	16.0
2013 Apr. 15 bin 1	2.36 ± 0.16	2.03 ± 0.08	7.26 ± 0.71	14.7
2013 Apr. 15 bin 2	2.54 ± 0.16	2.04 ± 0.07	7.88 ± 0.69	11.6
2013 Apr. 15 bin 3	2.92 ± 0.20	2.05 ± 0.08	9.14 ± 0.90	5.2
2013 Apr. 15 bin 4	1.30 ± 0.15	3.16 ± 0.22	11.4 ± 2.9	47
2013 Apr. 16	0.788 ± 0.066	2.45 ± 0.09	3.51 ± 0.43	11.7

Table 5.7: Table of results: Forward Folding with a power-law is applied between 251 GeV and 1 TeV. Listed is the resulting flux normalization ϕ_0, the index Γ and the integral flux $F(251 \text{ GeV} < E < 1 \text{ TeV})$ in the same energy range, as well as the χ^2 for 9 degrees of freedom. Data bins which do not cover the whole energy range or which exhibit flux variability are in bold.
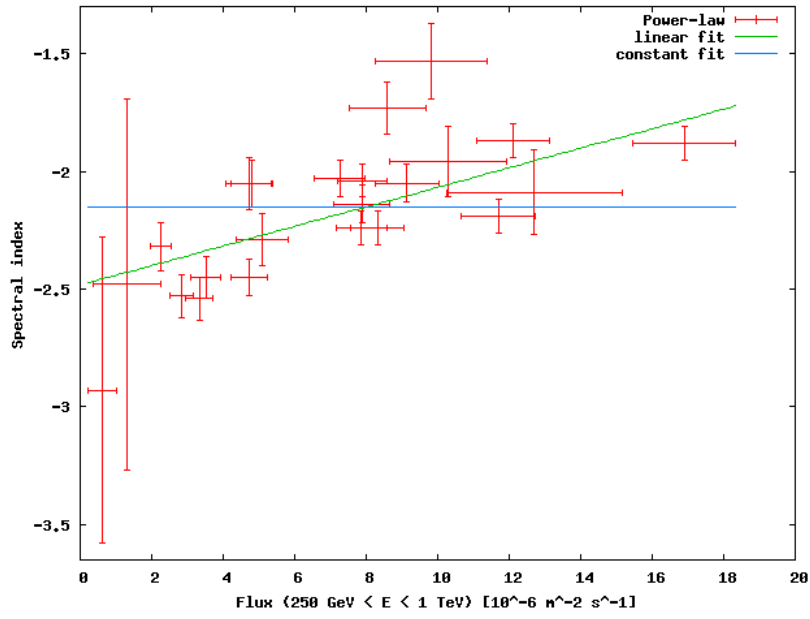
(a) All data bins
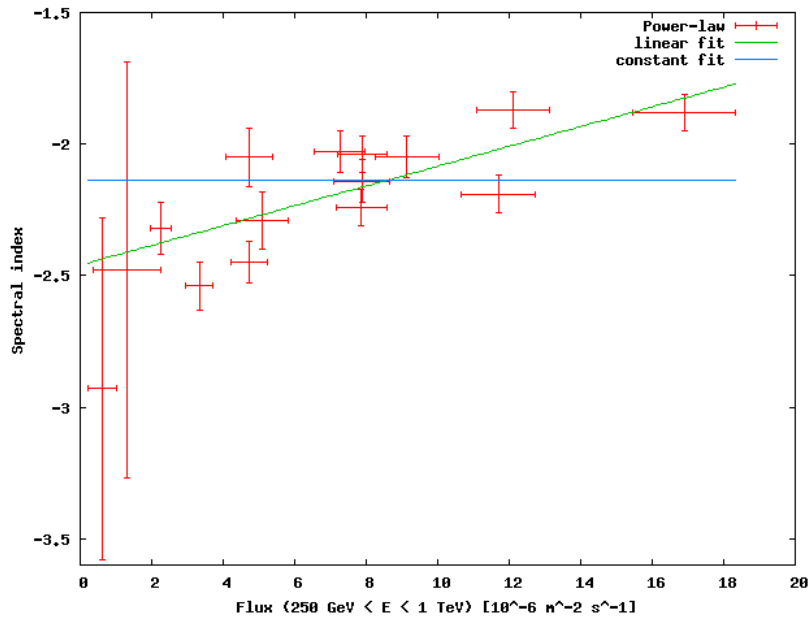
(b) Selected data bins

Figure 5.7: Dependence of spectral index Γ on flux level for all (a) and selected (b) data bins, obtained from a Forward Folding with a power-law over the energy range 251 GeV to 1 TeV. The spectral index is shown as a function of the integral flux $F(251$ GeV $< E < 1$ TeV$)$ in the energy range 251 GeV to 1 TeV. The data points are fit with a linear function (green) and a constant (blue).

First of all Forward Folding with a power-law is applied in the energy range 251 GeV to 1 TeV. This range is chosen such that the data are well represented by a power-law in all bins. The likelihood-ratio test significance of the exponential cut-off is less than 3σ on this energy range

for all data bins. Therefore, the effect of the cut-off is not significant below 1 TeV. Ideally, Forward Folding should be performed on a common energy range for all data bins. However, as much low energy data as possible should also be included for each bin. The lower limit of this range is therefore a compromise between the low energy threshold of the data bins and the desire to include as much data as possible.

The results of the Forward Folding with a power-law and the integral flux between 251 GeV and 1 TeV are shown in Table 5.7. The flux normalization at 1 TeV (ϕ_0) and the spectral index Γ are displayed with the errors from the Forward Folding. The χ^2 for the 9 degrees of freedom from the fit is given. The integral flux $F(251\,\text{GeV} < E < 1\,\text{TeV})$ together with the error from error propagation is listed.

The spectral index Γ is shown as a function of the flux between 251 GeV and 1 TeV $F(251\,\text{GeV} < E < 1\,\text{TeV})$ for all data bins in Figure 5.7 (a), and Figure 5.7 (b) shows the same plot obtained using only selected data bins (i.e., excluding those bins in bold in Table 5.7). The data points have been fit with a linear function (green line) and with a constant (blue line). The results from this fit are displayed in Table 5.8.

Sample	Power-law F-Γ All	Power-law F-Γ Selected
LINEAR fit		
Slope	0.0414 ± 0.0094	0.0376 ± 0.0092
χ^2	73	34
d.o.f.	21	13
CONSTANT fit		
χ^2	142	79
d.o.f.	22	14
TESTS		
F-test significance	3.7σ	3.3σ
Correlation coefficient r	0.72 ± 0.16	0.79 ± 0.18

Table 5.8: Table of fit results for Forward Folding with a power-law: Dependence of the spectral index Γ on the integrated flux $F(251\,\text{GeV} < E < 1\,\text{TeV})$. F-Γ data points are fit with a linear function and a constant.

A F-test has been performed using the χ^2 and degrees of freedom from the fit. The resulting significance by which the linear dependence is preferred over a constant is given. The results for the data set comprising all bins, and that comprising only the selected bin are in agreement, and show significant ($> 3\sigma$) sign of spectral hardening. Furthermore, the correla-

tion coefficient[3],

Sehr schwach

$$r_{F,\Gamma}^{\text{All}} = \frac{Cov(F,\Gamma)}{\sigma_F \sigma_\Gamma}, \tag{5.2}$$

is also calculated for both data sets and shown in Table 5.8. The coefficients are in agreement, and confirm the presence of spectral hardening with flux level.

Power-law with exponential cut-off

Bin	ϕ_0 [10^{-6}m^{-2}s^{-1}]	Index Γ	E_C [TeV]	[σ]	F [10^{-6}m^{-2}s^{-1}]	χ^2
Feb. 17 bin 1	8.95 ± 0.59	1.67 ± 0.06	3.39 ± 0.78	8.0	20.9 ± 3.1	33.5
Feb. 17 bin 2	5.42 ± 0.34	1.80 ± 0.09	3.30 ± 0.45	6.4	14.7 ± 2.4	36.3
Feb. 17 bin 3	4.05 ± 0.28	1.76 ± 0.08	3.94 ± 0.67	5.0	11.1 ± 2.2	44.2
Feb. 17 bin 4	5.68 ± 0.36	1.63 ± 0.09	3.07 ± 0.42	6.3	13.8 ± 2.4	42.2
Feb. 18	2.21 ± 0.24	1.88 ± 0.10	2.08 ± 0.36	5.5	5.56 ± 1.25	22.9
Low state 3	0.758 ± 0.072	2.15 ± 0.09	3.39 ± 0.78	3.8	2.59 ± 0.68	36.7
Apr. 11	1.16 ± 0.26	2.22 ± 0.15	1.10 ± 0.24	4.4	3.00 ± 1.02	23.0
Apr. 12 bin 1	3.06 ± 0.35	2.06 ± 0.09	2.21 ± 0.43	4.8	8.89 ± 2.13	36.8
Apr. 12 bin 2	3.06 ± 0.36	2.09 ± 0.09	1.91 ± 0.35	5.2	8.72 ± 2.03	38.2
Apr. 12 bin 3	3.02 ± 0.25	2.09 ± 0.07	2.68 ± 0.43	5.5	9.41 ± 1.81	33.4
Apr. 12 bin 4	5.38 ± 0.47	1.77 ± 0.10	2.10 ± 0.29	6.6	12.6 ± 2.4	31.9
Apr. 13 bin 1	5.44 ± 0.54	1.92 ± 0.08	1.81 ± 0.25	6.8	13.5 ± 2.5	44.1
Apr. 13 bin 2	5.00 ± 0.61	2.12 ± 0.14	2.62 ± 0.72	3.7	15.8 ± 4.8	43.1
Apr. 14 bin 1	1.38 ± 0.18	2.35 ± 0.10	2.66 ± 0.72	3.3	5.22 ± 1.65	40.9
Apr. 14 bin 2	1.12 ± 0.19	2.29 ± 0.13	1.70 ± 0.41	3.8	3.61 ± 1.16	30.2
Apr. 15 bin 1	2.70 ± 0.17	1.99 ± 0.06	4.91 ± 0.99	4.1	8.82 ± 1.93	30.8
Apr. 15 bin 2	2.78 ± 0.19	2.04 ± 0.06	4.69 ± 0.97	4.1	9.30 ± 2.09	37.6
Apr. 15 bin 3	3.65 ± 0.23	1.91 ± 0.07	4.14 ± 0.67	5.2	11.0 ± 2.1	26.7
Apr. 15 bin 4	3.32 ± 0.24	1.77 ± 0.12	3.36 ± 0.59	4.7	8.89 ± 1.93	154.2
Apr. 16	1.13 ± 0.18	2.31 ± 0.12	1.92 ± 0.49	3.6	3.83 ± 1.24	52.6

Table 5.9: Table of results for Mrk 421 between Feb. 2010 and May 2013. Forward Folding with a power-law, with an exponential cut-off, between 251 GeV and 15.8 TeV. Results with a significance of more than 3σ for an exponential cut-off are displayed. Flux normalization ϕ_0, spectral index Γ, cut-off energy E_C and flux $F(251 \text{ GeV} < E < 15.8 \text{ TeV})$ are listed with errors together with the χ^2 for 33 degrees of freedom. Data bins which do not cover the whole energy range or exhibit spectral variability are in bold.

---

[3]The correlation coefficient in the interval $-1 < r < 1$ signifies complete anti-correlation for $r = -1$, $r = 0$ means no correlation, and $r = 1$ is complete correlation.
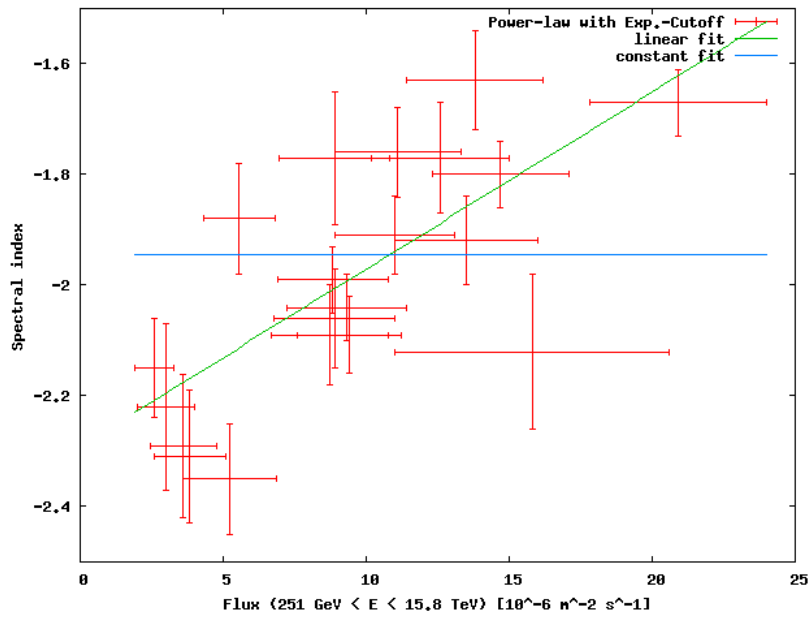
(a) All data bins
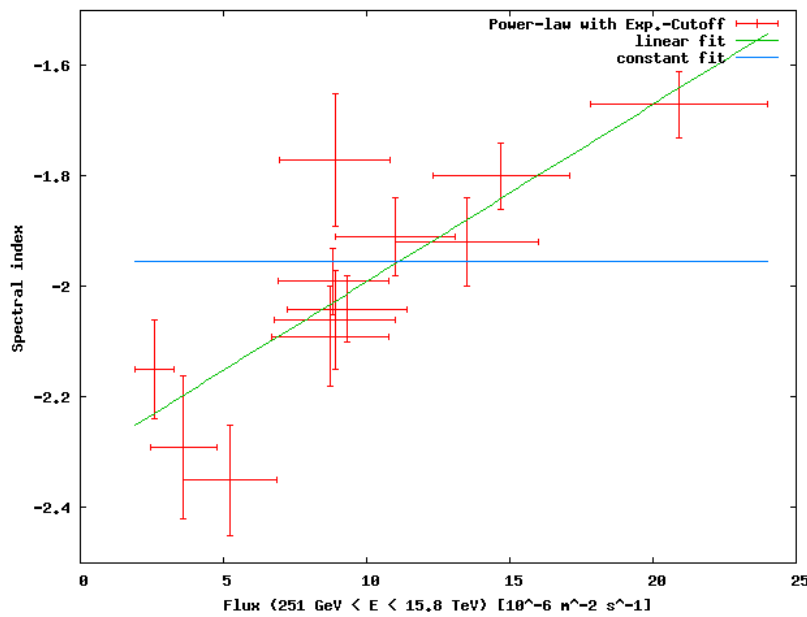
(b) Selected data bins

Figure 5.8: Dependence of the spectral index Γ on the integral flux between 251 GeV and 15.8 TeV for all data bins (a), where the exponential cut-off is favored by more than 3σ over a power-law, and selected data bins only (b). Obtained from Forward Folding with a power-law with an exponential cut-off over the energy range 251 GeV to 15.8 TeV. The data points are fit with a linear function (green) and a constant (blue).

In order to determine the cut-off energy, Forward Folding with a power-law with an exponential cut-off has to be applied. This also provides a cross-check of the spectral hardening result. Forward Folding with a power-law with an exponential cut-off is applied to the complete en-

ergy range from 251 GeV to 15.8 TeV. This includes all relevant data. The results are listed in Table 5.9. Only cut-offs detected with a significance of at greater than 3σ are shown. The flux normalization at 1 TeV ϕ_0, the spectral index Γ and the cut-off energy E_C are displayed with the errors from the Forward Folding. The χ^2 for the 33 degrees of freedom from the fit is given. The integral flux $F(251\,\mathrm{GeV} < E < 15.8\,\mathrm{TeV})$ together with the error from standard error propagation is given.

A possible dependence of the spectral index Γ on the flux level is investigated. The spectral index Γ as a function of the integral flux F (251 GeV $< E <$ 15.8 TeV) for data bins in which the exponential cut-off is favored by more than 3σ over a power-law is plotted in Figure 5.8. Part (a) displays the results for the complete data set. Part (b) shows the selected data sample in which data bins with spectral variability or which do not cover the complete energy range are excluded. The data points have been fit with a linear function (green line) and with a constant (blue line). The results from this fit are displayed in Table 5.10.

Selected bins?

Sample	Exp.Cut-off F-Γ All	Exp.Cut-off F-Γ Selected
LINEAR fit		
Slope	0.032 ± 0.006	0.032 ± 0.005
χ^2	40	13
d.o.f.	18	10
CONSTANT fit		
χ^2	105	65
d.o.f.	19	11
TESTS		
F-test significance	4.1σ	3.9σ
Correlation coefficient r	0.72 ± 0.16	0.79 ± 0.18

Table 5.10: Table of fit results for Forward Folding with a power-law with an exponential cut-off: Dependence of the spectral index Γ on the integral flux $F(251\,\mathrm{GeV} < E < 15.8\,\mathrm{TeV})$. F-Γ data points are fit with a linear function and a constant.

The F-test quantifies the significance by which the linear dependence is preferred over a constant. This significance is $> 3.9\sigma$ and is in agreement for the complete data set and the selected data sample. Additionally, the results for the correlation coefficient for all data bins and for selected data bins only are consistent, as seen in Table 5.10.

In conclusion, the results from the complete data set are consistent with the results from the selected data bins only. At the same time, the results from the Forward Folding with a power-law are consistent with the results from the Forward Folding with a power-law with an exponential cut-off. There is a correlation between the spectral index Γ and the flux level with a significance $> 3\sigma$.
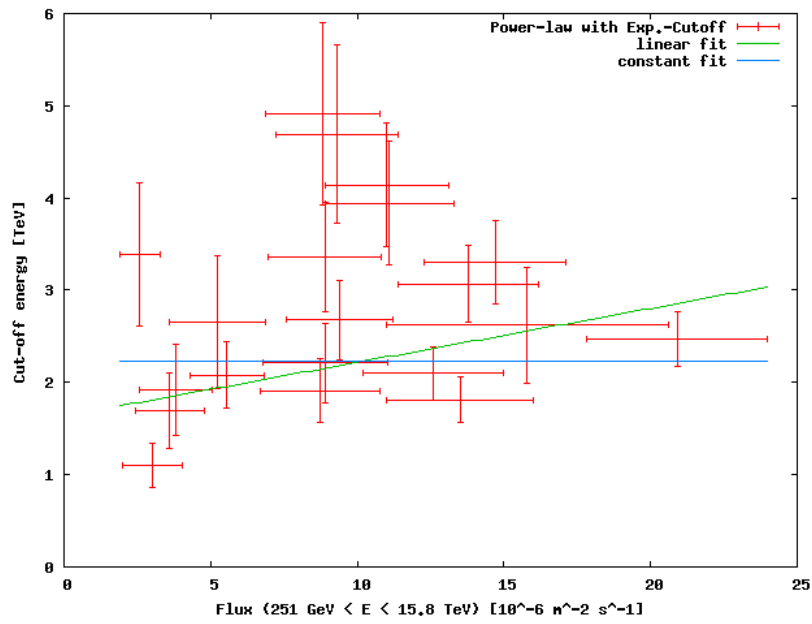
(a) All data bins
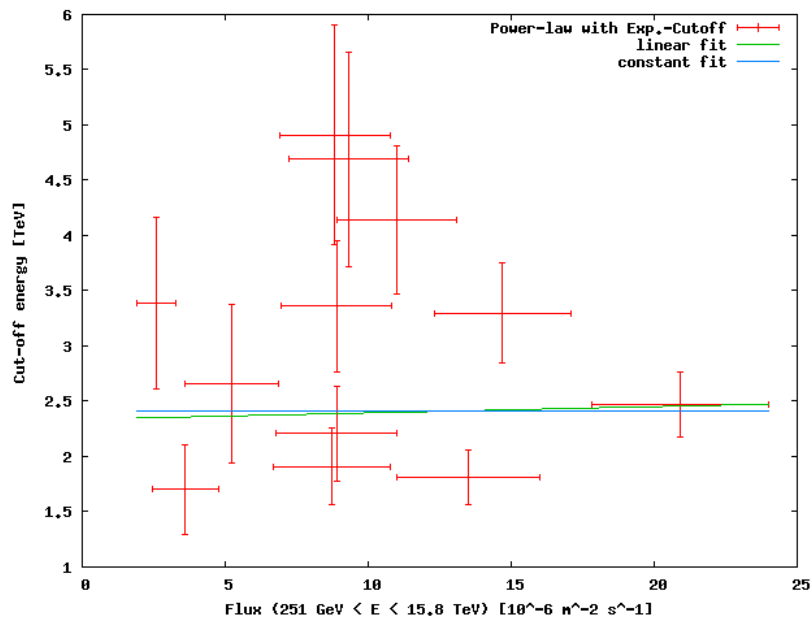
(b) Selected data bins

Figure 5.9: Dependence of the cut-off energy, E_C [TeV], on the integral flux between 251 GeV and 15.8 TeV for all data bins (a), where the exponential cut-off is favored by more than 3σ over a power-law, and selected data bins only (b). Results are obtained from Forward Folding with a power-law with an exponential cut-off over the energy range 251 GeV to 15.8 TeV. The data points are fit with a linear function (green) and a constant (blue).

In the following, the dependence of the cut-off energy on the flux level is investigated. Figure 5.9 shows the cut-off energy as a function of the the integral flux between 251 GeV and 15.8 TeV for the Forward Folding with a power-law with an exponential cut-off. Only cut-offs

detected with a significance $> 3\sigma$ are shown. The data points are fit with a linear function (green line) and with a constant (blue line). The results from this fit are displayed in Table 5.11.

Sample	Exp.Cut-off F-E_C All	Exp.Cut-off F-E_C Selected
LINEAR fit		
Slope	0.058 ± 0.032	0.057 ± 0.046
χ^2	63	38
d.o.f.	18	10
CONSTANT fit		
χ^2	75	38
d.o.f.	19	11
TESTS		
F-test significance	1.7σ	0.0σ
Correlation coefficient r	0.18 ± 0.24	-0.028 ± 0.317

Table 5.11: Table of fit results for Forward Folding with a power-law with an exponential cut-off: Dependence of cut-off energy E_C on the integrated flux $F(251 \text{ GeV} < E < 15.8 \text{ TeV})$. F-E_C data points are fitted with a linear function and a constant.

The results from the F-test do not show any dependence of the cut-off energy E_C on the flux level F. The significance is 1.7σ for the complete data sample, and 0.0σ for the selected data set. This is confirmed by the correlation coefficients, seen in Table 5.11.

Hence, no correlation of cut-off energy with the flux state could be observed. This result is consistent with the previous observations by Whipple, reported in Krennrich et al. (2002) [102], and MAGIC, Albert et al. (2007) [24].

Log-parabola spectrum

In previous observations of X-rays by Fossati et al. (2000) [67] and γ-rays by MAGIC (Albert et al., 2007 [24]) a shift of the Synchroton and Inverse Compton peak to higher energies could be observed. This can explain spectral hardening in the TeV regime, as shown in Figure 5.7 and Figure 5.8. In the case of such a shift, the flatter part of the spectrum, closer to the peak, is being measured. The underlying parameterization of the curved spectrum from the very-high-energy emission is a curved log-parabolic spectral shape (see Section 2.3, Equation 2.11). Then the peak energy of the Inverse Compton emisson in the SED is simply given by:

$$\frac{d}{dE}\left(E^2 \frac{dN}{dE}\right) = 0 \Rightarrow E_{\text{peak}} = E_0 \times e^{\frac{2-a}{2b}}. \tag{5.3}$$

A Forward Folding with a log-parabola spectrum has been applied in the following over the energy range from 251 GeV to 15.8 TeV. This is the same energy range as for the power-law with an exponential cut-off, and this includes all relevant data.
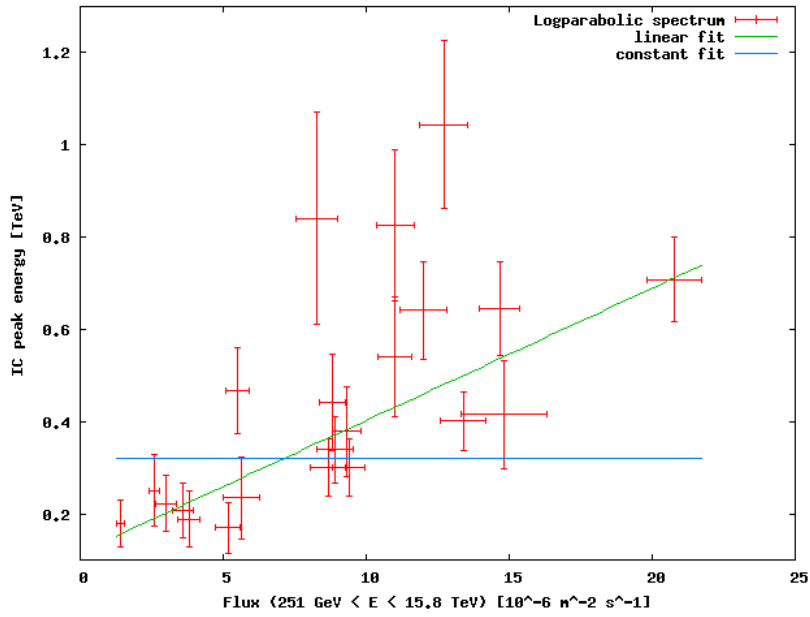
(a) All data bins
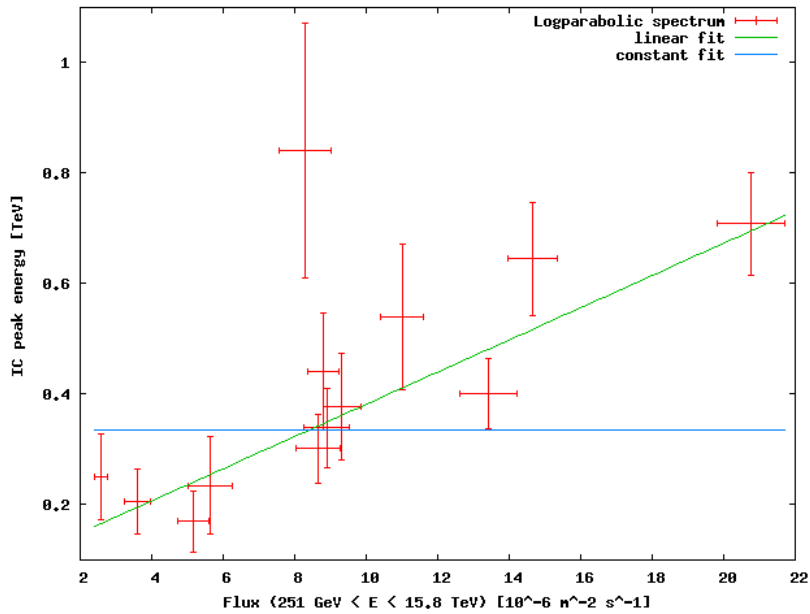
(b) Selected data bins

Figure 5.10: Dependence of the IC-peak position in TeV on the integral flux between 251 GeV and 15.8 TeV for all data bins (a) and selected data bins only (b). Results obtained from Forward Folding with a log-parabolic spectrum over the energy range 251 GeV to 15.8 TeV. The data points are fit with a linear function (green) and a constant (blue).

The results from the Forward Folding are displayed in Table 5.12. The integral flux between 251 GeV and 15.8 TeV $F(251\,\text{GeV} < E < 15.8\,\text{TeV})$ is shown together with the spectral index a, and the curvature parameter b, as well as the flux normalization at 1 TeV ϕ_0. All data bins where the log-parabolic spectral shape is preferred by more than 3σ over a power-

law are displayed. The errors on the spectral indices and the flux normalization from the fit, and the error on the flux from standard error propagation are given. Finally, the significance by which the log-parabolic spectrum is preferred over a power-law from the likelihood-ratio test is shown.

Bin	ϕ_0 [10^{-6}m^{-2}s^{-1}]	Index a	b	[σ]	F [10^{-6}m^{-2}s^{-1}]	χ^2
Feb. 17 bin 1	6.07 ± 0.17	2.20 ± 0.03	0.290 ± 0.030	7.7	20.77 ± 0.95	41.1
Feb. 17 bin 2	4.10 ± 0.12	2.21 ± 0.03	0.240 ± 0.030	6.4	14.7 ± 0.7	39.9
Feb. 17 bin 3	3.27 ± 0.12	2.09 ± 0.04	0.234 ± 0.036	5.0	11.0 ± 0.7	42.4
Feb. 17 bin 4	4.33 ± 0.14	1.97 ± 0.06	0.345 ± 0.043	6.3	12.7 ± 0.9	40.4
Feb. 18	1.38 ± 0.06	2.49 ± 0.05	0.322 ± 0.048	5.4	5.49 ± 0.40	23.8
Low state 2	0.23 ± 0.01	3.04 ± 0.07	0.302 ± 0.058	4.2	1.41 ± 0.14	25.6
Low state 3	0.565 ± 0.023	2.54 ± 0.05	0.195 ± 0.043	3.5	2.58 ± 0.19	40.9
Mar. 31	1.11 ± 0.07	2.76 ± 0.08	0.262 ± 0.069	3.0	5.63 ± 0.63	34.7
Apr. 11	0.45 ± 0.03	3.28 ± 0.09	0.426 ± 0.075	4.6	2.99 ± 0.36	20.8
Apr. 12 bin 1	1.96 ± 0.08	2.66 ± 0.05	0.305 ± 0.047	5.2	8.90 ± 0.64	29.3
Apr. 12 bin 2	1.80 ± 0.07	2.75 ± 0.05	0.313 ± 0.046	5.4	8.67 ± 0.62	34.5
Apr. 12 bin 3	2.08 ± 0.07	2.58 ± 0.04	0.242 ± 0.036	5.3	9.40 ± 0.56	35.5
Apr. 12 bin 4	3.46 ± 0.12	2.34 ± 0.05	0.382 ± 0.048	6.4	12.0 ± 0.8	31.8
Apr. 13 bin 1	3.12 ± 0.11	2.62 ± 0.04	0.339 ± 0.040	6.8	13.4 ± 0.8	44.3
Apr. 13 bin 2	3.53 ± 0.17	2.57 ± 0.07	0.324 ± 0.068	3.7	14.8 ± 1.5	39.6
Apr. 14 bin 1	0.94 ± 0.04	2.83 ± 0.06	0.234 ± 0.053	3.5	5.16 ± 0.45	37.4
Apr. 14 bin 2	0.61 ± 0.03	3.02 ± 0.07	0.323 ± 0.064	4.0	3.60 ± 0.37	28.1
Apr. 15 bin 1	2.24 ± 0.08	2.27 ± 0.03	0.165 ± 0.031	4.1	8.80 ± 0.45	30.8
Apr. 15 bin 2	2.29 ± 0.08	2.34 ± 0.04	0.175 ± 0.032	4.2	9.32 ± 0.52	34.7
Apr. 15 bin 3	2.92 ± 0.10	2.24 ± 0.03	0.195 ± 0.040	4.9	11.0 ± 0.6	36.3
Apr. 15 bin 4	2.55 ± 0.10	2.10 ± 0.08	0.289 ± 0.054	4.1	8.28 ± 0.72	131.7
Apr. 16	0.66 ± 0.04	2.95 ± 0.07	0.285 ± 0.062	3.7	3.80 ± 0.38	47.4

Table 5.12: Table of results for Mrk 421 between Feb. 2010 and May 2013. Forward Folding with a log-parabolic spectrum is applied between 251 GeV and 15.8 TeV. Results with a significance of more than 3σ for curvature are displayed. Flux normalization ϕ_0, spectral index a and curvature parrameter b, as well as the integral flux $F(251\ \text{GeV} < E < 15.8\ \text{TeV})$ are listed with errors, together with the χ^2 for the 33 degrees of freedom. Data bins which do not cover the whole energy range are shown in bold.

The dependence of the IC-peak position on the flux level can be investigated. Figure 5.10 (a) shows the IC-peak energy as a function of the flux level for all data bins in which the log-parabola spectrum is favored by more than 3σ over a power-law. The best fit with a linear

function (green line) yields a slope 0.0287 ± 0.0051, with a $\chi^2 = 41$ for 20 degrees of freedom. The fit with a constant (blue line) gives a $\chi^2 = 105$ for 21 degrees of freedom. Performing a F-test with these values leads to a significance of 4.1σ. A consistent result is obtained by the calculation of the correlation coefficient, for correlation between the IC-peak position and the flux $F(251\,\mathrm{GeV} < E < 15.8\,\mathrm{TeV})$. All data bins, in which the log-parabola spectrum is favored by more than 3σ over a power-law, are included. A cross-check is performed using only selected bins that cover the full energy range from 251 GeV to 15.8 TeV, with no spectral variability or flux variability. In Figure 5.10 (b), the IC-peak energy is displayed as a function of the flux level for selected data bins only.

The best fit with a linear function (green line) yields a slope 0.09 ± 0.05, with a $\chi^2 = 52$ for 11 degrees of freedom. The fit with a constant (blue line) gives a $\chi^2 = 13$ for 12 degrees of freedom. Performing a F-test with these values leads to a significance by which the linear dependence is preferred of 3.8σ. The correlation coefficient for the selected data bins is in full agreement with the previous result for all data bins. The results are summarized in Table 5.13.

Sample	Log-para. F-IC-peak All	Log-para. F-IC-peak Selected
LINEAR fit		
Slope	0.0287 ± 0.0051	0.09 ± 0.05
χ^2	41	52
d.o.f.	20	11
CONSTANT fit		
χ^2	105	13
d.o.f.	21	12
TESTS		
F-test significance	4.1σ	3.8σ
Correlation coefficient r	0.65 ± 0.17	0.68 ± 0.23

Table 5.13: Table of fit results for Forward Folding with a log-parabola spectrum: Dependence of the IC-peak position on the integral flux $F(251\,\mathrm{GeV} < E < 15.8\,\mathrm{TeV})$. F-IC-peak data points are fitted with a linear function and a constant.

As for the Forward Folding with a power-law with an exponential cut-off, the dependance of the spectral index as a function of the flux level can be investigated, for the log-parabolic spectrum. Looking at the spectral index a as a function of the flux level for all data bins in Figure 5.11 (a), there is moderate evidence for spectral hardening. The best fit with a linear function (green line) yields a slope -0.0345 ± 0.0102, with a $\chi^2 = 503$ for 20 degrees of freedom. The fit with a constant (blue line) gives a $\chi^2 = 795$ for 21 degrees of freedom. Performing a F-test with these values leads to a significance of 3.0σ by which the linear behaviour is preferred over a constant.
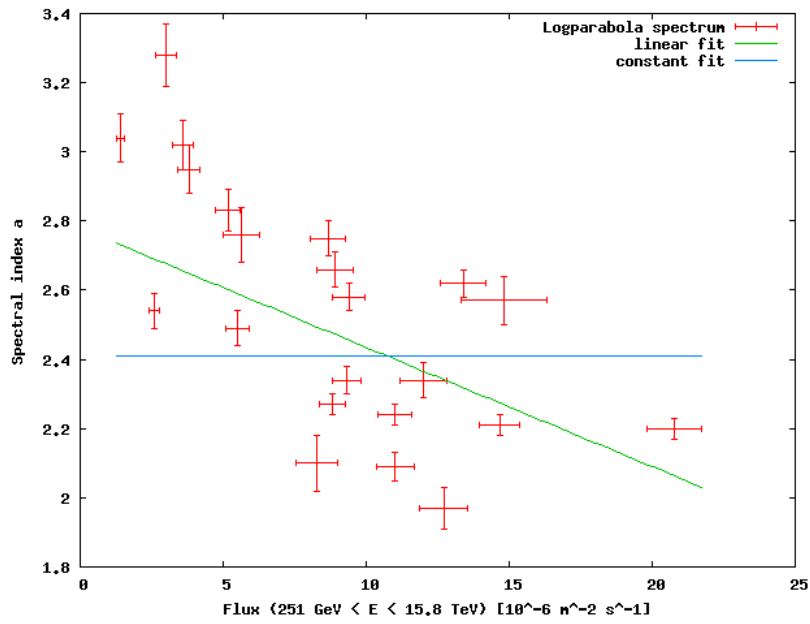
(a) All data bins
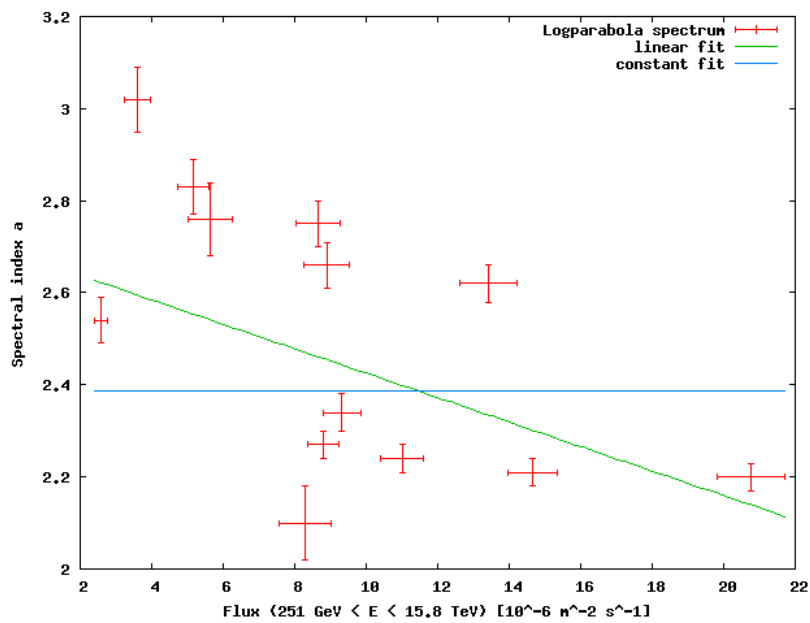
(b) Selected data bins

Figure 5.11: Dependence of the spectral index a on the integral flux between 251 GeV and 15.8 TeV for all data bins (a) and selected data bins only (b). Obtained from Forward Folding with a log-parabolic spectral shape on the energy range between 251 GeV to 15.8 TeV. Fit with a linear function (green line) and a constant (blue line)

The correlation coefficient between the spectral index a and the integral from 251 GeV to 15.8 TeV has also been calculated. The correlation coefficient, including all data bins in which the log-parabola spectrum is favored by more than 3σ over a power-law, shows a consistent sign of spectral hardening. The linear fit for the selected data sample gives a $\chi^2 = 278$ for

11 degrees of freedom, compared to a $\chi^2 = 411$ for 12 degrees of freedom, for a fit with a constant. This is shown in Figure 5.11 (b). The correlation coefficient is consistent with the result for all data bins. The results are summarized in Table 5.14.

Sample	Log-para. F-a All	Log-para. F-a Selected
LINEAR fit		
Slope	-0.0345 ± 0.0102	-0.0266 ± 0.0116
χ^2	503	278
d.o.f.	20	11
CONSTANT fit		
χ^2	795	411
d.o.f.	21	12
TESTS		
F-test significance	3.0σ	2.0σ
Correlation coefficient r	-0.68 ± 0.17	0.59 ± 0.25

Table 5.14: Table of fit results for Forward Folding with a log-parabola spectrum: Dependence of the spectral index a on the integral flux $F(251 \, \text{GeV} < E < 15.8 \, \text{TeV})$. F-a data points are fitted with a linear function and a constant.
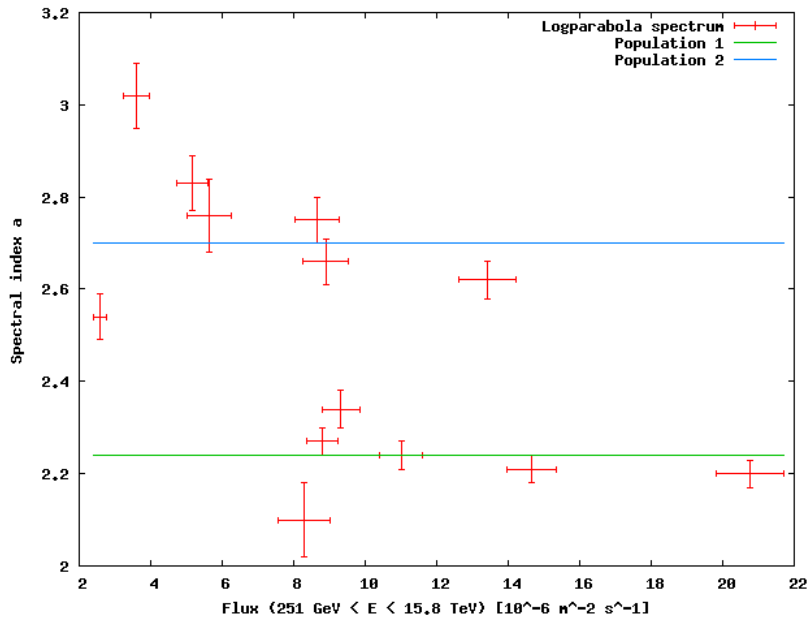
Figure 5.12: Dependence of the spectral index a on the integral flux between 251 GeV and 15.8 TeV $F(251 \, \text{GeV} < E < 15.8 \, \text{TeV})$ for selected data bins only, obtained from Forward Folding with a log-parabolic spectral shape in the energy range from 251 GeV to 15.8 TeV. In order to test if there are two distinct populations, both are fit with a constant.

Looking at the spectral index a, for selected data bins only, in Figure 5.12, it is tested if two distinct populations can be identified. The best fit with a constant for population 1 yields a $\chi^2 = 13$ for 5 degrees of freedom. For population 2 the result is $\chi^2 = 42$ for 6 degrees of freedom respectively. Also, since the result including all data bins shows a continuum, one can conclude that there is no significant distinction into two populations.
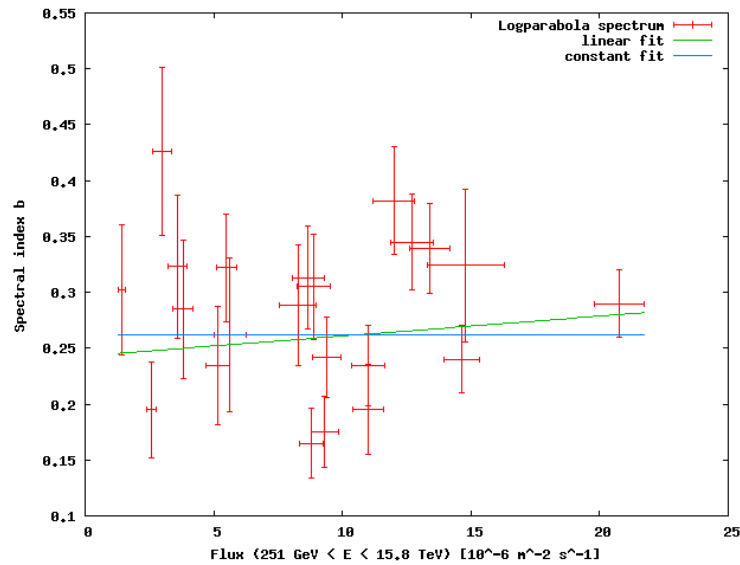
(a) All data bins
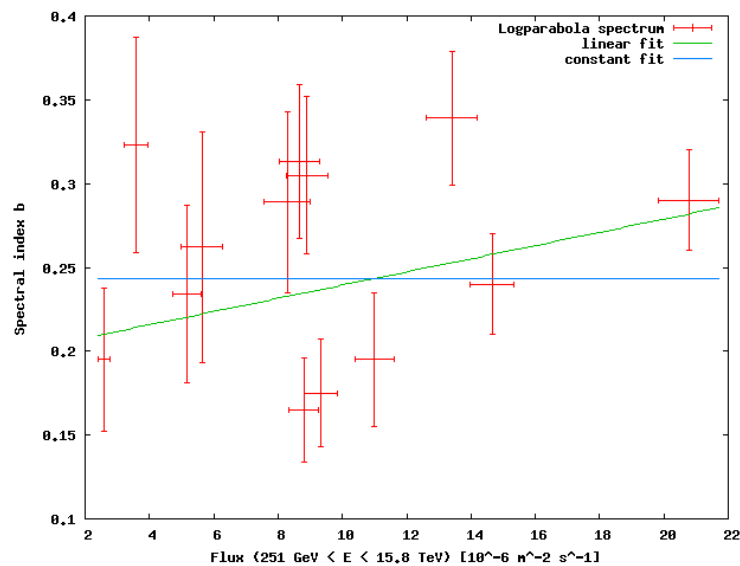
(b) Selected data bins

Figure 5.13: Dependence of the curvature parameter b on the integral flux between 251 GeV and 15.8 TeV $F(251\ \mathrm{GeV} < E < 15.8\ \mathrm{TeV})$ for all data bins (a) and selected data bins only (b), obtained from Forward Folding with a log-parabola spectrum over the energy range 251 GeV to 15.8 TeV. Fit with a constant (blue line) and a linear function (green line).

There is no evidence for any correlation of the curvature parameter b with the flux level. This can be seen in Figure 5.13 (a), which shows the fit with a linear function to all data bins in which the log-parabola spectrum is favored by more than 3σ over a power-law. The data points of the spectral index b as a function of the flux level F from the selected data set are displayed in Figure 5.13 (b). The results from the fit with a constant (blue line) and a linear function (green line) are summarized in Table 5.15.

Sample	Log-para. F-b All	Log-para. F-b Selected
LINEAR fit		
Slope	0.0018 ± 0.0030	0.0039 ± 0.0033
χ^2	50	25
d.o.f.	20	11
CONSTANT fit		
χ^2	50	28
d.o.f.	21	12
TESTS		
F-test significance	0.6σ	1.1σ
Correlation coefficient r	-0.0027 ± 0.2236	0.17 ± 0.30

Table 5.15: Table of fit results for Forward Folding with a log-parabola spectrum: Dependence of the spectral index b on the integral flux $F(251\,\text{GeV} < E < 15.8\,\text{TeV})$. Data points are fit with a linear function and a constant.

The correlation coefficient $r_{F,b} = \frac{Cov(F,b)}{\sigma_F \sigma_b}$ is consistent with $r = 0$. Furthermore, the F-test does not show a significant linear dependence of the parameter b on the flux level F. Hence, no correlation between the curvature parameter b and the flux level could be measured.

5.3 Conclusions

In conclusion, VERITAS observations of the blazar Mrk 421 from Februrary 2010 to May 2013 exhibit a $\sim 3\sigma$ significance for a correlation of the spectral index Γ to the flux state. The very-high-energy spectrum of Mrk 421 shows a harder spectral index Γ with an increasing flux level. Consistent results for this spectral hardening have been measured from Forward Folding with a power-law and a power-law with an exponential cut-off. These results were also confirmed by Forward Folding with a log-parabola spectrum. In addition, the log-parabola spectrum showed a correlation of the Inverse Compton peak energy with the integral flux. The observed spectral hardening can be explained by this shift of the Inverse Compton peak to higher energies with an increasing VHE flux level. This dependence has been observed by Albert et al. (2007) [24].

A correlation study of the VHE emission and the X-ray synchroton emission could provide a more complete picture of the acceleration mechanisms at work in the source. Mrk 421 has

shown a correlation between X-ray and VHE flux before (see e.g. Albert et al., 2007 [24]). From this, one can conclude that there is a common particle population responsible for the X-ray emission in the synchroton peak and the VHE emission in the Inverse Compton peak. Fossati et al. (2000) [67] observed a shift in the peak of the synchroton component in X-rays. They interpreted this as an injection of electrons at progressively higher energies. If the same mechanism is responsible for the shift of the IC peak at TeV energies, this could be investigated by studying a possible correlation of TeV γ-ray and X-ray emission.

Chapter 6

Summary and Outlook

Since the pioneering Whipple telescope discovered the first TeV γ-rays from the Crab Nebula in 1989 [147], VHE γ-ray astronomy has emerged to become an important field, complementary to other wavelength bands, such as X-ray and radio astronomy. The imaging atmospheric Cherenkov technique allows TeV γ-rays up to energies of 30 TeV to be observed. To this day, 147 γ-ray sources have been discovered by imaging atmospheric Cherenkov telescopes in the TeV energy range. VERITAS, a third generation IACT detecting γ-rays with energies from 85 GeV to 30 TeV, has discovered 16 and detected 47 of these objects. Of the 147 total TeV sources, 53 are extragalactic blazars, of which 26 have been detected by VERITAS.

In this thesis, the blazar Mrk 421 has been studied in detail with VERITAS. The sensitivity of VERITAS has steadily improved since its completion in 2007. After the major camera upgrade in summer 2012, VERITAS can detect a source with 1% the flux of the Crab Nebula in less than 26 hours with an improved energy threshold.

VERITAS observations of Mrk 421 from February 2010 to May 2013, comprising 106 hours of data, have been presented. In the 2010/2011 and 2011/2012 observing seasons, Mrk 421 remained in a relatively low state with 20% the flux of the Crab Nebula on average. However, it showed flux variability with a factor of 2 difference on consecutive nights.

Mrk 421 was detected with a total significance of 42.6σ in 12 hours in the 2010/2011 season and with 51.2σ in 34.3 hours in the 2011/2012 observing season. Two major flares reaching up to 8 times the flux of the Crab Nebula occured in February 2010 and April 2013. This leads to a total detection significance of 222σ in 11.5 hours of observations from February to May 2010. In the 2012/2013 observing season, Mrk 421 is detected with 331σ in 48.3 hours.

Overall, this data set allows the spectral behaviour of Mrk 421 to be investigated as a function of the flux state. Binning the data set into groups of data runs showing a similar flux level, the dependence of the spectral index and the cut-off energy on the flux state have been studied. The spectral index shows a correlation at 3σ significance level with the integral flux in the VHE range. This spectral hardening is seen when reconstructing the spectrum on a restricted energy range with a power-law. It is similarly seen when reconstructing the spectrum with a power-law with an exponential cut-off, including data over the complete sensitive energy

range. The cut-off energy reconstructed in this way does not show any dependence on the flux level. This is in accordance with previous observations by the Whipple telescope [102] and MAGIC [24].

The spectral hardening is also confirmed by a reconstruction of a log-parabola spectrum. Here, the Inverse Compton peak shows a 4σ positive correlation with the flux level. Hence, the spectral hardening can be interpreted as a shift of the flatter part of the spectrum to higher TeV energies. A shift of the Inverse Compton peak to higher energies can be accounted for by a shift of the Synchroton peak to higher energies in the case that the same particle population is responsible for both emission bumps. This can be investigated by a possible flux correlation in the future. A shift of the Synchroton peak to higher energies has been interpreted by Fossati et al. (2000) [67] in terms of a model where electrons are injected at progressively higher energies in the flaring state compared to the quiescent state.

The reconstruction of the spectrum throughout this work is done with an implementation of the Forward Folding technique. This method fully takes into account the finite energy resolution and bias of the detector. The instrument response function, which is obtained from simulations, is convolved with the parameterized spectrum and then fit to the data. This results in output values for the spectral parameters. Forward Folding is a standard method used by other VHE astronomy experiments and has been described by in detail by Albert et al. (2007) [25]. A major disadvantage of the standard correction factor method compared to Forward Folding is that an assumption of the spectral shape is made in the Monte-Carlo simulation. Forward Folding, in contrast, directly takes into account the detector response.

In this thesis, it is investigated how Forward Folding improves the reconstruction of spectral cut-offs. The performance of this method compared to the standard correction factor method is investigated in detail for VERITAS and CTA, the future TeV γ-ray observatory. A toy Monte-Carlo is set up to investigate the potential to detect exponential cut-offs in γ-ray spectra with VERITAS and CTA.

To test the significance of the presence of an exponential cut-off a likelihood-ratio test is performed. This uses the likelihood from the fits with a power-law and a power-law with a spectral cut-off. The observation time necessary for a 5σ detection is quantified as a function of the flux level and cut-off energy. It is found that VERITAS can detect an exponential cut-off (between 1 and 2 TeV) with 5σ significance for a source with Crab Nebula flux in less than ten hours. With the improved energy resolution and effective area of CTA, the required observation time is expected to decrease below one hour.

Finally, the performance of the standard correction factor method and Forward Folding is compared by means of the Mrk 421 data. The resulting significance from the Forward Folding is compared to the F-test significance using the standard correction factor method. The Forward Folding significance for an exponential cut-off exceeds the F-test significance in all cases. Hence, the Forward Folding clearly performs better in detecting an exponential cut-off

by means of a likelihood-ratio test than the standard correction factor method with a F-test using the χ^2. Forward Folding will therefore be an important tool to maximize the potential of future observation by CTA.

Bibliography

[1] A. A. Abdo et al. Fermi Observations of the Very Hard Gamma-ray Blazar PG 1553+113. *The Astrophysical Journal*, 708:1310–1320, January 2010.

[2] A. Abramowski et al. Measurement of the extragalactic background light imprint on the spectra of the brightest blazars observed with H.E.S.S. *Astronomy and Astrophysics*, 550:A4, February 2013.

[3] V. Acciari et al. Discovery of Very High Energy Gamma-ray Radiation from the BL Lac 1ES 0806+524. *The Astrophysical Journal Letters*, 690:L126–L129, January 2009.

[4] V. A. Acciari et al. VERITAS Discovery of > 200 GeV Gamma-Ray Emission from the Intermediate-Frequency-Peaked BL Lacertae Object W Comae. *The Astrophysical Journal*, 684:L73–L77, September 2008.

[5] V. A. Acciari et al. Discovery of Very High Energy Gamma Rays from PKS 1424+240 and Multiwavelength Constraints on Its Redshift. *The Astrophysical Journal Letters*, 708:L100–L106, January 2010.

[6] V. A. Acciari et al. The Discovery of γ-Ray Emission from the Blazar RGB J0710+591. *The Astrophysical Journal Letters*, 715:L49–L55, May 2010.

[7] V. A. Acciari et al. Spectral Energy Distribution of Markarian 501: Quiescent State Versus Extreme Outburst. *The Astrophysical Journal*, 729:2, March 2011.

[8] B. S. Acharya et al. Introducing the CTA concept. *Astroparticle Physics*, 43:3–18, March 2013.

[9] F. Aharonian et al. Evidence for TeV gamma-ray emission from Cassiopeia A. *Astronomy and Astrophysics*, 370:112–120, 2001.

[10] F. Aharonian et al. Variations of the TeV energy spectrum at different flux levels of Mkn 421 observed with the HEGRA system of Cherenkov telescopes. *Astronomy and Astrophysics*, 393:89–99, October 2002.

[11] F. Aharonian et al. Discovery of VHE gamma rays from PKS 2005-489. *Astronomy and Astrophysics*, 436:L17–L20, June 2005.

[12] F. Aharonian et al. A low level of extragalactic background light as revealed by γ-rays from blazars. *Nature*, 440:1018–1021, April 2006.

[13] F. Aharonian et al. Discovery of very high energy γ-ray emission from the BL Lacertae object H 2356-309 with the HESS Cherenkov telescopes. *Astronomy and Astrophysics*, 455:461–466, August 2006.

[14] F. Aharonian et al. Evidence for VHE γ-ray emission from the distant BL Lac PG 1553+113. *Astronomy and Astrophysics*, 448:L19–L23, March 2006.

[15] F. Aharonian et al. Observations of the Crab Nebula with H.E.S.S. *Astronomy and Astrophysics*, 457:899–915, 2006.

[16] F. Aharonian et al. An Exceptional Very High Energy Gamma-Ray Flare of PKS 2155-304. *The Astrophysical Journal*, 664:L71–L74, August 2007.

[17] F. Aharonian et al. Discovery of VHE γ-rays from the distant BL Lacertae 1ES 0347-121. *Astronomy and Astrophysics*, 473:L25–L28, October 2007.

[18] F. Aharonian et al. New constraints on the mid-IR EBL from the HESS discovery of VHE γ-rays from 1ES 0229+200. *Astronomy and Astrophysics*, 475:L9–L13, November 2007.

[19] F. Aharonian et al. Discovery of VHE gamma-rays from the high-frequency-peaked BL Lacertae object RGB J0152+017. *Astronomy and Astrophysics*, 481:L103–L107, April 2008.

[20] F. A. Aharonian, W. Hofmann, A. K. Konopelko, and H. J. Völk. The potential of ground based arrays of imaging atmospheric Cherenkov telescopes. I. Determination of shower parameters. *Astroparticle Physics*, 6:343–368, March 1997.

[21] J. Albert et al. Discovery of Very High Energy Gamma Rays from 1ES 1218+30.4. *The Astrophysical Journal*, 642:L119–L122, May 2006.

[22] J. Albert et al. Discovery of Very High Energy γ-Rays from Markarian 180 Triggered by an Optical Outburst. *The Astrophysical Journal*, 648:L105–L108, September 2006.

[23] J. Albert et al. Discovery of Very High Energy γ-Rays from 1ES 1011+496 at z = 0.212. *The Astrophysical Journal*, 667:L21–L24, September 2007.

[24] J. Albert et al. Observations of Markarian 421 with the MAGIC Telescope. *The Astrophysical Journal*, 663:125–138, July 2007.

[25] J. Albert et al. Unfolding of differential energy spectra in the MAGIC experiment. *Nucl.Instrum.Meth.*, A583:494–506, 2007.

[26] J. Aleksić et al. MAGIC Discovery of Very High Energy Emission from the FSRQ PKS 1222+21. *The Astrophysical Journal Letters*, 730:L8, March 2011.

[27] J. Aleksić et al. Discovery of VHE γ-ray emission from the BL Lacertae object B3 2247+381 with the MAGIC telescopes. *Astronomy and Astrophysics*, 539:A118, March 2012.

[28] J. Aleksić et al. Discovery of VHE γ-rays from the blazar 1ES 1215+303 with the MAGIC telescopes and simultaneous multi-wavelength observations. *Astronomy and Astrophysics*, 544:A142, August 2012.

[29] J. Aleksic et al. Performance of the MAGIC stereo system obtained with Crab Nebula data. *Astropart.Phys.*, 35:435–448, 2012.

[30] E. Aliu et al. Discovery of High-energy and Very High Energy γ-Ray Emission from the Blazar RBS 0413. *The Astrophysical Journal*, 750:94, May 2012.

[31] E. Aliu et al. A Search for Enhanced Very High Energy Gamma-Ray Emission from the 2013 March Crab Nebula Flare. *The Astrophysical Journal Letters*, 781:L11, January 2014.

[32] H. Anderhub et al. Discovery of very High Energy γ-Rays from the Blazar S5 0716+714. *The Astrophysical Journal Letters*, 704:L129–L133, October 2009.

[33] S. Archambault et al. Discovery of a New TeV Gamma-Ray Source: VER J0521+211. *The Astrophysical Journal*, 776:69, October 2013.

[34] R. Atkins et al. Status of the Milagro Gamma Ray Observatory. *ArXiv Astrophysics e-prints*, June 1999.

[35] W. B. Atwood et al. The Large Area Telescope on the Fermi Gamma-Ray Space Telescope Mission. *The Astrophysical Journal*, 697:1071–1102, June 2009.

[36] W. I. Axford, E. Leer, and G. Skadron. The acceleration of cosmic rays by shock waves. *International Cosmic Ray Conference*, 11:132–137, 1977.

[37] Anna Barnacka et al. Performance of the Cherenkov Telescope Array at energies above 10 TeV. *ArXiv e-prints*, July 2013.

[38] A. Barrau et al. The CAT imaging telescope for very-high-energy gamma-ray astronomy. *Nuclear Instruments and Methods in Physics Research A*, 416:278–292, October 1998.

[39] V. Beckmann and C. R. Shrader. *Active Galactic Nuclei*. Wiley-VCH, August 2012.

[40] A. R. Bell. The acceleration of cosmic rays in shock fronts. I. *Monthly Notices of the Royal Astronomical Society*, 182:147–156, January 1978.

[41] E. G. Berezhko and D. C. Ellison. A Simple Model of Nonlinear Diffusive Shock Acceleration. *The Astrophysical Journal*, 526:385–399, November 1999.

[42] D. Berge, S. Funk, and J. Hinton. Background modelling in very-high-energy γ-ray astronomy. *Astronomy and Astrophysics*, 466:1219–1229, May 2007.

[43] K. Berger. Overview of the results from extra-galactic observations with the MAGIC telescopes. *International Cosmic Ray Conference*, 8:167, 2011.

[44] K. Bernlöhr. Simulation of imaging atmospheric Cherenkov telescopes with CORSIKA and sim_ telarray. *Astroparticle Physics*, 30:149–158, October 2008.

[45] R. Blandford and D. Eichler. Particle acceleration at astrophysical shocks: A theory of cosmic ray origin. *Physics Reports*, 154:1–75, October 1987.

[46] R. D. Blandford and A. Königl. Relativistic jets as compact radio sources. *The Astrophysical Journal*, 232:34–48, August 1979.

[47] R. D. Blandford and J. P. Ostriker. Particle acceleration by astrophysical shocks. *The Astrophysical Journal Letters*, 221:L29–L32, April 1978.

[48] R. D. Blandford and M. J. Rees. Some comments on radiation mechanisms in Lacertids. In A. M. Wolfe, editor, *BL Lac Objects*, pages 328–341, 1978.

[49] R. D. Blandford and R. L. Znajek. Electromagnetic extraction of energy from Kerr black holes. *Monthly Notices of the Royal Astronomical Society*, 179:433–456, May 1977.

[50] V. Blobel. *Unfolding methods in high energy physics experiments*. DESY, 1984.

[51] V. Blobel. An Unfolding Method for High Energy Physics Experiments. *ArXiv High Energy Physics - Experiment e-prints*, August 2002.

[52] M. Catanese et al. Discovery of Gamma-Ray Emission above 350 GeV from the BL Lacertae Object 1ES 2344+514. *The Astrophysical Journal*, 501:616, July 1998.

[53] P. M. Chadwick, K. Lyons, T. J. L. McComb, K. J. Orford, J. L. Osborne, S. M. Rayner, S. E. Shaw, K. E. Turver, and G. J. Wieczorek. PKS 2155-304 - a source of VHE γ-rays. *Astroparticle Physics*, 11:145–148, June 1999.

[54] P.A. Cherenkov. *Doklady Akademii Nauk SSSR*, 2:451, 1934.

[55] G.D. Cowan. *Statistical Data Analysis*. Oxford University Press, 1998.

[56] H. D. Curtis. Descriptions of 762 Nebulae and Clusters Photographed with the Crossley Reflector. *Publications of Lick Observatory*, 13:9–42, 1918.

[57] A. Daum et al. First results on the performance of the HEGRA IACT array. *Astroparticle Physics*, 8:1–11, December 1997.

[58] J. M. Davies and E. S. Cotton. Design of the quartermaster solar furnace. *Solar Energy*, 1:16–22, April 1957.

[59] B. de Lotto et al. The MAGIC Telescopes: Performance, Results and Future Perspectives. *12th International Conference on Topics in Astroparticle and Underground Physics*, 2011.

[60] C. D. Dermer, R. Schlickeiser, and A. Mastichiadis. High-energy gamma radiation from extragalactic radio sources. *Astronomy and Astrophysics*, 256:L27–L30, March 1992.

[61] M. Errando, R. Bock, D. Kranich, E. Lorenz, P. Majumdar, M. Mariotti, D. Mazin, E. Prandini, F. Tavecchio, M. Teshima, and R. Wagner. Discovery of very high energy gamma-rays from the flat spectrum radio quasar 3C 279 with the MAGIC telescope. In F. A. Aharonian, W. Hofmann, and F. Rieger, editors, *American Institute of Physics Conference Series*, volume 1085 of *American Institute of Physics Conference Series*, pages 423–426, December 2008.

[62] M. Errando for the VERITAS Collaboration. Discovery and identification of two gamma-ray blazars at low galactic latitude with VERITAS. *Fermi Symposium Proceedings*, November 2011.

[63] B. L. Fanaroff and J. M. Riley. The morphology of extragalactic radio sources of high and low luminosity. *Monthly Notes of the Royal Astronomical Society*, 167:31P–36P, May 1974.

[64] D. J. Fegan. TOPICAL REVIEW: γ/hadron separation at TeV energies. *Journal of Physics G Nuclear Physics*, 23:1013–1060, September 1997.

[65] E. Fermi. On the Origin of the Cosmic Radiation. *Physical Review*, 75:1169–1174, April 1949.

[66] V. P. Fomin, A. A. Stepanian, R. C. Lamb, D. A. Lewis, M. Punch, and T. C. Weekes. New methods of atmospheric Cherenkov imaging for gamma-ray astronomy. I. The false source method. *Astroparticle Physics*, 2:137–150, May 1994.

[67] G. Fossati, A. Celotti, M. Chiaberge, Y. H. Zhang, L. Chiappetti, G. Ghisellini, L. Maraschi, F. Tavecchio, E. Pian, and A. Treves. X-Ray Emission of Markarian 421: New Clues from Its Spectral Evolution. II. Spectral Analysis and Physical Constraints. *The Astrophysical Journal*, 541:166–179, September 2000.

[68] G. Fossati, L. Maraschi, A. Celotti, A. Comastri, and G. Ghisellini. A unifying view of the spectral energy distributions of blazars. *Monthly Notices of the Royal Astronomical Society*, 299:433–448, September 1998.

[69] J. A. Gaidos et al. Extremely rapid bursts of TeV photons from the active galaxy Markarian 421. *Nature*, 383:319–320, September 1996.

[70] N. Galante and for the VERITAS Collaboration. VERITAS observation of Markarian 421 flaring activity. *ICRC Proc.*, September 2011.

[71] B. Giebels, G. Dubus, and B. Khélifi. Unveiling the X-ray/TeV engine in Mkn 421. *Astronomy and Astrophysics*, 462:29–41, January 2007.

[72] V. L. Ginzburg and S. I. Syrovatskii. Cosmic Magnetobremsstrahlung (synchrotron Radiation). *Annual Review of Astronomy and Astrophysics*, 3:297, 1965.

[73] M. M. González. Observing the universe at TeV energies with the HAWC observatory. *International Cosmic Ray Conference*, 3:1563–1566, 2008.

[74] H. E. S. S. Collaboration, A. Abramowski, et al. H.E.S.S and Fermi-LAT discovery of gamma rays from the blazar 1ES 1312-423. *Monthly Notes of the Royal Astronomical Society*, June 2013.

[75] H. E. S. S. Collaboration, A. Abramowski, et al. H.E.S.S. observations of the Crab during its March 2013 GeV gamma-ray flare. *Astronomy and Astrophysics*, 562:L4, February 2014.

[76] J. Hall, V. V. Vassiliev, D. B. Kieda, J. Moses, T. Nagai, and J. Smith. Veritas CFDs. *International Cosmic Ray Conference*, 5:2851, July 2003.

[77] D. Hanna, A. McCann, M. McCutcheon, and L. Nikkinen. An LED-based flasher system for VERITAS. *Nuclear Instruments and Methods in Physics Research A*, 612:278–287, January 2010.

[78] E. Hays. VERITAS Data Acquisition. *International Cosmic Ray Conference*, 3:1543–1546, 2008.

[79] D. Heck, J. Knapp, J. N. Capdevielle, G. Schatz, and T. Thouw. *CORSIKA: a Monte Carlo code to simulate extensive air showers.* February 1998.

[80] H.E.S.S. Collaboration, A. Abramowski, et al. HESS J1943+213: a candidate extreme BL Lacertae object. *Astronomy and Astrophysics*, 529:A49, May 2011.

[81] H.E.S.S. Collaboration, A. Abramowski, et al. Discovery of hard-spectrum γ-ray emission from the BL Lacertae object 1ES 0414+009. *Astronomy and Astrophysics*, 538:A103, February 2012.

[82] H.E.S.S. Collaboration, A. Abramowski, et al. Discovery of VHE γ-ray emission and multi-wavelength observations of the BL Lacertae object 1RXS J101015.9-311909. *Astronomy and Astrophysics*, 542:A94, June 2012.

[83] H.E.S.S. Collaboration, A. Abramowski, et al. Discovery of high and very high-energy emission from the BL Lacertae object SHBL J001355.9-185406. *Astronomy and Astrophysics*, 554:A72, June 2013.

[84] H.E.S.S. Collaboration, A. Abramowski, et al. Discovery of TeV γ-ray emission from PKS 0447-439 and derivation of an upper limit on its redshift. *Astronomy and Astrophysics*, 552:A118, April 2013.

[85] H.E.S.S. Collaboration, A. Abramowski, et al. Discovery of very high energy γ-ray emission from the BL Lacertae object PKS 0301-243 with H.E.S.S. *Astronomy and Astrophysics*, 559:A136, November 2013.

[86] H.E.S.S. Collaboration, Y. Becherini, C. Boisson, and M. Cerruti. Discovery of the most distant BL Lacertae at very high energies with H.E.S.S. *5th International Symposium on High-Energy Gamma-Ray Astronomy*, 2012.

[87] D. Hildebrand, S. Lombardi, P. Colin, J. Sitarek, F. Zandanel, F. Prada, for the MAGIC Collaboration, C. Pfrommer, and A. Pinzke. MAGIC detection of VHE Gamma-ray emission from NGC 1275 and IC 310. *International Cosmic Ray Conference*, October 2011.

[88] A. M. Hillas. Cerenkov light images of EAS produced by primary gamma. *International Cosmic Ray Conference*, 3:445–448, August 1985.

[89] J. Hinton. Ground-based gamma-ray astronomy with Cherenkov telescopes. *New Journal of Physics*, 11(5):055005, May 2009.

[90] J. A. Hinton and W. Hofmann. Teraelectronvolt Astronomy. *Annual Review of Astronomy and Astrophysics*, 47:523–565, September 2009.

[91] W. Hofmann, I. Jung, A. Konopelko, H. Krawczynski, H. Lampeitl, and G. Pühlhofer. Comparison of techniques to reconstruct VHE gamma-ray showers from multiple stereoscopic Cherenkov images. *Astroparticle Physics*, 12:135–143, November 1999.

[92] J. Holder. Exploiting VERITAS Timing Information. *International Cosmic Ray Conference*, 5:383, 2005.

[93] J. Holder et al. The first VERITAS telescope. *Astroparticle Physics*, 25:391–401, July 2006.

[94] J. Holder et al. VERITAS: Status and Highlights. *International Cosmic Ray Conference*, November 2011.

[95] D. Horan et al. Detection of the BL Lacertae Object H1426+428 at TeV Gamma-Ray Energies. *The Astrophysical Journal*, 571:753–762, June 2002.

[96] Frederick E James. *Statistical Methods in Experimental Physics; 2nd ed.* World Scientific, Singapore, 2006.

[97] E. E. Khachikian and D. W. Weedman. A spectroscopic study of luminous galactic nuclei. *Astrofizika*, 7:389–406, 1971.

[98] E. Y. Khachikian and D. W. Weedman. An atlas of Seyfert galaxies. *The Astrophysical Journal*, 192:581–589, September 1974.

[99] J. G. Kirk and P. Duffy. TOPICAL REVIEW: Particle acceleration and relativistic shocks. *Journal of Physics G Nuclear Physics*, 25:163, August 1999.

[100] J. G. Kirk, P. Duffy, and Y. A. Gallant. Stochastic particle acceleration at shocks in the presence of braided magnetic fields. *Astronomy and Astrophysics*, 314:1010–1016, October 1996.

[101] A. Kohnle et al. Stereoscopic imaging of air showers with the first two HEGRA Cherenkov telescopes. *Astroparticle Physics*, 5:119–131, August 1996.

[102] F. Krennrich, I. Bond, et al. Discovery of Spectral Variability of Markarian 421 at TeV Energies. *The Astrophysical Journal*, 575:L9–L13, August 2002.

[103] G. F. Krymskii. A regular mechanism for the acceleration of charged particles on the front of a shock wave. *Akademiia Nauk SSSR Doklady*, 234:1306–1308, June 1977.

[104] T.-P. Li and Y.-Q. Ma. Analysis methods for results in gamma-ray astronomy. *The Astrophysical Journal*, 272:317–324, 1983.

[105] M. L. Lister et al. MOJAVE: Monitoring of Jets in Active Galactic Nuclei with VLBA Experiments. VI. Kinematics Analysis of a Complete Sample of Blazar Jets. *The Astronomical Journal*, 138:1874–1892, December 2009.

[106] M.S. Longair. *High-energy astrophysics*. Cambridge University Press, 2011.

[107] R. V. E. Lovelace and M. M. Romanova. Relativistic Poynting Jets from Accretion Disks. *The Astrophysical Journal*, 596:L159–L162, October 2003.

[108] MAGIC Collaboration, J. Aleksić, et al. Discovery of very high energy gamma-ray emission from the blazar 1ES 1727+502 with the MAGIC Telescopes. *Astronomy and Astrophysics*, February 2013.

[109] L. Maraschi, G. Ghisellini, and A. Celotti. A jet model for the gamma-ray emitting blazar 3C 279. *The Astrophysical Journal*, 397:L5–L9, 1992.

[110] L. Maraschi, G. Ghisellini, and A. Celotti. A jet model for the gamma-ray emitting blazar 3C 279. *The Astrophysical Journal Letters*, 397:L5–L9, September 1992.

[111] B. Margon and J. P. Ostriker. The Luminosity Function of Galactic X-Ray Sources - a Cutoff and a "standard Candle"? *The Astrophysical Journal*, 186:91–96, November 1973.

[112] A. P. Marscher and W. K. Gear. Models for high-frequency radio outbursts in extra-galactic sources, with application to the early 1983 millimeter-to-infrared flare of 3C 273. *The Astrophysical Journal*, 298:114–127, November 1985.

[113] E. Massaro, M. Perri, P. Giommi, and R. Nesci. Log- parabolic spectra and particle acceleration in the BL Lac object Mkn 421: Spectral analysis of the complete BeppoSAX wide band x-ray data set. *Astronomy and Astrophysics*, 413:489–503, 2004.

[114] E. Massaro, A. Tramacere, M. Perri, P. Giommi, and G. Tosti. Log-parabolic spectra and particle acceleration in blazars. 3. SSC emission in the TeV band from Mkn 501. *Astronomy and Astrophysics*, 2005.

[115] A. McCann, D. Hanna, J. Kildea, and M. McCutcheon. A new mirror alignment system for the VERITAS telescopes. *Astroparticle Physics*, 32:325–329, January 2010.

[116] A. Mücke, R. J. Protheroe, R. Engel, J. P. Rachen, and T. Stanev. BL Lac objects in the synchrotron proton blazar model. *Astroparticle Physics*, 18:593–613, March 2003.

[117] C. Müller et al. Dual-frequency VLBI study of Centaurus A on sub-parsec scales. The highest-resolution view of an extragalactic jet. *Astronomy and Astrophysics*, 530:L11, June 2011.

[118] Y. I. Neshpor, N. N. Chalenko, A. A. Stepanian, O. R. Kalekin, N. A. Jogolev, V. P. Fomin, and V. G. Shitov. BL Lac: A New Ultrahigh-Energy Gamma-Ray Source. *Astronomy Reports*, 45:249–254, April 2001.

[119] Y. I. Neshpor, A. A. Stepanyan, O. P. Kalekin, V. P. Fomin, N. N. Chalenko, and V. G. Shitov. Blazar 3C 66A: Another extragalactic source of ultra-high-energy gamma-ray photons. *Astronomy Letters*, 24:134–138, March 1998.

[120] T. Nishiyama. Detection of a new TeV gamma-ray source of BL Lac object 1ES 1959+650. *International Cosmic Ray Conference*, 3:370, August 1999.

[121] P. Padovani and P. Giommi. The connection between x-ray- and radio-selected BL Lacertae objects. *The Astrophysical Journal*, 444:567–581, May 1995.

[122] B. G. Piner, A. B. Pushkarev, Y. Y. Kovalev, C. J. Marvin, J. G. Arenson, P. Charlot, A. L. Fey, A. Collioud, and P. A. Voitsik. Relativistic Jets in the Radio Reference Frame Image Database. II. Blazar Jet Accelerations from the First 10 Years of Data (1994-2003). *The Astrophysical Journal*, 758:84, October 2012.

[123] Heike Prokoph. *Observations and modeling of the active galactic nucleus B2 1215+30 together with performance studies of the ground-based gamma-ray observatories VERITAS and CTA*. PhD thesis, 2013.

[124] M. Punch et al. Detection of TeV photons from the active galaxy Markarian 421. *Nature*, 358:477, August 1992.

[125] J. Quinn et al. Detection of Gamma Rays with E > 300 GeV from Markarian 501. *The Astrophysical Journal Letters*, 456:L83, January 1996.

[126] P. F. Rebillot, J. H. Buckley, P. Dowkontt, and K. Kosack. The VERITAS Flash ADC Electronics System. *International Cosmic Ray Conference*, 5:2827, July 2003.

[127] M. J. Rees. Studies in radio source structure-I. A relativistically expanding model for variable quasi-stellar radio sources. *Monthly Notes of the Royal Astronomical Society*, 135:345, 1967.

[128] F. M. Rieger, V. Bosch-Ramon, and P. Duffy. Fermi acceleration in astrophysical jets. *Astrophysics and Space Science*, 309:119–125, June 2007.

[129] F. M. Rieger and P. Duffy. A Microscopic Analysis of Shear Acceleration. *The Astrophysical Journal*, 652:1044–1049, December 2006.

[130] E. Roache, R. Irvin, J. S. Perkins, and et al. Mirror Facets for the VERITAS Telescopes. *International Cosmic Ray Conference*, 3:1397–1400, 2008.

[131] F. W. Samuelson, S. D. Biller, et al. The TeV Spectrum of Markarian 501. *The Astrophysical Journal*, 501:L17, July 1998.

[132] W. L. W. Sargent, P. J. Young, C. R. Lynds, A. Boksenberg, K. Shortridge, and F. D. A. Hartwick. Dynamical evidence for a central mass concentration in the galaxy M87. *The Astrophysical Journal*, 221:731–744, May 1978.

[133] F. Schmidt. Corsika shower images. *http://www.ast.leeds.ac.uk/ fs/showerimages.html*, 2005. [Online; accessed 14 March 2014].

[134] R. Schopper, H. Lesch, and G. T. Birk. Magnetic reconnection and particle acceleration in active galactic nuclei. *Astronomy and Astrophysics*, 335:26–32, July 1998.

[135] A. J. Smith and HAWC Collaboration. HAWC: A next generation all-sky gamma-ray telescope. *Journal of Physics Conference Series*, 60:131–134, March 2007.

[136] J. T. Stocke, C. W. Danforth, and E. S. Perlman. Broad Lyα Emission from Three Nearby BL Lacertae Objects. *The Astrophysical Journal*, 732:113, May 2011.

[137] G. Superina, W. Benbow, T. Boutelier, and et al. Discovery of VHE gamma-rays from the BL Lac object PKS 0548-322 with H.E.S.S. *International Cosmic Ray Conference*, 3:913–916, 2008.

[138] I.E. Tamm and I.M. Frank. *Doklady Akademii Nauk SSSR*, 14:109, 1937.

[139] A.N. Tikhonov and V.Ja. Arsenin. Methods of solution of ill-posed problems. 1937.

[140] Diego F. Torres and Luis A. Anchordoqui. Astrophysical origins of ultrahigh energy cosmic rays. *Rept.Prog.Phys.*, 67:1663–1730, 2004.

[141] A. Tramacere, E. Massaro, and A.M. Taylor. Stochastic Acceleration and the Evolution of Spectral Distributions in SSC Sources: A Self Consistent Modeling of Blazars' Flares. *The Astrophysical Journal*, 739:66, 2011.

[142] C. M. Urry. Multiwavelength properties of blazars. *Advances in Space Research*, 21:89–100, 1998.

[143] C. Megan Urry and Paolo Padovani. Unified schemes for radio-loud active galactic nuclei. *Publ.Astron.Soc.Pac.*, 107:803, 1995.

[144] E. Valtaoja, H. Terasranta, S. Urpo, N. S. Nesterov, M. Lainela, and M. Valtonen. Five Years Monitoring of Extragalactic Radio Sources - Part Four - Variability Statistics and the Unified Models for AGN / Active Galactic Nuclei. *Astronomy and Astrophysics*, 254:80, February 1992.

[145] S. J. Wagner and H.E.S.S. Collaboration. Detection of VHE Gamma-ray Emission from a Type 1 Quasar. In *American Astronomical Society, HEAD meeting #11, #27.06*, volume 11 of *AAS/High Energy Astrophysics Division*, page #27.06, February 2010.

[146] S. Wakely and D. Horan. Tevcat - an online gamma-ray catalog. *http://tevcat.uchicago.edu*. [Online; accessed 10 April 2014].

[147] T. C. Weekes, M. F. Cawley, D. J. Fegan, K. G. Gibbs, A. M. Hillas, P. W. Kowk, R. C. Lamb, D. A. Lewis, D. Macomb, N. A. Porter, P. T. Reynolds, and G. Vacanti. Observation of TeV gamma rays from the Crab nebula using the atmospheric Cerenkov imaging technique. *The Astrophysical Journal*, 342:379–395, July 1989.

[148] A. Weinstein. The VERITAS Trigger System. *International Cosmic Ray Conference*, 3:1539–1542, 2008.

[149] Wystan Benbow for the VERITAS Collaboration. VHE Blazar Discoveries with VERITAS. *International Cosmic Ray Conference*, September 2011.

[150] P. J. Young, J. A. Westphal, J. Kristian, C. P. Wilson, and F. P. Landauer. Evidence for a supermassive object in the nucleus of the galaxy M87 from SIT and CCD area photometry. *The Astrophysical Journal*, 221:721–730, May 1978.

Appendix A

Spectra of observational data bins

In this appendix the spectrum from Forward Folding on the energy range from 251 GeV to 15.8 TeV is shown together with the Correction factor method data points. If the Forward Folding yields a significance $< 3\sigma$ for a power-law with an exponential cut-off, the spectrum is displayed as a power-law. If the significance is $> 3\sigma$ a power-law with an exponential cut-off is shown.
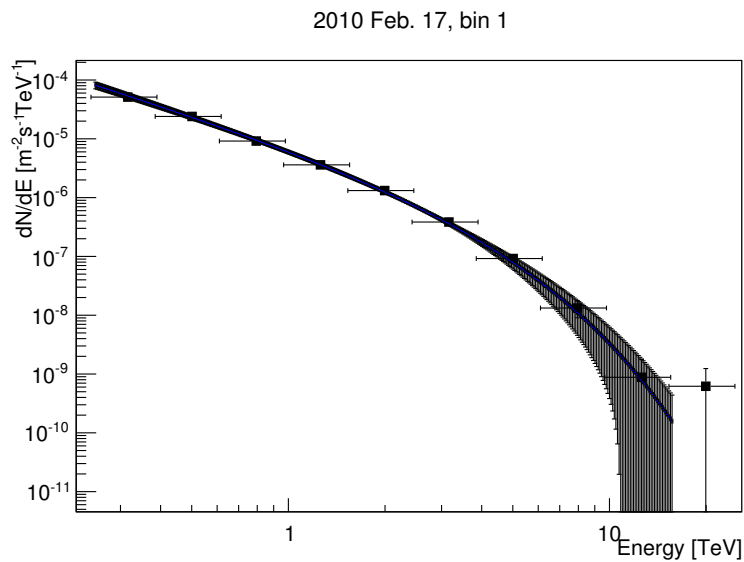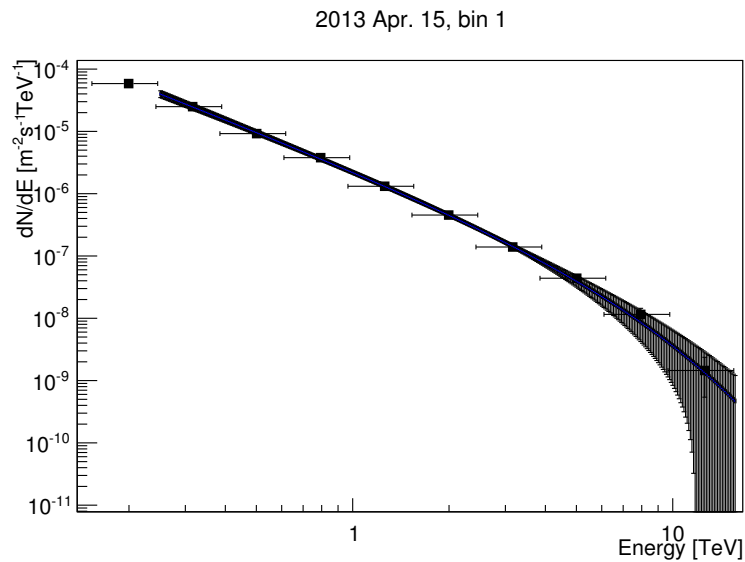

Figure A.1: 2010 Feb. 17, bin 1, power-law with exponential cut-off spectrum. Forward folding from 251 GeV to 15.8 TeV.
Norm $\phi_0 = (8.95 \pm 0.59) \times 10^{-6} \mathrm{m}^{-2}\mathrm{s}^{-1}\mathrm{TeV}^{-1}$, Index $\Gamma = 1.67 \pm 0.06$,
Cut-off energy $E_C = 2.47 \pm 0.29$ TeV, detection with 8.0σ
$\chi^2 = 33.5$ for 33 degrees of freedom.
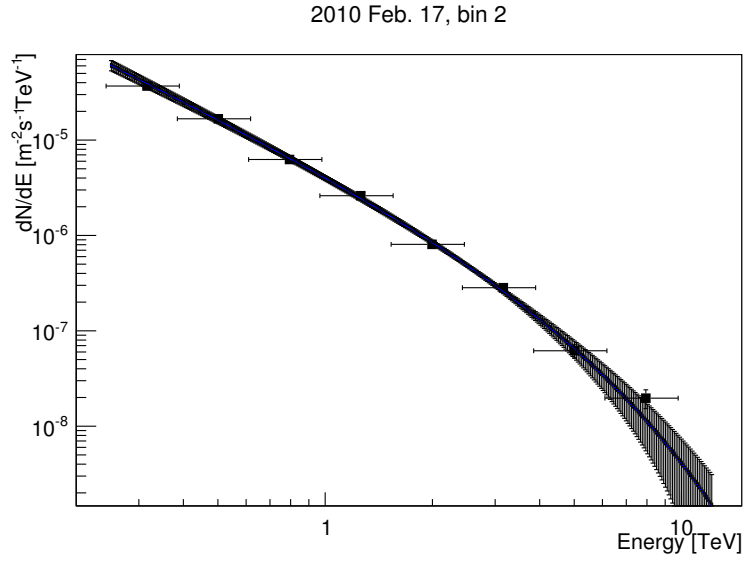
2010 Feb. 17, bin 2
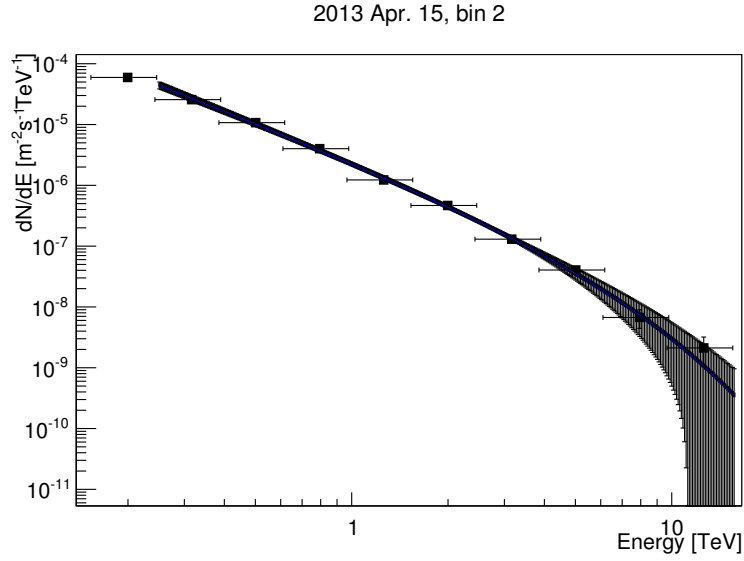

Figure A.2: 2010 Feb. 17, bin 2, power-law with exponential cut-off spectrum. Forward folding from 251 GeV to 15.8 TeV.

Norm $\phi_0 = (5.42 \pm 0.34) \times 10^{-6} \mathrm{m}^{-2}\mathrm{s}^{-1}\mathrm{TeV}^{-1}$, Index $\Gamma = 1.80 \pm 0.06$,

Cut-off energy $E_C = 3.30 \pm 0.45$ TeV, detection with 6.4σ

$\chi^2 = 36.3$ for 33 degrees of freedom.
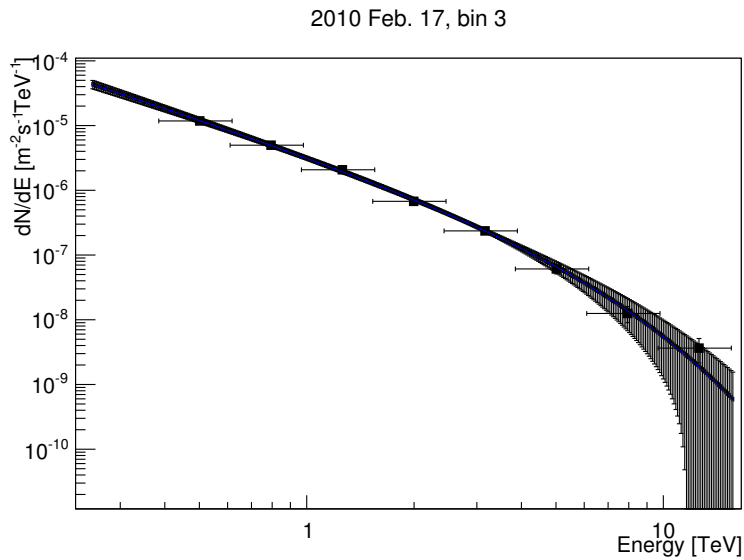
2010 Feb. 17, bin 3

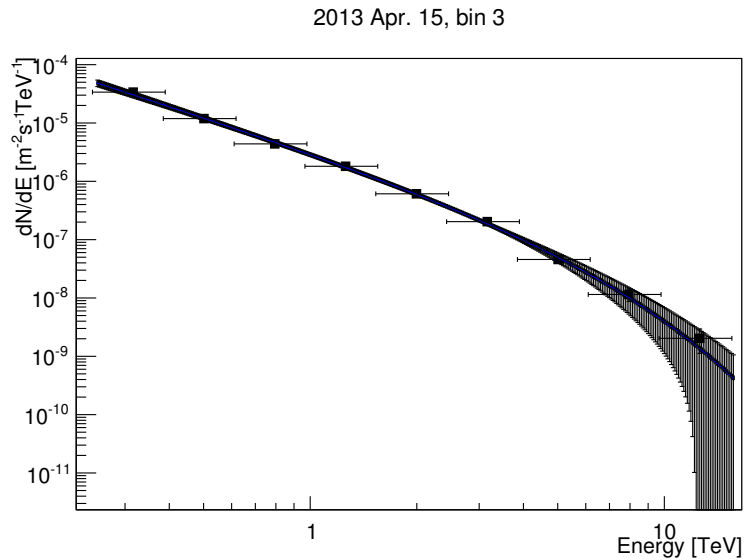Figure A.3: 2010 Feb. 17, bin 3, power-law with exponential cut-off spectrum. Forward folding from 251 GeV to 15.8 TeV.

Norm $\phi_0 = (4.05 \pm 0.28) \times 10^{-6} \mathrm{m}^{-2}\mathrm{s}^{-1}\mathrm{TeV}^{-1}$, Index $\Gamma = 1.76 \pm 0.08$,

Cut-off energy $E_C = 3.94 \pm 0.67$ TeV, significance 5.0σ
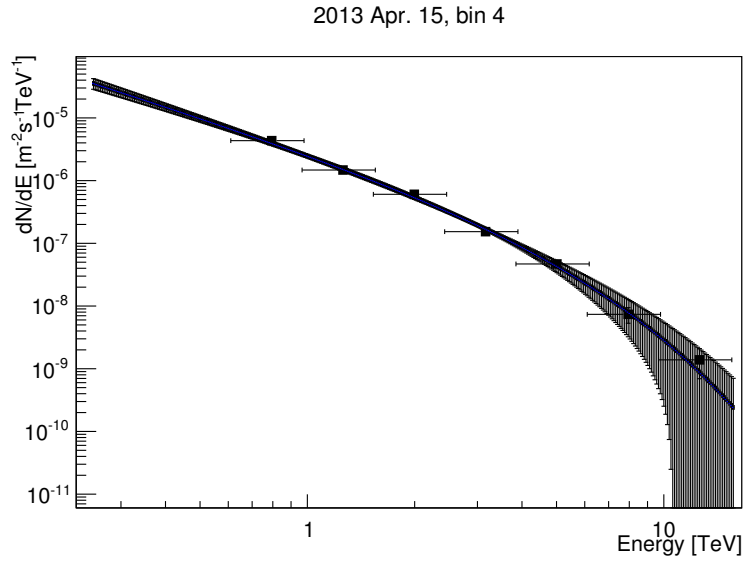
$\chi^2 = 44.2$ for 33 degrees of freedom.
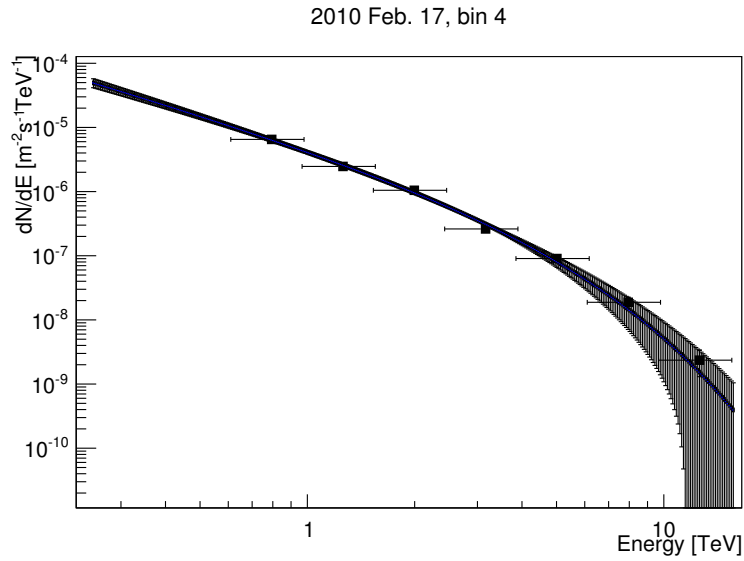
Figure A.4: 2010 Feb. 17, bin 4, power-law with exponential cut-off spectrum.
Forward folding from 251 GeV to 15.8 TeV.
Norm $\phi_0 = (5.68 \pm 0.36) \times 10^{-6} \mathrm{m}^{-2}\mathrm{s}^{-1}\mathrm{TeV}^{-1}$, Index $\Gamma = 1.63 \pm 0.09$,
Cut-off energy $E_C = 3.07 \pm 0.42$ TeV, detection with 6.3σ
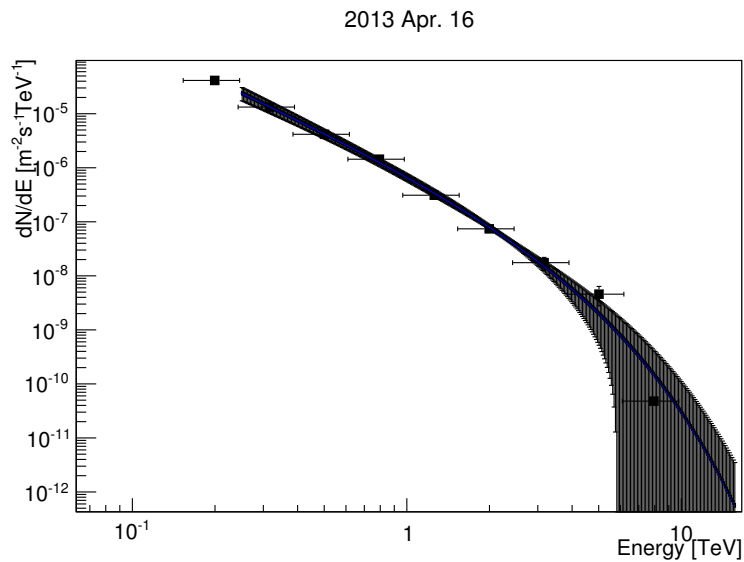$\chi^2 = 42.2$ for 33 degrees of freedom.
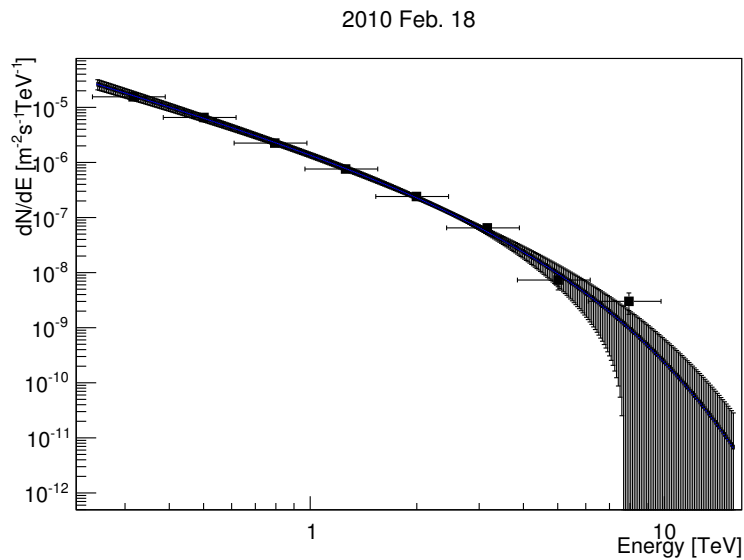
Figure A.5: 2010 Feb. 18, power-law with exponential cut-off spectrum.
Forward folding from 251 GeV to 15.8 TeV.
Norm $\phi_0 = (2.21 \pm 0.24) \times 10^{-6} \mathrm{m}^{-2}\mathrm{s}^{-1}\mathrm{TeV}^{-1}$, Index $\Gamma = 1.88 \pm 0.10$,
Cut-off energy $E_C = 2.08 \pm 0.36$ TeV, significance 5.5σ
$\chi^2 = 22.9$ for 33 degrees of freedom.
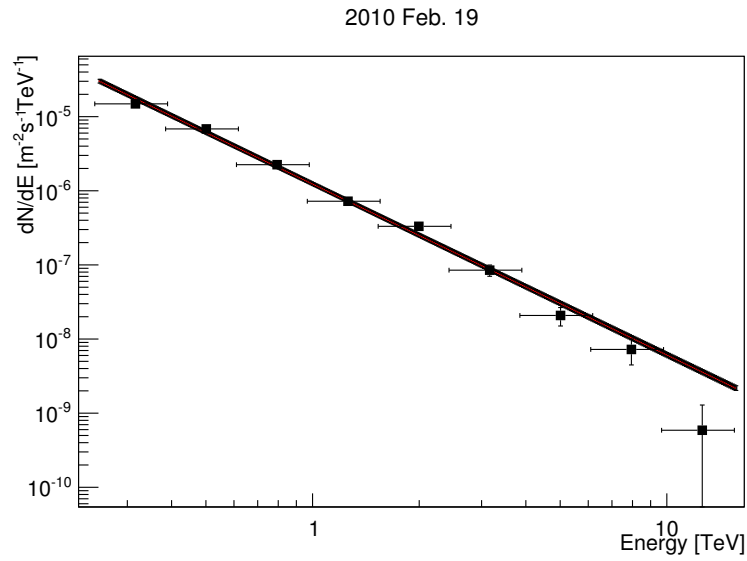
2010 Feb. 19

Figure A.6: 2010 Feb. 19, power-law spectrum.

Forward folding from 251 GeV to 15.8 TeV.

Norm $\phi_0 = (1.25 \pm 0.05) \times 10^{-6} \mathrm{m}^{-2}\mathrm{s}^{-1}\mathrm{TeV}^{-1}$, Index $\Gamma = 2.31 \pm 0.05$,

Cut-off significance 2.7σ, $\chi^2 = 63.8$ for 34 degrees of freedom.
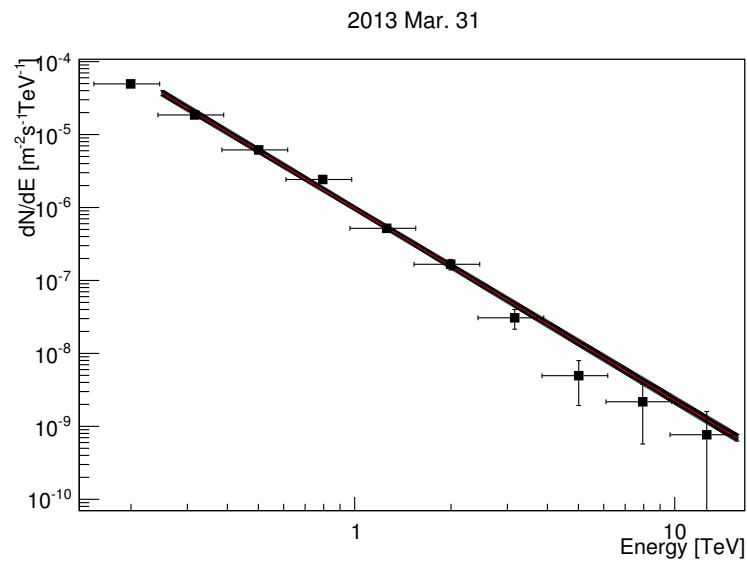
2013 Mar. 31

Figure A.7: 2013 March 31, power-law spectrum.

Forward folding from 251 GeV to 15.8 TeV.

Norm $\phi_0 = (0.98 \pm 0.05) \times 10^{-6} \mathrm{m}^{-2}\mathrm{s}^{-1}\mathrm{TeV}^{-1}$, Index $\Gamma = 2.63 \pm 0.06$

$\chi^2 = 62.8$ for 34 degrees of freedom, cut-off significance 2.5σ.
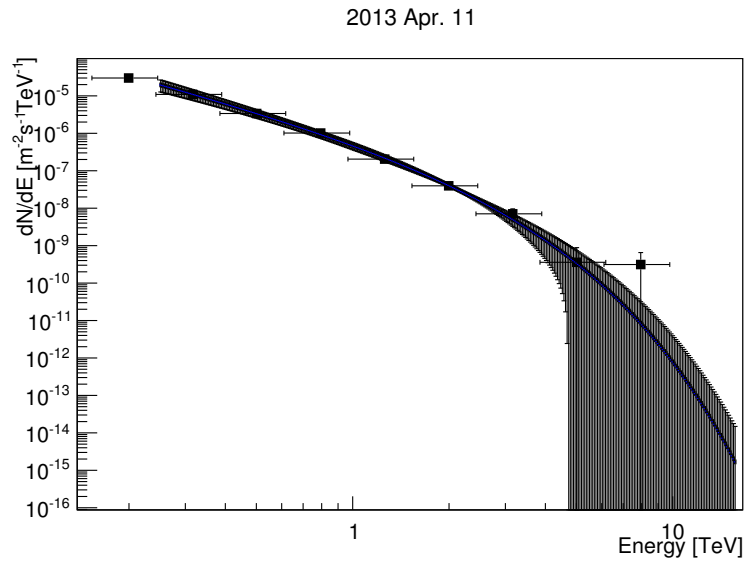
Figure A.8: 2013 April 11, power-law with exponential cut-off spectrum. Forward folding from 251 GeV to 15.8 TeV.

Norm $\phi_0 = (1.16 \pm 0.26) \times 10^{-6} \mathrm{m}^{-2}\mathrm{s}^{-1}\mathrm{TeV}^{-1}$, Index $\Gamma = 2.22 \pm 0.15$,

Cut-off energy $E_C = 1.10 \pm 0.24$ TeV, significance 4.4σ
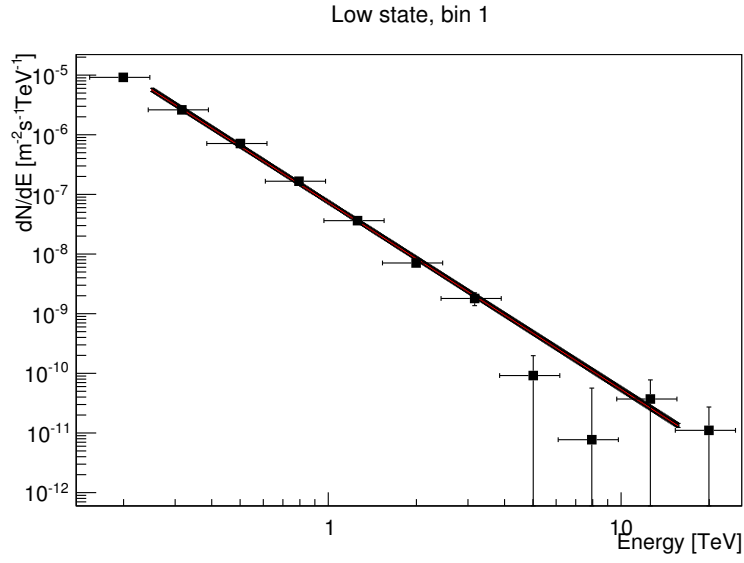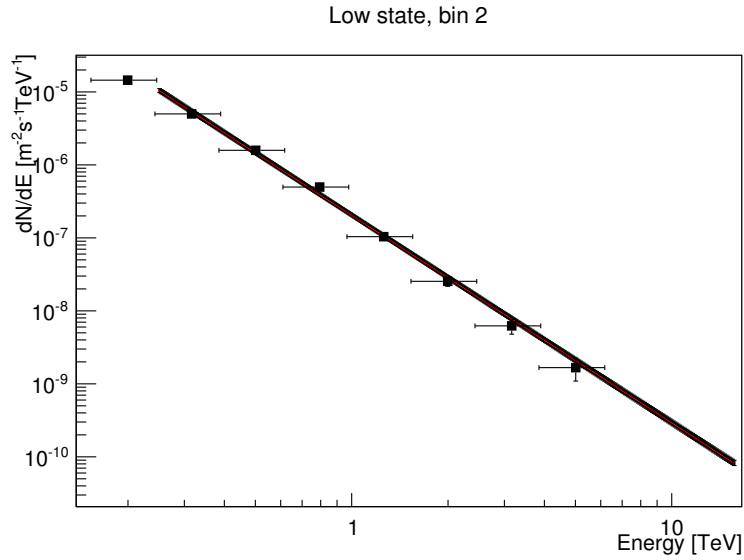
$\chi^2 = 23.0$ for 33 degrees of freedom.
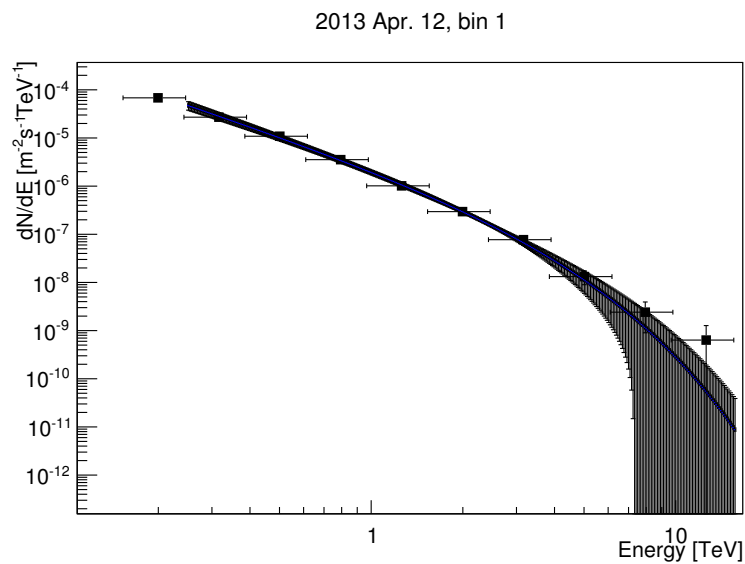
Figure A.9: 2013 April 12, bin 1, power-law with exponential cut-off spectrum. Forward folding from 251 GeV to 15.8 TeV.

Norm $\phi_0 = (3.06 \pm 0.35) \times 10^{-6} \mathrm{m}^{-2}\mathrm{s}^{-1}\mathrm{TeV}^{-1}$, Index $\Gamma = 2.06 \pm 0.09$,

Cut-off energy $E_C = 2.21 \pm 0.43$ TeV, significance 4.8σ

$\chi^2 = 36.8$ for 33 degrees of freedom.
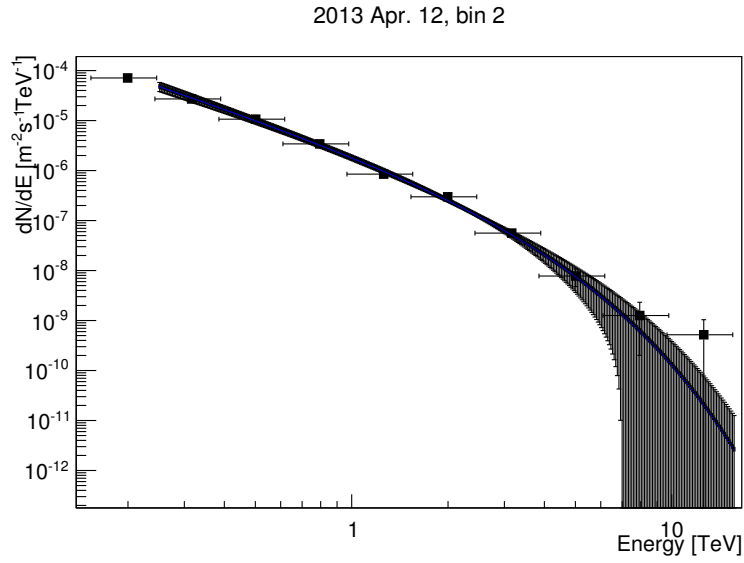
2013 Apr. 12, bin 2

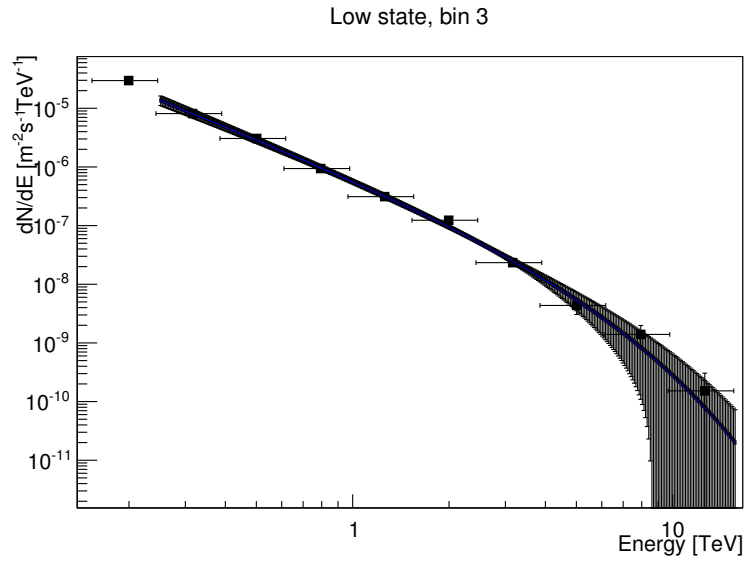Figure A.10: 2013 April 12, bin 2, power-law with exponential cut-off spectrum.
Forward folding from 251 GeV to 15.8 TeV.
Norm $\phi_0 = (3.06 \pm 0.36) \times 10^{-6} \mathrm{m}^{-2}\mathrm{s}^{-1}\mathrm{TeV}^{-1}$, Index $\Gamma = 2.09 \pm 0.09$,
Cut-off energy $E_C = 1.91 \pm 0.35$ TeV, significance 5.2σ
$\chi^2 = 38.2$ for 33 degrees of freedom.
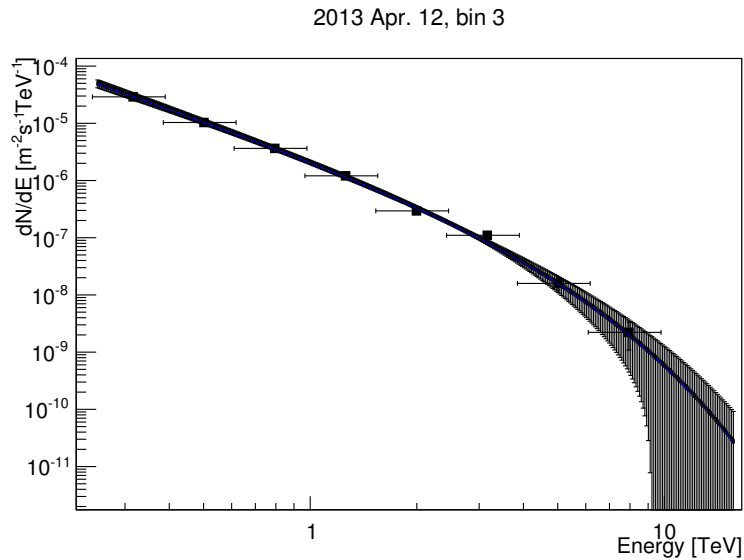
2013 Apr. 12, bin 3

Figure A.11: 2013 April 12, bin 3, power-law with exponential cut-off spectrum.
Forward folding from 251 GeV to 15.8 TeV.
Norm $\phi_0 = (3.02 \pm 0.25) \times 10^{-6} \mathrm{m}^{-2}\mathrm{s}^{-1}\mathrm{TeV}^{-1}$, Index $\Gamma = 2.09 \pm 0.07$,
Cut-off energy $E_C = 2.68 \pm 0.43$ TeV, significance 5.5σ
$\chi^2 = 33.4$ for 33 degrees of freedom.
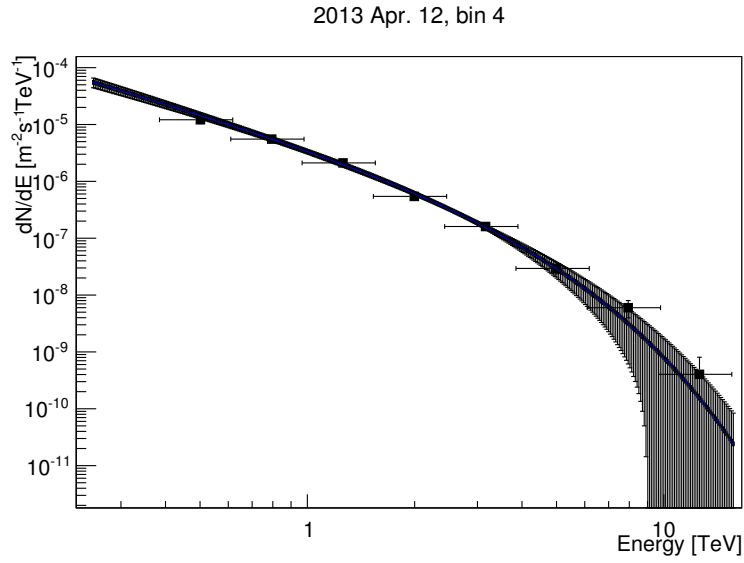
2013 Apr. 12, bin 4

Figure A.12: 2013 April 12, bin 4, power-law with exponential cut-off spectrum.
Forward folding from 251 GeV to 15.8 TeV.
Norm $\phi_0 = (5.38 \pm 0.47) \times 10^{-6} \mathrm{m}^{-2} \mathrm{s}^{-1} \mathrm{TeV}^{-1}$, Index $\Gamma = 1.77 \pm 0.10$,
Cut-off energy $E_C = 2.10 \pm 0.29$ TeV, significance 6.6σ
$\chi^2 = 31.9$ for 33 degrees of freedom.

2013 Apr. 13, bin 1
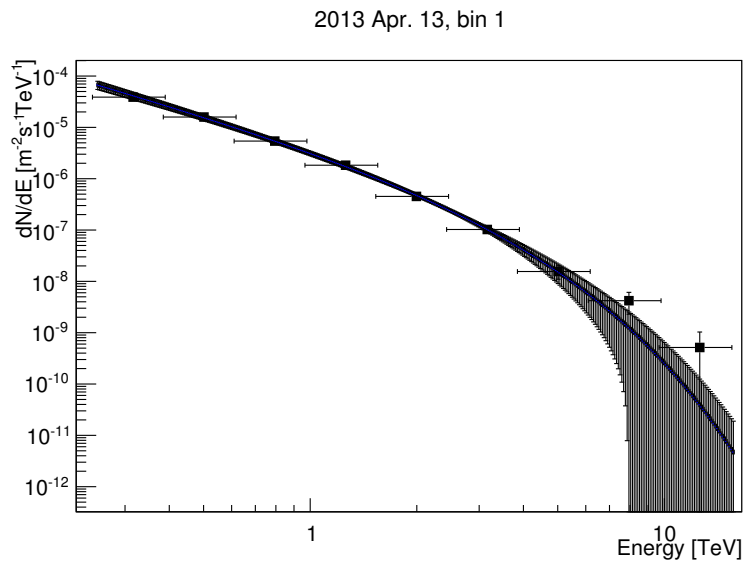
Figure A.13: 2103 April 13, bin 1, power-law with exponential cut-off spectrum.
Forward folding from 251 GeV to 15.8 TeV.
Norm $\phi_0 = (5.44 \pm 0.54) \times 10^{-6} \mathrm{m}^{-2} \mathrm{s}^{-1} \mathrm{TeV}^{-1}$, Index $\Gamma = 1.92 \pm 0.08$,
Cut-off energy $E_C = 1.81 \pm 0.25$ TeV, significance 6.8σ
$\chi^2 = 44.1$ for 33 degrees of freedom.
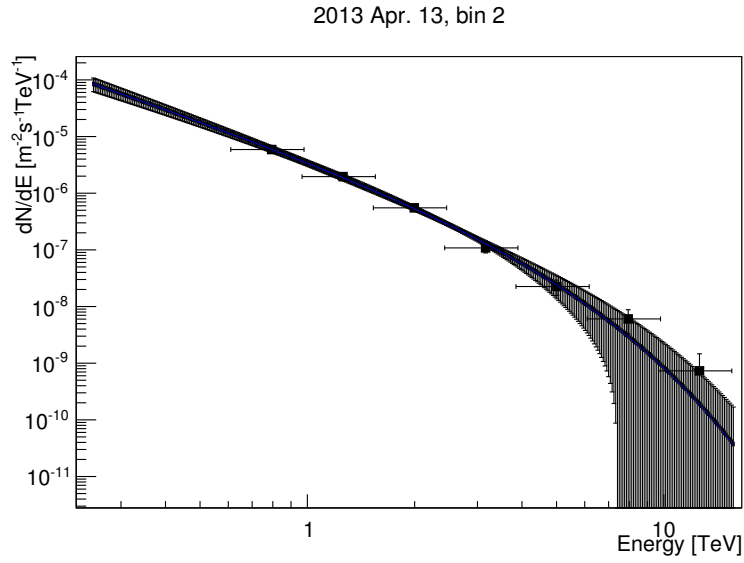
2013 Apr. 13, bin 2

Figure A.14: 2013 April 13, bin 2, power-law with exponential cut-off spectrum.
Forward folding from 251 GeV to 15.8 TeV.
Norm $\phi_0 = (5.00 \pm 0.61) \times 10^{-6}\text{m}^{-2}\text{s}^{-1}\text{TeV}^{-1}$, Index $\Gamma = 2.12 \pm 0.14$,
Cut-off energy $E_C = 2.62 \pm 0.63$ TeV, significance 3.7σ
$\chi^2 = 43.1$ for 33 degrees of freedom.
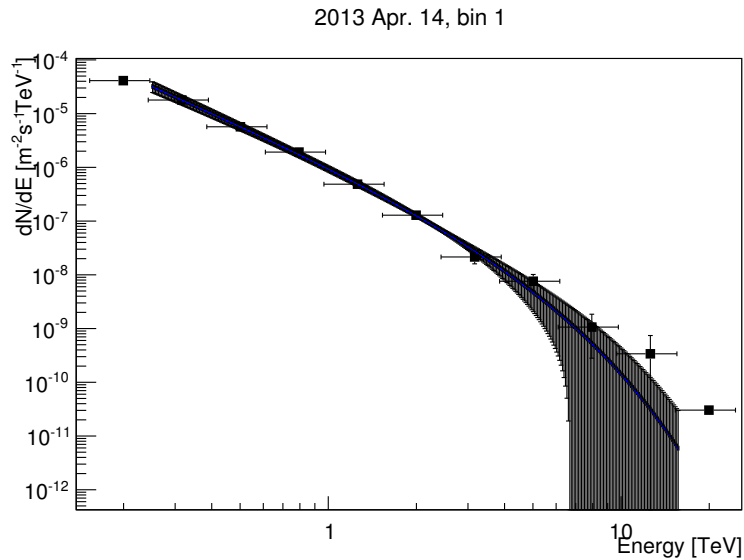
2013 Apr. 14, bin 1

Figure A.15: 2013 April 14, bin 1, power-law with exponential cut-off spectrum.
Forward folding from 251 GeV to 15.8 TeV.
Norm $\phi_0 = (1.38 \pm 0.18) \times 10^{-6}\text{m}^{-2}\text{s}^{-1}\text{TeV}^{-1}$, Index $\Gamma = 2.35 \pm 0.10$.
Cut-off energy $E_C = 2.66 \pm 0.72$ TeV, significance 3.3σ
$\chi^2 = 40.9$ for 33 degrees of freedom.
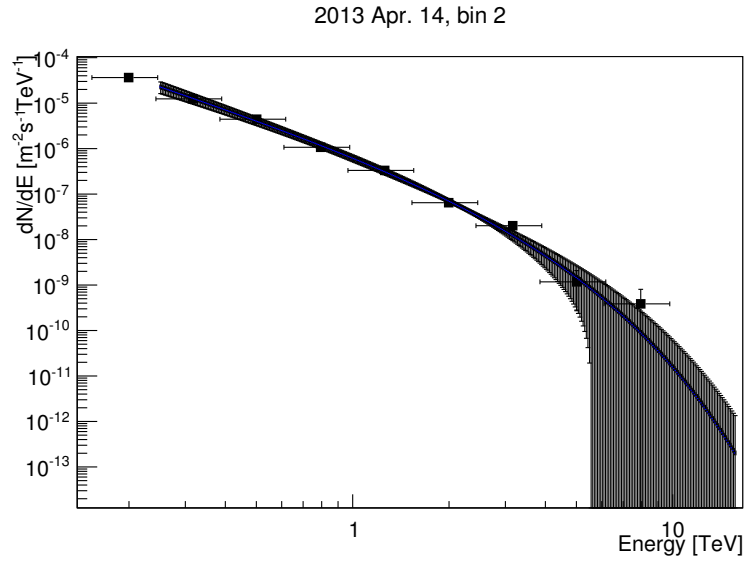
Figure A.16: 2013 April 14, bin 2, power-law with exponential cut-off spectrum.
Forward folding from 251 GeV to 15.8 TeV.
Norm $\phi_0 = (1.12 \pm 0.19) \times 10^{-6} \mathrm{m}^{-2} \mathrm{s}^{-1} \mathrm{TeV}^{-1}$, Index $\Gamma = 2.29 \pm 0.13$,
Cut-off energy $E_C = 1.70 \pm 0.41$ TeV, significance 3.8σ
$\chi^2 = 30.2$ for 33 degrees of freedom

Figure A.17: 2013 April 15, bin 1, power-law with exponential cut-off spectrum.
Forward folding from 251 GeV to 15.8 TeV.
Norm $\phi_0 = (2.70 \pm 0.17) \times 10^{-6} \mathrm{m}^{-2} \mathrm{s}^{-1} \mathrm{TeV}^{-1}$, Index $\Gamma = 1.99 \pm 0.06$,
Cut-off energy $E_C = 4.91 \pm 0.99$ TeV, significance 4.1σ
$\chi^2 = 30.8$ for 33 degrees of freedom.

2013 Apr. 15, bin 2

Figure A.18: 2013 April 15, bin 2, power-law with exponential cut-off spectrum.
Forward folding from 251 GeV to 15.8 TeV.
Norm $\phi_0 = (2.78 \pm 0.19) \times 10^{-6} \mathrm{m}^{-2}\mathrm{s}^{-1}\mathrm{TeV}^{-1}$, Index $\Gamma = 2.04 \pm 0.06$,
Cut-off energy $E_C = 4.69 \pm 0.97$ TeV, significance 4.1σ
$\chi^2 = 37.6$ for 33 degrees of freedom.

2013 Apr. 15, bin 3

Figure A.19: 2013 April 15, bin 3, power-law with exponential cut-off spectrum.
Forward folding from 251 GeV to 15.8 TeV.
Norm $\phi_0 = (3.65 \pm 0.23) \times 10^{-6} \mathrm{m}^{-2}\mathrm{s}^{-1}\mathrm{TeV}^{-1}$, Index $\Gamma = 1.91 \pm 0.07$,
Cut-off energy $E_C = 4.14 \pm 0.67$ TeV, significance 5.2σ
$\chi^2 = 26.7$ for 33 degrees of freedom.

Figure A.20: 2013 April 15, bin 4, power-law with exponential cut-off spectrum.
Forward folding from 251 GeV to 15.8 TeV.
Norm $\phi_0 = (3.32 \pm 0.24) \times 10^{-6} \mathrm{m}^{-2}\mathrm{s}^{-1}\mathrm{TeV}^{-1}$, Index $\Gamma = 1.77 \pm 0.12$,
Cut-off energy $E_C = 3.36 \pm 0.59$ TeV, significance 4.7σ
$\chi^2 = 154.2$ for 33 degrees of freedom.

Figure A.21: 2013 April 16, power-law with exponential cut-off spectrum.
Forward folding from 251 GeV to 15.8 TeV.
Norm $\phi_0 = (1.13 \pm 0.18) \times 10^{-6} \mathrm{m}^{-2}\mathrm{s}^{-1}\mathrm{TeV}^{-1}$, Index $\Gamma = 2.31 \pm 0.12$,
Cut-off energy $E_C = 1.92 \pm 0.49$ TeV, significance 3.6σ
$\chi^2 = 52.6$ for 33 degrees of freedom.

Low state, bin 1

Figure A.22: Low state bin 1, power-law spectrum.

Forward folding from 251 GeV to 15.8 TeV.

Norm $\phi_0 = (7.4 \pm 0.3) \times 10^{-8} \mathrm{m}^{-2} \mathrm{s}^{-1} \mathrm{TeV}^{-1}$, Index $\Gamma = 3.13 \pm 0.04$,

$\chi^2 = 75.0$ for 34 degrees of freedom.

Low state, bin 2

Figure A.23: Low state bin 2, power-law spectrum.

Forward folding from 251 GeV to 15.8 TeV.

Norm $\phi_0 = (2.06 \pm 0.08) \times 10^{-7} \mathrm{m}^{-2} \mathrm{s}^{-1} \mathrm{TeV}^{-1}$, Index $\Gamma = 2.84 \pm 0.04$,

$\chi^2 = 63.2$ for 34 degrees of freedom.

Figure A.24: Low state bin 3, power-law with exponential cut-off spectrum.
Forward folding from 251 GeV to 15.8 TeV.
Norm $\phi_0 = (0.76 \pm 0.08) \times 10^{-6} \mathrm{m}^{-2}\mathrm{s}^{-1}\mathrm{TeV}^{-1}$, Index $\Gamma = 2.15 \pm 0.09$,
Cut-off energy $E_C = 3.39 \pm 0.78$ TeV, significance 3.8σ
$\chi^2 = 36.7$ for 33 degrees of freedom.

List of Figures

135

List of Tables

Acknowledgements

My many thanks, in the first instance, go to the supervisor of this thesis Dr. Gernot Maier. I am very grateful for the opportunity to work in his group and all the support over the last years. His commitment to the ideals of science and his profound knowledge about γ-ray astronomy have been a guiding thread for my daily work. Likewise I thank the members of my PhD committee and in particular Prof. Dr. Andy Smith and Prof. Dr. Thomas Lohse for refereeing this dissertation.

But of course, the completion of this thesis would not have been possible without the help of all my other colleauges from DESY. Dr. Lucie Gerard with her critical intellect gave a structure to my work. She constantly motivated me to bring the best out of this project. Together with Dr. Anna O'Faolain de Broithe she helped me to shape a real thesis. I would also like to thank Dr. Serguei Vorobiov for valuable discussion during the lunch breaks.

It was always fun to be part of VERITAS and DESY.

I do not want to forget Dr. Karl Jansen the supervisor of my dipoma thesis, who brought me to DESY for the very first time as a summer student.

Last but not least it was my family and friends with their constant motivation and esteem who made this work possible. I would like to mention my brother and my mother and thank them for all their love.

Selbstständigkeitserklärung

Hiermit erkläre ich, dass ich die vorliegende Arbeit selbstständig und nur unter Verwendung der angegebenen Literatur und Hilfsmittel angefertigt habe. Ich habe mich nicht anderweitig um einen Doktorgrad beworben und besitze keinen Doktorgrad. Die Promotionsordnung der Mathematisch-Naturwissenschaftlichen Fakultät der Humboldt-Universität zu Berlin ist mir bekannt.

Berlin, den 03.07.2014   Roman Welsing